UNIVERSITY OF CALIFORNIA,
IRVINE

Microfluidic Devices for Digestion, Dissociation, and Filtration of Tissues into Single Cell Suspensions

DISSERTATION

submitted in partial satisfaction of the requirements
for the degree of

DOCTOR OF PHILOSOPHY

in Biomedical Engineering

by

Xiaolong Qiu

Dissertation Committee:
Assistant Professor Jered B. Haun, Chair
Associate Professor Elliot E. Hui
Professor Edward L. Nelson

2017

DEDICATION

To my parents, for their unconditional love and support.

TABLE OF CONTENTS

LIST OF FIGURES

LIST OF TABLES

ACKNOWLEDGMENTS

I would like to express the deepest appreciation to my advisor and committee chair, Dr. Jered B. Haun for all his guidance and mentorship over the past five years through every step of my research. Your endless help and support throughout my graduate work has made me a better researcher. This work would not have been possible without his constant inspiration, enthusiasm, encouragement, patience, and passion.

I would like to thank my committee members, Drs. Elliot E. Hui and Edward L. Nelson for providing me with their insight and expertise on various projects and collaborations. I am grateful to all their advice and guidance that I received through our fruitful discussions.

I would also like to thank my other qualifying exam committee members, Drs. Abraham P. Lee, William C. Tang, and Mark Bachman for their critiques during my advancement exam.

My sincerest gratitude to all members of the Haun lab. I would like to thank my mentor Janice De Jesus for introducing me to her world of microfluidic tissue processing, my labmates Marissa Pennell, Pedram P. Pourfard, Jeremy A. Lombardo, Hinesh V. Patel, Maha Rahim, and Vanessa Herrera, for their help at various stages of my work, and my undergraduate students Marco Troiani, Katrina Henrikson, Stephanie Pearlman, Danny Duong, Griffith L. Wagner, Anita Ng, and Miami Shafeeq for their passion and willingness to learn from me.

Special thanks to Dr. Trisha M. Westerhof from the Nelson lab for her contributions to flow cytometry, biopsy harvesting, and animal work involved in my projects. Special thanks to Drs. Pulak Nath and Jen-Huang Huang from Los Alamos National Laboratories, Amrith Karunaratne and Erik Werner from the Hui lab for their help with device design and fabrications. I truly appreciated all your help.

I would like to acknowledge the Royal Society of Chemistry for providing me with permissions to include copyrighted materials as part of my dissertation.

Lastly, I would like to extend my gratitude to the Center for Advanced Design & Manufacturing of Integrated Microfluidics (CADMIM), National Cancer Institute, and UC Cancer Research Coordinating Committee for their funding support.

CURRICULUM VITAE

Xiaolong Qiu

EDUCATION

Ph.D. in Biomedical Engineering **2017**
University of California, Irvine

M.S. in Biomedical Engineering **2015**
University of California, Irvine

B.S. in Chemical Engineering **2012**
University of California, San Diego

JOURNAL PUBLICATIONS

X. Qiu, J. Huang, T. M. Westerhof, J. A. Lombardo, K. M. Henrikson, M. Pennell, P. P. Pourfard, E. L. Nelson, P. Nath, and J. B. Haun. Microfluidic channel design optimization to improve hydrodynamic dissociation of cell aggregates and tissue. *Lab Chip*. 2017. Submitted.

X. Qiu, T. M. Westerhof, A. Karunaratne, E. Werner, P. P. Pourfard, E. L. Nelson, E. E. Hui, and J. B. Haun. Microfluidic device for rapid digestion of tissues into cellular suspensions. *Lab Chip*. 2017. Accepted.

D. A. Banyard, C. N. Sarantopoulos, A. A. Borovikova, **X. Qiu**, G. A. Wirth, K. Z. Paydar, J. B. Haun, G. R. Evans, and A. D. Widgerow. Phenotypic analysis of stromal vascular fraction after mechanical shear reveals stress-induced progenitor populations. *Plast Reconstr Surg.* 2016, 138(2), 237e-247e.

X. Qiu, J. De Jesus, M. Pennell, M. Troiani, and J. B. Haun. Microfluidic device for mechanical dissociation of cancer cell aggregates into single cells. *Lab Chip.* 2015, 15(1), 339-350.

PODIUM TALKS

X. Qiu, T. Westerhof, J. De Jesus, Pennell, M. Troiani, E. L. Nelson, and J. B. Haun. Microfluidic device for mechanical dissociation of tumor tissues into single cells. Presented at Associated Graduate Student Symposium. Irvine, CA. March 2015.

X. Qiu, H. V. Patel, M. Pennell, E. E. Hui, and J. B. Haun. Tissue processing chip for single-cell molecular diagnostics. Presented at Center for Advanced Design and Manufacturing of Integrated Microfluidics industry advisory board meeting. Cincinnati, OH. September, 2015.

X. Qiu, T. Westerhof, M. Pennell, E. L. Nelson, and J. B. Haun. Microfluidic device for mechanical dissociation of tumor tissue into single cells. Presented at Biomedical Engineering Society annual meeting. Tampa, FL. October 2015.

X. Qiu, E. Werner, A. Karunaratne, E. E. Hui, and J. B. Haun. Integrated Tumor Biopsy Platform. Presented at Center for Advanced Design and Manufacturing of Integrated Microfluidics industry advisory board meeting. Cincinnati, OH. September, 2016.

X. Qiu, T. Westerhof, A. Karunaratne, E. Werner, P. Pourfard, E. L. Nelson, E. E. Hui, and J. B. Haun. Microfluidic device for rapid digestion of tissues into cellular suspensions. Presented at UC Systemwide Bioengineering Symposium. Los Angeles, CA. June 2017.

POSTER PRESENTATIONS

X. Qiu, M. Pennell, M. Troiani, E. E. Hui, and J. B. Haun. A microfluidic device for dissociating tumor tissue into single cells. Presented at Center for Complex Biological Systems annual retreat. Pasadena, CA. March 2014.

X. Qiu, M. Pennell, M. Troiani, E. E. Hui, and J. B. Haun. A microfluidic device for dissociating tumor tissue into single cells. Presented at Center for Advanced Design and Manufacturing of Integrated Microfluidics industry advisory board meeting. Irvine, CA. April 2014.

X. Qiu, M. Pennell, M. Troiani, E. E. Hui, and J. B. Haun. A microfluidic device for dissociating tumor tissue into single cells. Presented at UC Systemwide Bioengineering Symposium. Irvine, CA. June 2014.

X. Qiu, M. Pennell, M. Troiani, E. E. Hui, and J. B. Haun. A microfluidic device for dissociating tumor tissue into single cells. Presented at Chao Family Comprehensive Cancer Center annual scientific retreat. Palm Springs, CA. September 2014.

X. Qiu, M. Pennell, M. Troiani, E. E. Hui, and J. B. Haun. A microfluidic device for dissociating tumor tissue into single cells. Presented at Biomedical Engineering Society annual meeting. San Antonio, TX. October 2014.

X. Qiu, T. Westerhof, M. Pennell, K. Henrikson, E. E. Hui, E. L. Nelson, and J. B. Haun. Microfluidic device for mechanical dissociation of tumor into single cells. Presented at Center for Advanced Design and Manufacturing of Integrated Microfluidics industry advisory board meeting. Irvine, CA. February 2015.

X. Qiu, T. Westerhof, M. Pennell, K. Henrikson, E. E. Hui, E. L. Nelson, and J. B. Haun. Microfluidic device for mechanical dissociation of tumor into single cells. Presented at Center for Advanced Design and Manufacturing of Integrated Microfluidics industry advisory board meeting. Irvine, CA. March 2016.

X. Qiu, A. Karunaratne, E. Werner, P. Pourfard, T. Westerhof, E. E. Hui, and J. B. Haun. Incubation chamber device for rapid dissociation of core biopsies. Presented at Center for Advanced Design and Manufacturing of Integrated Microfluidics industry advisory board meeting. Cincinnati, OH. September, 2016.

X. Qiu, M. Pennell, D. Duong, A. Ng, and J. B. Haun. Integrated filter device for dissociation and enrichment of single cells from tissue. Presented at Center for Advanced Design and Manufacturing of Integrated Microfluidics industry advisory board meeting. Cincinnati, OH. September, 2016.

X. Qiu, T. Westerhof, M. Pennell, K. Henrikson, E. L. Nelson, and J. B. Haun. Microfluidic devices for mechanical dissociation and filtration of tumor tissues into single cells. Presented at Biomedical Engineering Society annual meeting. Minneapolis, MN. October 2016.

X. Qiu, T. Westerhof, M. Pennell, K. Henrikson, E. L. Nelson, and J. B. Haun. Microfluidic devices for mechanical dissociation and filtration of tumor tissues into single cells. Presented at Chao Family Comprehensive Cancer Center annual scientific retreat. Long Beach, CA. November 2016.

X. Qiu, T. Westerhof, E. Werner, A. Karunaratne, P. Pourfard, E. L. Nelson, E. E. Hui, and J. B. Haun. Microfluidic device for rapid digestion of tissues into cellular suspensions. Presented at Center for Advanced Design and Manufacturing of Integrated Microfluidics industry advisory board meeting. Irvine, CA. March 2017.

X. Qiu, J. Huang, K. Henrikson, M. Pennell, P. Pourfard, P. Nath, and J. B. Haun. Microfluidic device for mechanical dissociation of tissues into single cells. Presented at Center for Advanced Design and Manufacturing of Integrated Microfluidics industry advisory board meeting. Irvine, CA. March 2017.

X. Qiu, M. Pennell, J. Lombardo, G. Wagner, E. E. Hui, and J. B. Haun. Integrated filter device for dissociation and enrichment of single cells from cell aggregates. Presented at Center for Advanced Design and Manufacturing of Integrated Microfluidics industry advisory board meeting. Irvine, CA. March 2017.

ABSTRACT OF THE DISSERTATION

Microfluidic Devices for Digestion, Dissociation, and Filtration of Tissues into Single Cell Suspensions

By

Xiaolong Qiu

Doctor of Philosophy in Biomedical Engineering

University of California, Irvine, 2017

Professor Jered B. Haun, Chair

The ability to harvest primary cells from tissues is crucial in the fields of tissue engineering and regenerative medicine. Furthermore, achieving cellular suspensions from tissues in a timely and efficient manner is currently a bottleneck to the use of single cell-based technologies to analyze diseases such as cancer. Various enzymatic and mechanical approaches have attempted to solve this problem, but with limited success. Thus, there is a critical need to develop new techniques to improve the speed and efficiency of tissue dissociation at the point-of-care. One of the biggest advantages of microfluidics lies in its ability to precisely control flow profiles and thus the shear forces. This advantage provides an ideal platform for tissue dissociation at the single cell resolution. The overall goal of this dissertation is to develop a suite of microfluidic devices to achieve point-of-care tissue dissociation. First, to digest clinically resected tissue cores, we design a microfluidic device that utilizes precision fluid flows to rapidly digest tissues into cellular suspensions. Our microfluidic channels are designed to hydrodynamically mince tissues at discrete locations, while maximizing enzyme-tissue contact, thus accelerating digestion. We show our device

is superior at recovering cells compared to conventional methods using animal organ tissues. Second, we employ a series of branching channel network in our dissociation device to gradually reduce device cross-section through a series of bifurcating stages. The constriction and expansion regions induce flow disturbances that help mix the sample and generate fluidic jets at different length scales to produce shear forces necessary to dissociate cell aggregates. Device performance has been characterized with tumor spheroids and human biopsies from cancer patients. Lastly, we demonstrate a microfluidic filter device with integrated microscale nylon mesh membranes to retain and recycle aggregates for further dissociation while selectively allowing single cells to elute from the device. Promising results have been achieved from device testing with cancer cell lines as well as animal organ tissues. At this point, each device has been developed with its specific goal in mind. In the future, all devices will be integrated to achieve a lab-on-a-chip tissue to single cell dissociation platform.

CHAPTER 1 INTRODUCTION

1.1 Current Landscape of Cancer Diagnostics

With the only exception of leukemia, nearly every type of cancer forms solid tumors, abnormal tissue masses that are now viewed as an ecosystem of diverse cell types. This heterogeneity has been identified as a key factor underlying tumor progression, metastasis, and the development of drug resistance [1], [2]. This has led to an increase in studies that are focused on defined cellular subsets within tumors to address biological and therapeutic questions. The diverse cell types comprising tumors can include neoplastic subpopulations with distinct genotypes and phenotypes arising from clonal evolution and hierarchical differentiation from cancer stem cells (CSCs) [1], [3]. Host cells of diverse origins, such as non-tumor epithelium, stoma, and immune subtypes, also promote tumor growth in various capacities [1], [4]. Thus, tumor heterogeneity analysis and identification of key cell types have become major focus areas in tumor biology and clinical diagnostics [5].

Ultimately, the goal of clinical cancer treatment is to first gather information about the molecular drivers of each tumor and then directly target these pathways with specific pharmaceutical or biological interventions. Indeed, this is the way in current treatment of breast (HER2 amplification), lung (EGFR mutation), and colon (KRAS mutation), and melanoma (BRAF mutation) [6]–[9]. But cellular heterogeneity, specifically the presence of key cell types such as CSCs, has major implications for clinical diagnostics. Identified as the most critical cell type for cancer progression and metastasis, CSCs should serve as the direct target of cancer therapies if effective cures are to be achieved [5]. For instance, CSCs appear to have different therapeutic sensitivities than cancer cells with more differentiated

features. It is unclear whether standard chemotherapeutic, radiotherapeutic, or biological therapeutic agents are effective at treating CSCs [10], [11]. It has further been proposed that elimination of CSCs is essential for achieving more effective therapies. However, CSCs not only vary from patient to patient, but also only represent a small population of tumor cells (0.01 to 0.1%), making them difficult to trace [12]. Endothelial cells are another example of a clinically relevant cell subpopulation, as abnormal and increased vasculature is a hallmark of tumor growth and progression [13]. Insights into tumor angiogenesis and the advent of effective anti-angiogenic therapies has further heightened the importance of understanding the role of endothelial cells and their progenitors in tumors. Recent studies have shown that number of endothelial progenitor cells may be both a predictor and indicator of response to anti-angiogenic therapy [14]. In addition, the presence of infiltrating leukocytes is also of great interest to address biological and clinical questions. However its subtype would need to be identified first.

The search for specific cell types in tumors is often hindered by the fact that tumors are three-dimensional tissues. Current tissue-based methods and "omic" technologies are low throughput, underpowered, and require sample destruction, which ultimately leads to the loss of cellular context. Nevertheless, cell-based analysis platforms such as flow cytometry have the potential to satisfy throughput demands with cellular resolution while allowing the entire population to be analyzed. Other cell-based platforms include mass cytometry [15], microfabricated magnetic and optical detectors [16]–[18], cytology [19], single cell gene sequencing [20], and physical measurements such as density and deformability [21], [22]. In order to provide material for identification and analysis of specific tumor cell subsets such as cancer stem cells, metastatic precursors, or drug

resistant clones for more detailed studies, single cell suspensions would needed to be obtained from tumor tissues [23]–[26].

Single cell suspensions are typically achieved for large tissue specimens such as surgical resections and core biopsies through a combination of mincing with a scalpel and treatment with proteolytic enzymes that digest the underlying extracellular matrix (ECM). While this treatment is mild, leaving cells relatively undisturbed, it does require long incubation times on the order of hours, which could negatively affect cell viability or molecular expression. Enzymatic treatment is usually accompanied by vortexing and repeated pipetting of the sample to augment yield. During these processes, samples are typically subjected to poorly defined shear flow environments that do not allow control over sample exposure, potentially resulting in large variability. Poorly defined hydrodynamics could also cause compromises in cell viability during sample processing. To date, the gentleMACS™ Dissociator is the only commercially available system that has been developed to standardize mechanical dissociation for large tumor tissues [27]. However, its use and performances are not well documented and studied. Thus, there is a critical need to develop new technologies to improve current tissue digestion methods to truly take advantage of cell-based analysis platforms available. Improving mechanical dissociation would enhance cell recovery, shorten enzymatic digestion time, and potentially enable non-enzymatic treatments to better protect cellular integrity and viability.

1.2 Microfluidics and Microfabrication

Microfabrication refers to a set of manufacturing technologies that is capable of creating objects having micrometer scale dimensions. Microfabricated objects or devices

can be seen in a variety of engineering disciplines and applications, ranging from semiconductor chipsets in electrical engineering to biosensing devices in biomedical engineering [28]. Utilizing the technology of microfabrication, fluidic devices with micron scaled channel features are made possible. Behavior of fluids at such miniaturized levels and length scales are different from those observed at larger length scales. The regime of fluid flow is dominated by laminar flow over turbulent flow, which is characterized by high momentum diffusion over low momentum convection. Such behaviors of laminar flow can be well-characterized and devices serve particular purposes can also be designed based on such fluidic properties [29], [30].

Advances in the rapid-developing industry of large-scale biology, biochemistry, and medicine in the past decades have made extreme sensitivity and reproducibility possible in biomedical engineering and its related fields. For instance, advancement in genomic and proteomic technologies would require complex yet high-throughput analysis platforms that are able to process small sample sizes in short time scales. In order to take advantage of these technological advances, small scale systems that are suitable for laboratory operations would need to be developed. Technological advancements in microfabrication has helped translate the landscape of bench scale biological experiments and processes in the fields of biomedical engineering and medicine. In particular, microfluidic analytical devices have been the subject of much research interest over the past few decades in both academia and industry. The motivation to shift from macroscale analytical procedures to micro-analytical devices is driven by efforts to minimize sample consumption, decrease processing time, create possibilities of integration and automation, and provide high throughout potentialities [31].

The idea of microfluidics was largely inspired by the movement of miniaturization in the semiconductor industry. The successful development of Microelectromechanical systems (MEMS) in silicon processing techniques was introduced as a model to help translate bench scale biological processes into Micro Total Analysis Systems (μTAS), or commonly known as Lab-On-A-Chip (LOC) systems. LOC systems is capable of integrating multiple conventional bench operations into a single on-chip process, thus minimizing cost of labor, reagents, and materials. Sample volume reduction has always seen as a desirable feature in microfabricated systems designed for various applications. In the case of *in vitro* diagnostics, reduction in sample volume could potentially reduce volume of blood drawn or sampling pain from diabetic patients undergoing glucose sensing. Reduction of time is another factor that is generally emphasized in miniaturized device development. By reducing amount of reagents and apparatus dimension, miniaturization could directly result in faster time-to-result processes [32].

1.3 Microfluidic Technologies and Tissue Dissociation

The past decade has seen a rapid growth in studies seeking to harvest single cells from tissues, which has spanned across several biomedical research areas. This has been driven in part by the rise of single cell analysis techniques, such as flow cytometry, mass cytometry, and single cell sequencing, to identify and profile different cell subpopulations obtained from tissues [33]–[35]. For cancer, this has enabled assessment of tumor heterogeneity, metastatic potential, and the presence of rare cell types such as putative cancer stem cells [36], [37]. These insights obtained at the resolution of single cells are drastically changing our understanding of cancer, and in the future are poised to

revolutionize clinical diagnostics and inform personalized patient care [5], [16] In the field of tissue engineering, isolation of primary cells from tissues is critical for the creation of new constructs to replace damaged organs such as skin, liver, heart, pancreas, and kidney [38]–[41]. Finally, the goal of regenerative medicine is to utilize mesenchymal stem cells or various progenitor cells to heal or otherwise replace diseased areas of the body [42], [43]. A common theme unifying all of these applications is that they require viable single cells that remain as representative of their original phenotypic state as possible. Thus, there is a critical need to develop new technologies that will make it possible to liberate single cells from tissues in a rapid, gentle, and thorough manner.

Microfluidics and microfabrication have advanced the fields of biology and medicine by miniaturizing devices to the scale of cellular samples. With the help of microfluidic systems, desired qualities of miniaturized devices such as high throughput, cost efficiency, minimal sample requirement, process integrations, and point-of-care operations are made possible to achieve [44], [45]. The focus of microfluidic devices has been set on sample processing, including on-chip sample purification, cell sorting and lysis, and rare cell population separations [45]–[47]. However, little attention has been given to applications that would make single cell suspensions readily available.

1.4 Structure of the Dissertation

The remainder of this dissertation is organized as follows: in chapter 2, a microfluidic device designed to interface core tissue biopsies and on-chip digestion is introduced. In chapter 3, a microfluidic dissociation device designed to further dissociate digestion effluent to millimeter scale aggregates and singles cells is demonstrated. Chapter

4 explores dissociation optimization options in terms of channel width reduction and feature geometry characterizations using a novel polymeric film based fabrication technology. In chapter 5, a microfluidic filtration device is developed to further purify single cell content as the final step in the entire microfluidic lab-on-a-chip platform. Chapter 6 summarizes the work presented in previous chapters, and concludes this dissertation by presenting future directions and studies that could be investigated by future research.

CHAPTER 2 MICROFLUIDIC TISSUE DIGESTION

2.1 Introduction

A survey of current research shows that tissue digestion methods predominantly involve enzymatic digestion, mechanical treatments, or a combination of both [48]–[50]. Single cell suspension or mixtures of single cells and millimeter scale aggregates are typically achieved from large tissue specimens, such as surgical resections and core biopsies, through a combination of mincing and enzymatic digestion. Mincing is usually achieved through means of repeated cutting and grinding, while enzymatic digestion is more often than not performed on a multi-hour basis for thorough ECM digestions. Collagenase is currently the preferred enzyme, as it digests tissue's underlying ECM components without cleaving biomarkers of diagnostic interests. However, the mild nature of collagenase typically requires prolonged incubation times, which can negatively affect cell viability and molecular expression profiles.

Mechanical mincing is seen as another means of harvesting single cells or small cell aggregates from tissues. Typically, enzymatic digestion is further augmented by subjecting samples to vortexing and repeated pipetting to mechanically liberate individual cells. Lacking control, these methods generate poorly defined shear flow environments, resulting in large variability in their end products. Thus, current tissue digestion methods are far from ideal, and there is clearly an opportunity for new technologies to dramatically improve the gold standards. To address this, areas of focus should be set to reducing or eliminating the dependence on proteolytic enzymes, shortening processing time, better

defining hydrodynamic environment involved in mechanical dissociation, and improving recovery viability and efficiency.

Microfluidic technologies has emerged as simple yet powerful methods for processing and manipulation cellular samples at the microscale [44], [45]. However, only a few microfluidic devices have designed to have the ability to process cell aggregates or tissues. The microfluidic cell dissociation chip (μ-CDC) was designed to break down neurospheres under fluid flow using a micro-pillar array, but it could only accommodate aggregates that were at most 200-300 μm in diameter yet still suffered from severe clogging issues [48]. The Biogrid was another such device developed to address this issue by mechanically cutting neurospheres using sharp silicon knife-edges placed across the device cross-section [49]. While this is a more effective approach, mechanical cutting in this fashion was harsh and only resulted in smaller aggregates, not single cells. To date, full scale tissue processing have only been employed in a single microfluidic application, the culture and enzymatic digestion of rat liver biopsies [50]. However, approach taken by this device focuses heavily on tissue incubation, not dissociation. It also suffered from extremely low cell yields following prolonged digestion times.

2.2 Microfluidic Device for Rapid Digestion of Tissues into Cellular Suspensions

2.2.1 Device Design

Our device was designed to process 1 mm diameter x 1 cm length tissues, similar to core needle biopsies, directly into cell suspensions without the need for manual processing steps such as mincing with a scalpel. To achieve this goal, we devised three primary components for the device. First, there is a tissue chamber that holds the sample in place

while fluid containing proteolytic enzymes are passed over the surface. This was intended to promote sample mixing, enhance enzymatic activity, and apply hydrodynamic shear forces to mechanically dislodge cells. Chamber dimensions were 1.5 mm x 1 cm, which is the size of a Tru-Cut core biopsy needle. Chamber height was also similar to the size of the tissue at approximately 1 mm. The second feature is a series of fluidic channels located upstream of the chamber, which focuses the fluid into high velocity jets that are directed into the tissue. These jets concentrate hydrodynamic shear forces at discrete locations, breaking the tissue down mechanically and delivering proteolytic enzymes deep inside the tissue. This is analogous to manual mincing of the tissue with a scalpel, and therefore we have developed the term hydro-mincing. Finally, fluidic channels were also placed downstream of the sample chamber to act as a sieve that selectively retains larger pieces of tissue and cellular aggregates for further dissociation. Smaller aggregates and single cells can freely pass out of the device for collection, or potentially further microfluidic processing.

To establish the channel features, we started with the downstream sieves. We reasoned that spacing many channels evenly throughout the device cross-section would minimize back pressure, while also holding the tissue firmly in place. We chose a channel width of 500 μm, of which 7 channels could comfortably be spaced across the width of the tissue chamber. Note that 500 μm is slightly smaller than the 1 mm size scale tissue pieces typically achieved by scalpel mincing. Aggregates of the size would also be ideal for directly inputting into our branching channel array dissociation device [51]. For the upstream channels, the goal was to achieve efficient hydro-mincing. Using fewer channels would generate stronger fluidic jets, but would also cover less of the tissue cross-section, which

would lead to higher device back pressures. Since these are competing factors, we chose to use channel number as a test variable and created devices with 3, 5, and 7 upstream channels. As for channels size, smaller widths would generate stronger, more concentrated fluidic jets. Therefore we chose 200 μm, which was the smallest feature resolution that we could reliably achieve with our laser-based fabrication method. Schematics of the tissue digestion device are shown in Figure 2.1. Computational fluid dynamics simulations were also performed using COMSOL Multiphysics software (COMSOL, Burlington, MA) for each upstream channel number using a flow rate of 1 mL/min (Figure 2.1B). These simulations were performed with and without a model tissue obstruction within the chamber. As expected, the design with 3 upstream channels generated the highest fluid velocities, or strongest hydro-mincing "cuts." Increasing channel number provided weaker "cuts," but better coverage of the tissue.

Devices were fabricated in hard acrylic sheets. The tissue chamber and channel features were laser-etched in acrylic sheets (Figure 2.1C). Laser power and raster speed were controlled to achieve a depth of approximately 1 mm, establishing the channel height. A second layer of acrylic was tapped and fitted with hose barbs to connect inlet and outlet tubing. Finally, a polydimethylsiloxane (PDMS) gasket was sandwiched between the acrylic layers to provide a watertight seal. Note that the deformable nature of PDMS, and possibly the tissue itself, should alleviate flow and backpressure issues related to the tissue initially blocking the flow path. Finally, the device was held together by 6 nylon screws. A fully assembled device is shown in Figure 2.1D, and the experimental setup is shown in Figure 2.1E. For this initial work, we used a peristaltic pump to recirculate fluid through the device to conserve proteolytic enzyme solution. Alternative operating procedures using

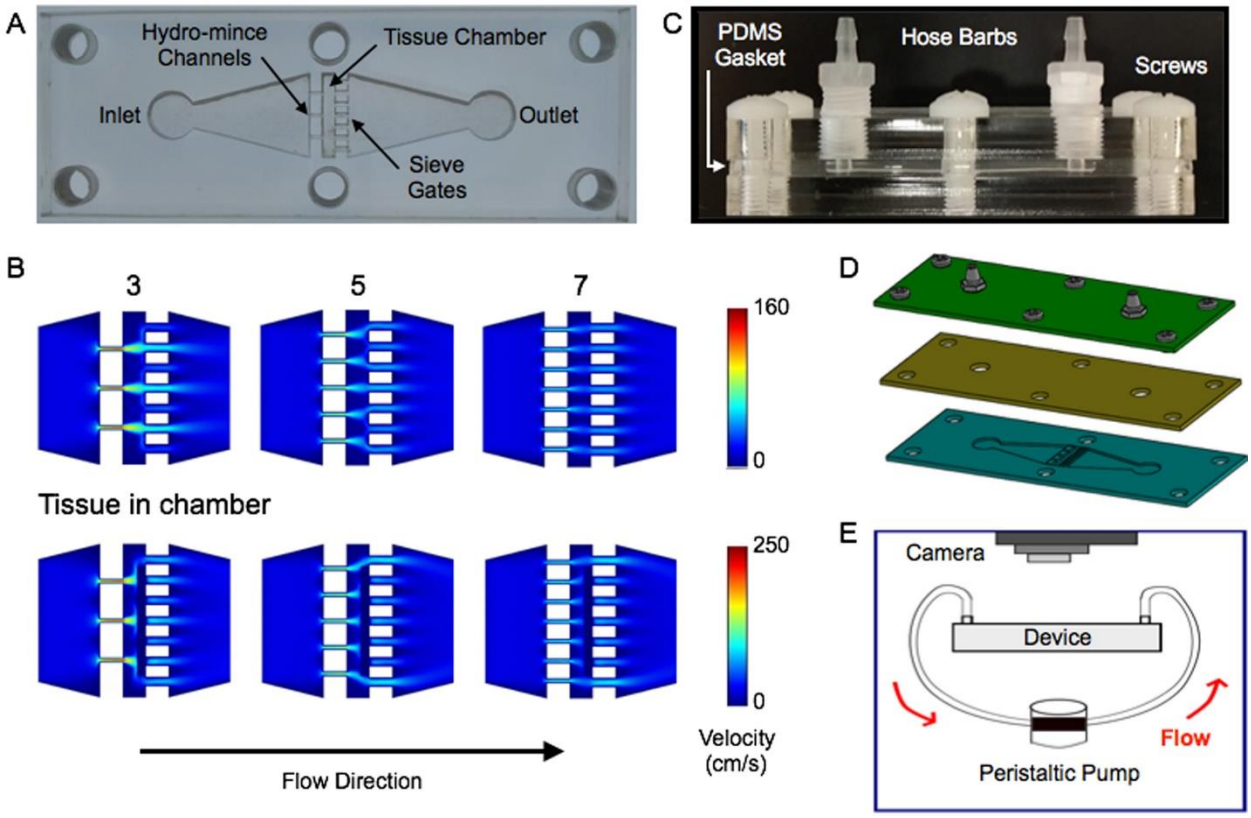

Figure 2.1. Microfluidic digestion device design and operation. (A) Image of laser-etched acrylic sheet containing the chamber for loading tissue samples and fluidic channels including upstream (left) for hydro-mincing and downstream (right) sieves. (B) Finite-element fluid dynamics simulations showing velocity profiles in devices with different numbers of hydro-mince channels. Results are shown with the chamber empty and partially blocked by a model tissue. Fewer hydro-mince channels will generate stronger fluidic jets to shear the tissue, but with less overall coverage. (C, D) Full digestion device shown in (C) side and (D) exploded views, with a PDMS gasket layer sandwiched between two acrylic sheets. Hose barbs were added to the top layer and nylon screws were used to hold the device together. (E) Experimental set-up for digestion experiments. Flow was driven by a peristaltic pump and tissue digestion was visually monitored with a camera mounted above the device.

continuous flow, or recirculation with removal of sample, could also be explored. A camera was mounted above the device to monitor the progress of tissue digestion.

2.2.2 Initial Device Optimization using Beef Liver Tissues

Performance of the microfluidic digestion device was first evaluated using beef liver as the sample tissue. Model tissue cores were extracted using a Tru-Cut biopsy needle and

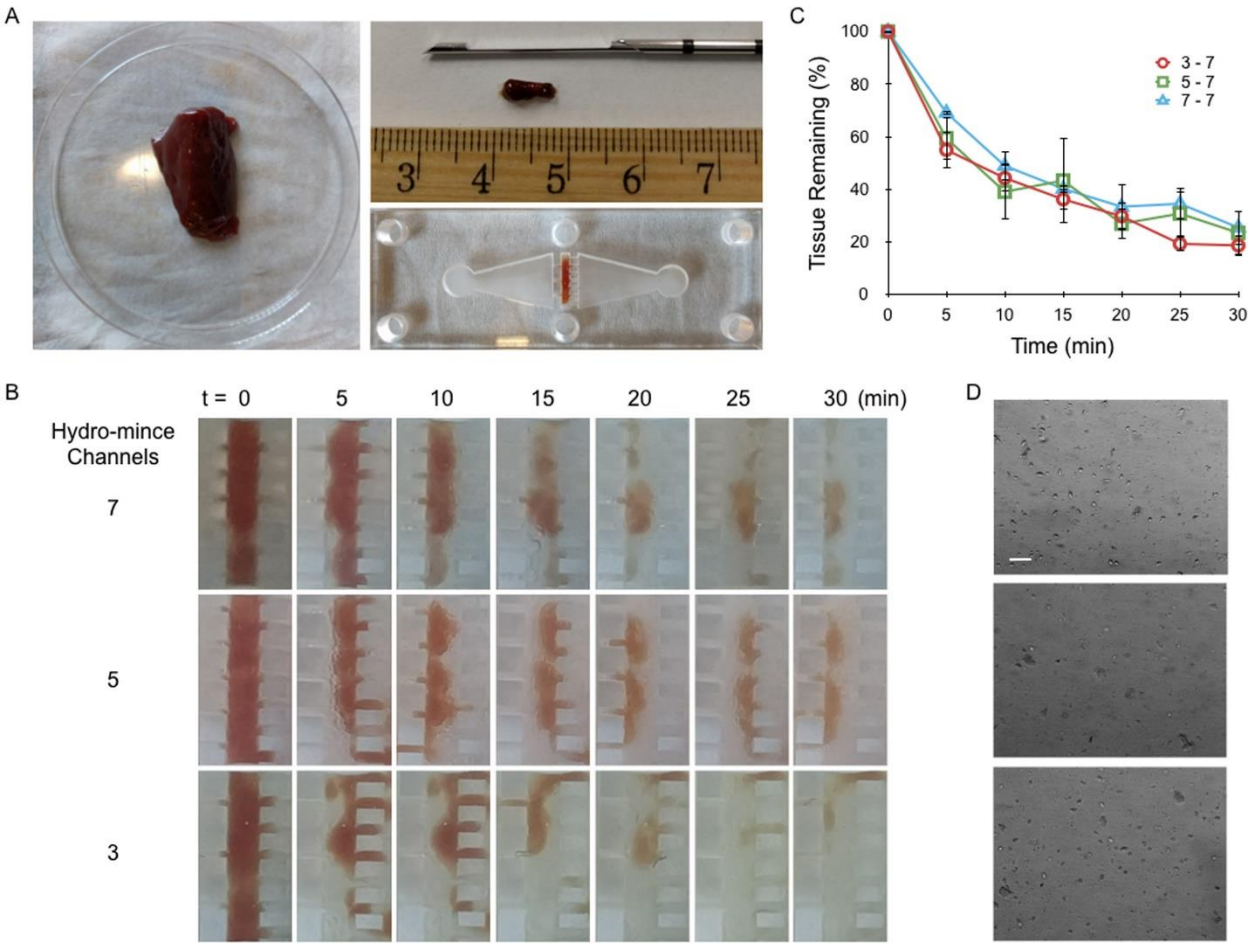

Figure 2.2. Digestion device optimization using beef liver cores. (A) Model tissue cores were obtained using a Tru-Cut biopsy needle and placed inside the tissue chamber. (B) Time-lapse images of tissue digestion for devices with 3, 5, and 7 hydro-mince channels. The fluid contained collagenase, and was pumped through the device at 20 mL/min. (C) Tissue loss was quantified from images based on mean gray value and overall tissue area. Trends were similar, but results were most consistent for 3 hydro-mince channels. (D) Micrographs of device effluents after 30 min operation. Scale bar is 100 μm. Error bars represent standard errors from at least three independent experiments.

loaded into the sample chamber (Figure 2.2A). Devices were then primed with PBS buffer containing collagenase enzyme, sealed, and flow was initiated at 20 mL/min using a peristaltic pump. Digestion progress was monitored by acquiring images every 5 min using the camera mounted above the device, and experiments performed for a total of 30 min (Figure 2.2B). After each image was acquired, flow was briefly reversed to clear the downstream sieve channels of tissue, before switching back to resume standard operation.

We observed that tissue migrated into the downstream channels more for the 3 upstream channel device, reflecting the higher hydrodynamic forces being generated. Images were processed using ImageJ and MATLAB to assess the amount of liver tissue remaining in the device at each time point based on tissue area and pixel density (Figure 2.3). Digestion profiles are plotted in Figure 2.2C, after normalizing by initial tissue mass. Results were similar for all three devices, with a dramatic 40% tissue decrease during the first 5 min, followed by a more gradual decrease of ~10% per additional 5 min interval. The initial drop primarily related to diminished pixel intensity, which may have reflected general tissue debulking or washing out of red blood cells. The second, gradual phase of digestion correlated with a loss of tissue area. After 30 min, approximately 80% of the tissue had

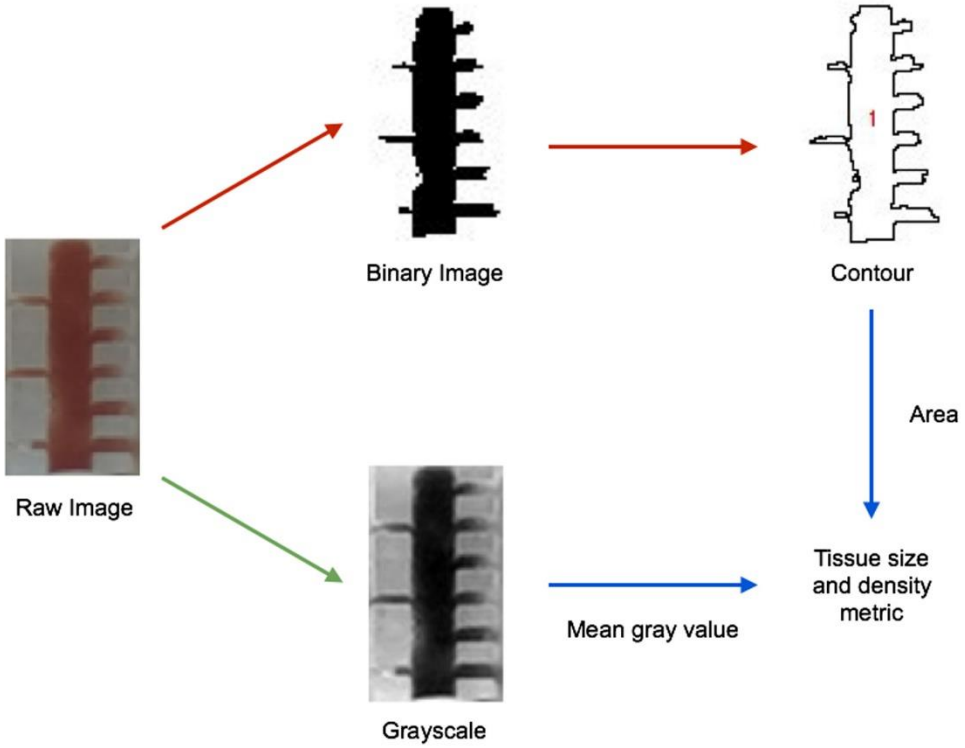

Figure 2.3. Image processing algorithm to monitor tissue digestion. Images were analyzed for tissue size and density to quantify changes during digestion within the device. First, raw images were separately converted to binary (red arrow) and grayscale (green arrow) images to outline the contour and quantify mean gray value, respectively. The area within the tissue contour was then calculated, and multiplied by mean gray value to obtain a single metric accounting for tissue size and density.

been removed from all three of the device designs. However, the device with 3 upstream channels provided the most consistent results, particularly at later time points, and thus was chosen for further evaluation. Representative micrographs of device effluents collected after 30 min of device operation are shown in Figure 2.2D. For all cases, sample effluents primarily comprised a mixture of larger tissue aggregates and smaller red blood cells.

2.2.3 Evaluation of Cell Suspensions Obtained from Fresh Mouse Organs

Next we tested the 3 hydro-mincing channel design using freshly resected murine liver and kidney samples. These live tissues better represent samples that will be used in future applications, and the resulting cell suspensions can be directly assayed for quality. Moreover, liver cells are well known to be exceptionally fragile [38], while kidney is considered to be a difficult tissue to dissociate due to high stromal content and structural elements such as add [40], [41] Immediately after harvesting, tissues were cut into approximately 1 cm x 1 mm x 1 mm pieces with a scalpel (Figure 2.4) and weighed. Digestion device experiments were then conducted as described for beef liver, with collagenase recirculated for either 15 or 30 min before sample collection. Images were again taken every 5 min and processed to monitor tissue loss, which was similar to beef liver (Figure 2.2). Controls were further minced with a scalpel into approximately 1 mm^3 pieces before digesting with collagenase for 15, 30, or 60 min in a conical tube. These samples were constantly agitated, and vortexed every 5 min. A separate control was included in which the tissue was not minced, only digested for 30 min. Following digestion, device-processed and control samples were mechanically treated by vortexing and pipetting, filtered through a 70 μm cell strainer, and treated with DNase to remove

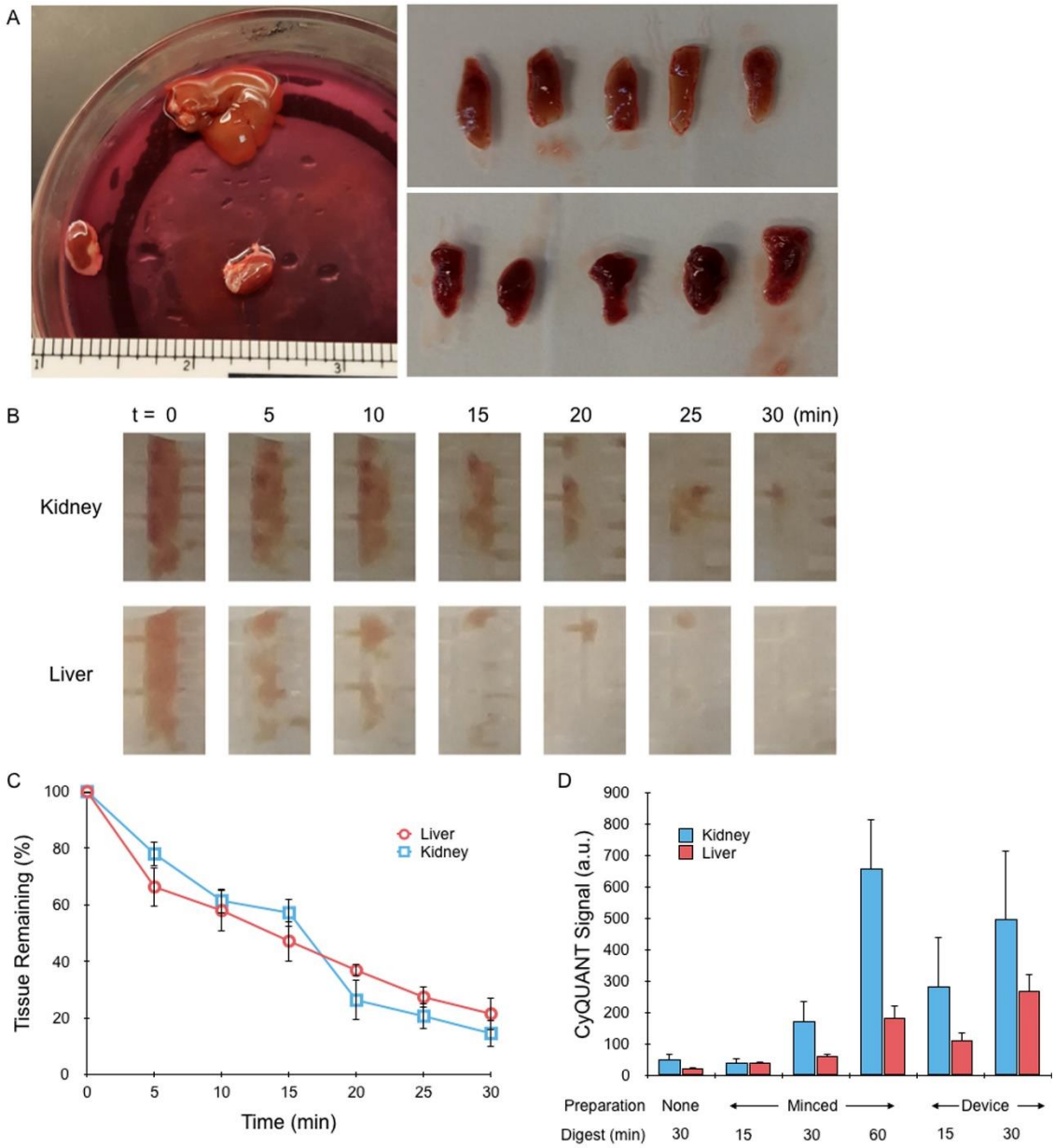

Figure 2.4. Mouse kidney and liver tissue imaging and CyQUANT data. (A) Mouse liver (top) and kidneys (bottom) were freshly harvested and cut into 1 cm long x 1 mm diameter pieces and placed within the device sample chamber. (B) Time-lapsed images of tissue digestion for device containing 3 hydro-mince channels. Tissue size and density both decreased over time as digestion progressed. (C) Tissue loss was quantified from images based on mean gray value and overall tissue area, with liver and kidney samples demonstrating similar trends. (D) CyQUANT assay was used to directly quantify cell suspensions obtained by digestion only, scalpel mincing and digestion, or device treatment lasting for a total of 15, 30, or 60 min. CyQUANT signal increased with treatment time, and was higher overall for kidney samples. Signals from device treated samples were consistently higher than minced controls, similar to gNDA and cell counting results presented in Figure 3 of the main text. Error bars represent standard errors from at least three independent experiments.

extracellular DNA. Cellular content was then assessed based on total genomic DNA (gDNA) that could be extracted using a QIAamp DNA kit. For minced controls, extracted gDNA progressively increased with digestion time (Figure 2.5A). Kidney samples yielded approximately 100 ng gDNA per mg of tissue after 60 min digestion, while liver was less than half this value. Slightly less gDNA was obtained from the unminced controls, but differences were not significant. Device treatment yielded dramatically more gDNA than controls when compared at the same digestion time. The difference was approximately 5-fold for both tissue types after 15 min, and 3 to 4-fold after 30 min. Moreover, device treatment produced comparable, or even more, gDNA than the control at the next longer digestion time point. The most striking result was for kidney, as the 30 min device treatment yielded 50% more gDNA than the 60 min minced control. Thus, the microfluidic digestion device can improve digestion efficiency while also shortening digestion time. DNA was also assessed within intact cellular suspensions using the CyQUANT assay, which corroborated gDNA results (Figure 2.4). Finally, a portion of recovered cellular suspensions was treated with red blood cell lysis buffer before quantifying cell number with an automated counter and visualizing the cells under phase contrast microscopy. Cell counts, which primarily reflected single cells but may also include small aggregates, were similar to gDNA results (Figure 2.5B). The main difference was that liver now provided values that were comparable to kidney. This suggests that a significant portion of kidney cells may have remained in aggregates that could have passed through the cell strainer and be lysed to obtain gDNA. Alternatively, the cell counter may have detected more debris in liver suspensions, which was seen in micrographs for both minced controls and device treated samples (Figure 2.5C).

2.2.4 Analysis of Cell Types, Numbers, and Viability using Flow Cytometry

The final evaluation focused on determining single cell numbers and viability. Fresh mouse kidney and liver samples were prepared and digested as described in the previous section, except the unminced control was removed and a 10 min device treatment was added. Digested cellular suspensions were filtered through a 40 μm cell strainer and labeled with a panel of four fluorescent probes: CellMask Green to stain phospholipid cell membranes, Draq5 to stain DNA within all cells, 7-AAD to stain DNA only within dead cells

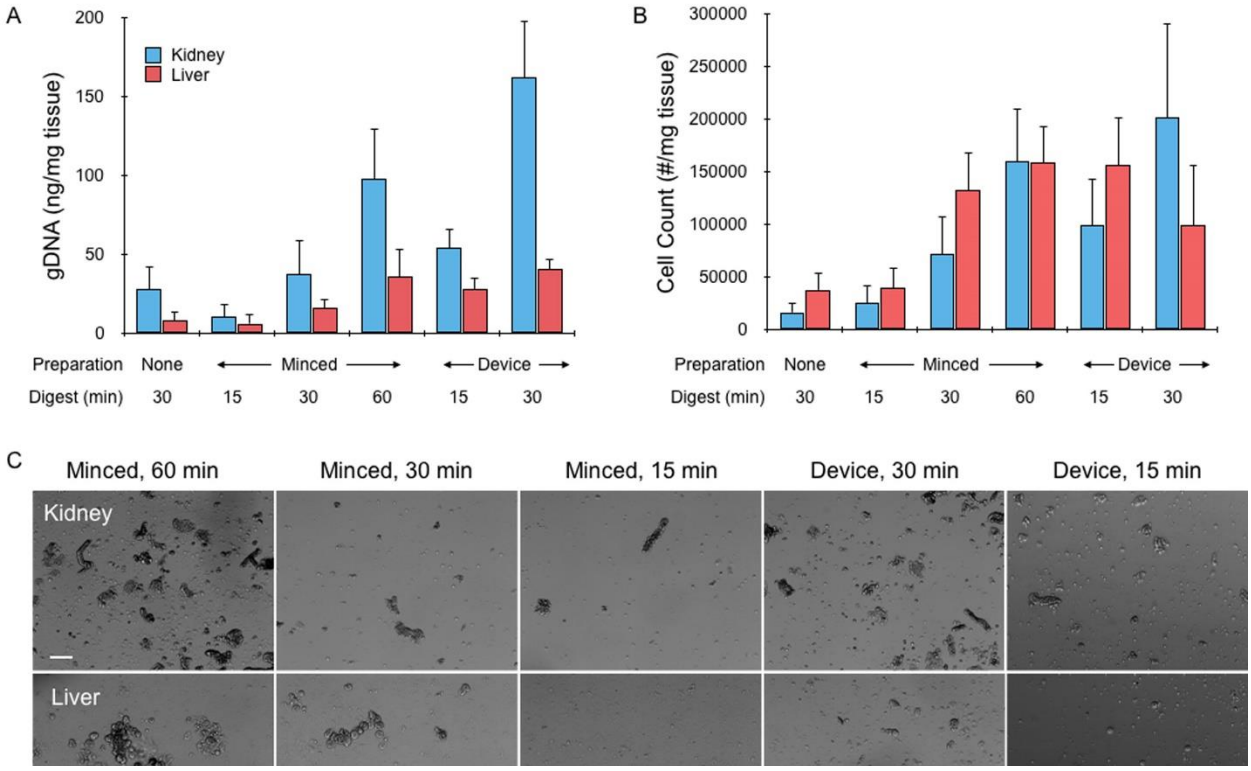

Figure 2.5. Cell recovery from fresh mouse kidney and liver tissues. (A) Genomic DNA (gDNA) was extracted and quantified from cell suspensions obtained by digestion only, scalpel mincing and digestion, or device treatment lasting for a total of 15, 30, or 60 min. gDNA increased with treatment time, and overall was higher for kidney samples. Device treatment consistently provided more gDNA than minced controls at the same time point, and even the next longer time point in most cases. (B) Cell counter results, showing that single cell numbers largely matched gDNA findings. However, values for liver were now similar or even higher than kidney, suggesting that the latter may have had more cells in small aggregates or clusters. (C) Micrographs of minced controls and device effluents, which corroborated recovery numbers. Scale bar is 100 μm. Error bars represent standard errors from at least three independent experiments.

with disrupted plasma membranes, and CD45 to stain leukocytes (Table 2.1). This panel enabled distinction of tissue cells from non-cellular debris, anucleated red blood cells, and leukocytes, while simultaneously assessing viability. Stained cell suspensions were analyzed with a BD Accuri Flow Cytometer to obtain the number of each cell type using the gating protocol described in the methods section and shown in Figure 2.6. Comparing the relative numbers for each cell type (Figure 2.7A and B), red blood cells constituted the majority of all but the minced control that was digested for 15 min. Unexpectedly, red blood cell percentage increased as the tissue was digested more thoroughly, although this effect was minor. Leukocyte percentage remained stable, decreasing slightly with digestion time. Tissue cell counts, which are expected to predominantly be epithelial, were quantified for kidney and liver samples and are presented in Figure 2.7C and D; respectively. Tissue cell numbers were 2 to 5 times higher for kidney than liver, with both tissue types showing a dramatic increase with digestion time for the minced controls. This increase was more than an order of magnitude between 15 to 30 min, and 5-fold between 30 to 60 min. With device treatment, there was little change between 10 and 15 min time points, although 10 min was associated with high variability for kidney samples. Extending processing time to 30 min increased cell number by only approximately 50% for both tissue types. Comparing

Table 2.1. Flow cytometry probe panel.

Assay	CellMask Green (Lipid membrane)	Draq5 (Nucleus)	CD45-PE (Leukocytes)	7-AAD (Dead cells)
Red blood cells	+	-	-	-
Leukocytes	+	+	+	+/-
Tissue cells	+	+	-	+/-

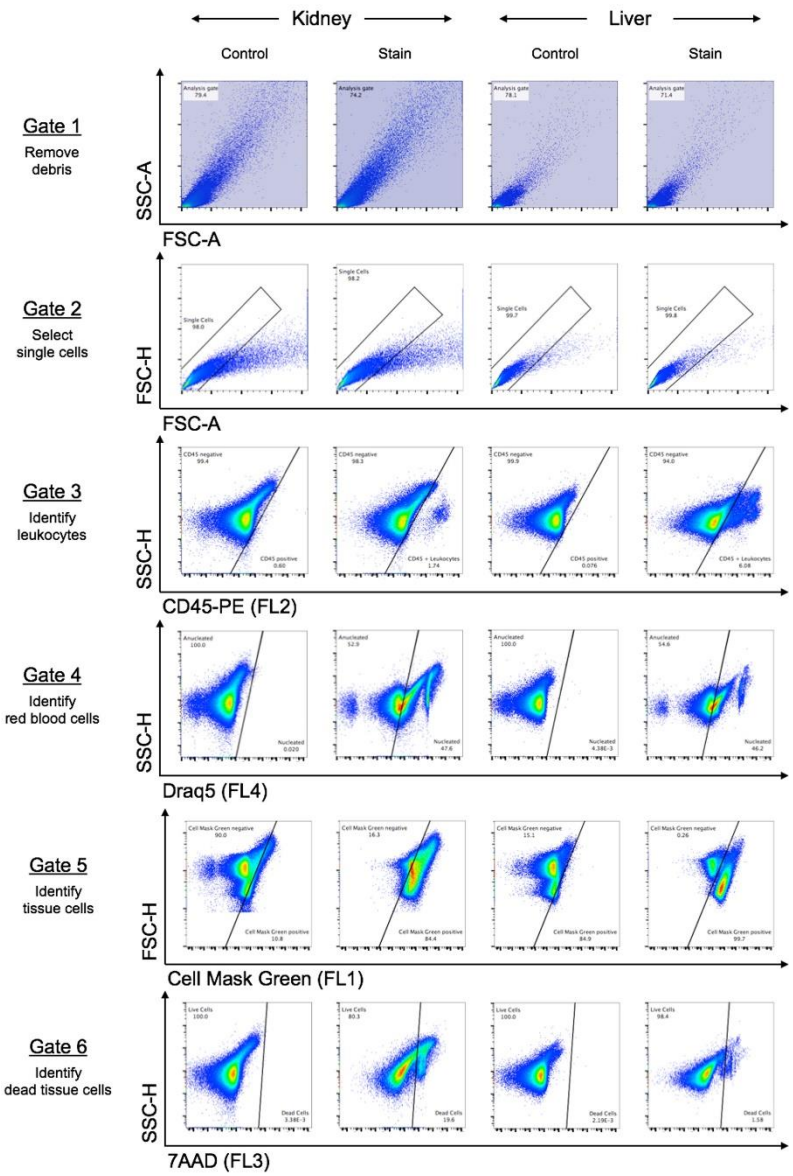

Figure 2.6. Flow cytometry gating scheme. Cell suspensions obtained from digested mouse liver and kidney samples were stained with the four probe panel listed in Table 1 and analyzed using flow cytometry. Controls were treated only with an isotype matched (IgG2b), PE-conjugated antibody. Acquired data was assessed using a sequential gating scheme. First, an FSC-A vs. SSC-A gate (Gate 1) was used to exclude debris near the origin. Gate 2 was based on FSC-A vs. FSC-H, and was used to select single cells. Gate 3 distinguished CD45+ leukocytes based on CD45-PE signal in FL2-A vs. SSC-H plots. The CD45- cell subset was further divided into anucleated RBCs and nucleated tissue cell subsets based on signal from the Draq5 nuclear stain in FL4-A vs. SSC-H plots. The cellularity of nucleated tissue cells of interest was validated based on signal of the cell membrane dye Cell Mask Green in FL1-A vs. FSC-H plots. Finally, live and dead tissue cells were discriminated based on 7-AAD signal in FL3-A vs. SSC-H plots. All gates were established using the minced control that was digested for 60 min. Heat treatment was used to confirm appropriate 7-AAD signal for dead cells.

to the minced controls, device treatment again provided superior results at the same digestion time point. For kidney, cell number differences were 30-fold at 15 min and 4-fold at 30 min. Differences were about half these values for liver. Furthermore, 15 min device treatment yielded similar or better results than the minced control that was digested for 30 min. However, the minced control that was digested for 60 min now provided the highest cell numbers, exceeding the 30 min device treatment by 50% for kidney and 100% for

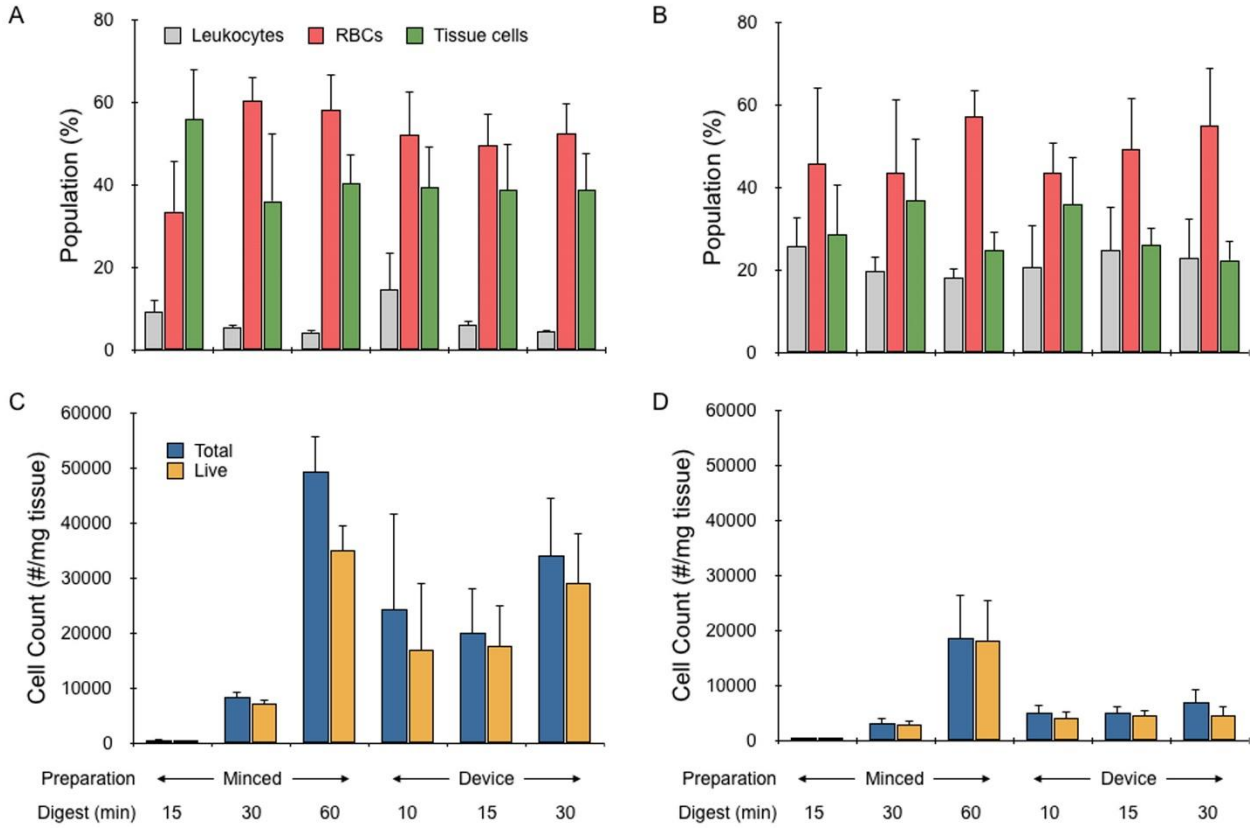

Figure 2.7. Single cell analysis of mouse kidney and liver cell suspensions. Flow cytometry was used to identify and quantify the number of leukocytes, red blood cells, and single tissue cells in the suspensions obtained from minced controls or device treatment. (A, B) Relative numbers of each cell type are shown for (A) kidney and (B) liver samples. Population compositions remained similar across all minced control and device conditions, with red blood cells comprising the highest percentage. (C, D) Total and live tissue cell numbers per mg of tissue were determined for (C) kidney and (D) liver samples. Tissue cell recovery increased with digestion time for minced controls, but did not change significantly with device processing beyond 10 min. Importantly though, all device conditions yielded more cells than minced controls that were digested for up to 30 min. Viability remained >80% for all but the longest time points, which reached as low as 70%. Error bars represent standard errors from at least three independent experiments.

liver. This finding is in contrast to the gNDA results, particularly for kidney, but generally consistent with CyQUANT and cell counter data. Thus, a significant portion of the additional cells liberated by the digestion device may reside within small aggregates or clusters, which would be reasonable considering the smallest channel feature size is 200 μm. Finally, we assessed viability using a DNA dye that is excluded from healthy cells with intact membranes. Viability was approximately 80% for all kidney samples except the minced control that was digested for 60 min and 30 min device cases, which both dropped to 70% (Figure 2.8). For liver, viability was approximately 90% for the minced controls, 80% for 10 and 15 min device treatments, and 70% for 30 min device treatment. The number of live tissue cells obtained from each condition is also presented in Figure 2.7C and D. For kidney, 30 min device treatment produced approximately the same number of live single tissue cells as the minced control that was digested for 60 min. The 10 and 15 min device treatments produced around half of this value, but in a fraction of the time. For liver, the number of live, single tissue cells did not increase with device treatment beyond 10 min. This was likely due to the fragile nature of liver cells, which may have been damaged or

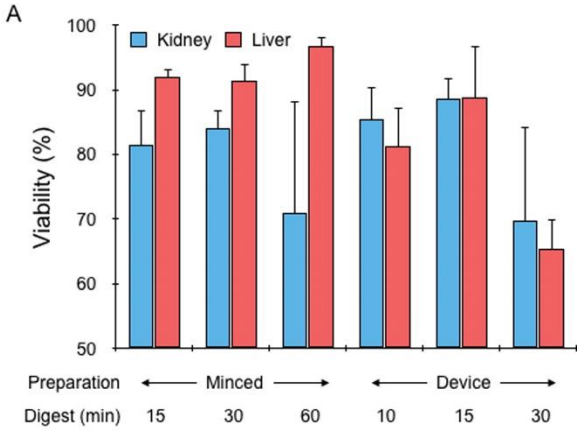

Figure 2.8. Mouse kidney and liver cell viability data. (A) Cell viability was similar for device treated conditions relative to minced counterparts, demonstrating minimal effect of device treatment. Error bars represent standard errors from at least three independent experiments.

fully destroyed while recirculating through the device. Overall, the microfluidic digestion device performed better for kidney samples despite the fact that this tissue type is generally considered to be tougher to dissociate. This is likely due to the combination of greater cell robustness and a higher potential for improvement, which the device was successfully able to exploit.

2.3 Materials and Methods

2.3.1 Fluid Dynamics Simulations

Flow profiles within device channels were simulated using COMSOL Multiphysics software. This involved coupling the Navier-Stokes equations and the continuity equation in finite element fluid dynamics simulations. Fluid flow was assumed to be laminar, and the no-slip boundary condition was enforced at the channel walls.

2.3.2 Device Fabrication

Digestion devices were designed using Onshape software. Fluidic channels and hose barb openings were laser etched using a VLS 4.60 60W CO_2 laser (Universal Laser Systems, Scottsdale, AZ). Channel designs were etched in 6" x 6" optically clear cast acrylic sheets (McMaster-Carr, Elmhurst, IL) that served as the bottom layer of the device. Hose barb openings were then tapped to provide threading. A gasket was prepared from PDMS (Ellsworth Adhesives, Germantown, WI) by casting a 5 mm slab and cutting with a scalpel. The device was assembled with the PDMS gasket placed between the top and bottom acrylic layers, and secured with nylon screws. The inlet and outlet of the device were connected to a peristaltic pump that was controlled by a custom-built Arduino Uno R3 microcontroller.

2.3.3 Tissue Models

Beef liver was purchased from a local butcher and tissue cores were extracted by using a Tru-Cut biopsy needle (CareFusion, Vernon Hills, IL). Briefly, the obturator was retracted to cover the specimen notch and the cannula handle was held firmly while the needle was inserted into the tissue. The obturator was quickly advanced as far as permitted to position the specimen notch in the tissue and the cannula handle was quickly advanced to cut the tissue. Tissue obtained in the specimen notch was then transferred to device using tweezers. Mouse liver and kidneys were harvested from sacrificed C57B/6 or BALB/c mice (Jackson Laboratory, Bar Harbor, ME) that were deemed waste from a research study approved by the University of California, Irvine, Institutional Animal Care and Use Committee (courtesy of Dr. Angela G. Fleischman). Animal organs were cut with a scalpel into 1 cm long x 1 mm diameter pieces, and the mass of each was recorded. Mouse kidneys were sliced in a symmetrical fashion to obtain histologically similar portions.

2.3.4 Digestion of Tissue Samples

The digestion device was first primed with 200 μL collagenase type I (Stemcell Technologies, Vancouver, BC) and heated to 37°C inside an incubator to ensure optimal enzymatic conditions. Tissue was then placed inside the chamber, the device was assembled and secured with nylon screws, and flow was initiated at 20 mL/min with the peristaltic pump. Every 5 min, the flow was reversed to clear tissue from the downstream sieve gates. Device effluents were collected by pumping directly into a conical tube. Controls were digested in a conical tube, either with or without prior mincing with a scalpel into ~1 mm^3 pieces. Tubes were placed inside a 37°C incubator and gently agitated

on a rotating mixer. Every 5 min, the tubes were vortexed to mechanically disrupt tissue and maximize digestion. At the conclusion of digestion procedures, all cell suspensions were repeatedly vortexed and pipetted to mechanically disrupt aggregates and treated with DNase I (10 μL; Roche, Indianapolis, IN) at 37°C for 5 min.

2.3.5 Image Analysis to Monitor Tissue Digestion

During device operation, images of the tissue were captured every 5 min using a camera mounted directly above the device. Raw images were processed using ImageJ by first converting to binary to identify the borders of the tissue (Figure 2.3). Mean gray value was then determined within the tissue border, and multiplied by the area to obtain a single metric accounting for tissue size and density. Results at each time point were normalized by the initial value prior to the experiment, and presented as percent tissue remaining.

2.3.6 Quantification of DNA Recovered from Cell Suspensions

DNA content of digested cell suspensions was assessed by extraction and purification, as well as direct assessment within cells using a fluorescent DNA stain. For both cases, samples were first filtered using a 70 μm cell strainer to remove remaining tissue and large aggregates. Purified genomic DNA (gDNA) was isolated using the QIAamp DNA Mini Kit (Qiagen, Germantown, MD) according to manufacturer's instructions and quantified using a Nanodrop ND-1000 (Thermo Fisher, Waltham, MA). DNA within cells was labelled using the CyQUANT NF Cell Proliferation Assay Kit (Thermo Fisher, Waltham, MA) according to the manufacturer's instructions. Briefly, samples were suspended in HBSS supplemented with 35mg/L sodium bicarbonate and 20 mM HEPES and added to an opaque 96-well plate (Corning, Corning, NY) in triplicate. An equal volume of CyQUANT dye

was then added to each well, incubated at 37°C for 40 minutes under continuous mixing at 200 RPM, and fluorescence signal was quantified using a Synergy 2 plate reader (BioTek, Winooski, VT). Wells containing only HBSS and CyQUANT dye were used for background subtraction. gDNA and fluorescence intensities were normalized by the initial tissue mass.

2.3.7 Cell Counting and Imaging of Cell Suspensions

Digested effluents were collected, filtered using a 70 μm cell strainer, and incubated with red blood cell lysis buffer containing ammonium chloride, potassium carbonate, and EDTA (Biolegend, San Diego, CA) for 5 min at room temperature. Cell concentration was determined using a Moxi Z cell counter with type S cassettes (Orflo, Hailey, ID), and converted to cell number per mass of tissue using the total volume recovered and the initial tissue mass. Imaging was performed by transferring samples to a 12-well plate, waiting for 1 hour for the cells to settle, and capturing images using a Hoffman phase contrast microscope with a 4x objective.

2.3.8 Flow Cytometric Analysis of Single Cells

Digested mouse kidney and liver cell suspensions were evenly divided into FACS tubes (Corning, Corning, NY) and resuspended in FACS Buffer (1X PBS, pH 7.4 without Ca and Mg cations) supplemented with 1% BSA and 0.1% NaN_3. Samples were first stained with 0.5X CellMask Green (Thermo Fisher, Waltham, MA) and 2.5μg/mL anti-mouse CD45-PE monoclonal antibody (clone 30-F11, (BioLegend, San Diego, CA) for 20 minutes at 37°C and washed twice with FACS Buffer by centrifugation. Cells were then resuspended in FACS buffer supplemented with 12.5 μM Draq5 (BioLegend, San Diego, CA) and 5 μg/mL 7-AAD (BD Biosciences, San Jose, CA) and maintained on ice for at least 15 minutes prior to

analysis on an Accuri Flow Cytometer (BD Biosciences, San Jose, CA). An isotype matched, PE-conjugated rat monoclonal antibody (clone RTK4530, BioLegend, San Diego, CA) was used as a control. Flow cytometry data was compensated and analyzed using FlowJo software (FlowJo, Ashland, OR). Compensation was determined using the kidney and liver tissues that were minced with a scalpel and digested for 60 mi, which were aliquoted into four different preparations to obtain distinct positive and negative subsets for each probe. The four preparations included cell fractions with: 1) negative control CompBeads (3.0-3.4 μm diameter, BD Biosciences, San Jose, CA) and CellMask Green membrane stain, 2) RBCs lysed and CD45-PE antibody, 3) live and dead (heat-killed at 55°C for 30 min) cells with 7-AAD stain, and 4) Draq5 stain. Gates encompassing the positive and negative subpopulations within each compensation sample were inputted into FlowJo to automatically calculate the compensation matrix. Finally, a sequential gating scheme was used to identify different cell subpopulations. (Figure 2.6). A SSC-A vs. FSC-A gate was created to select all cellular events and exclude debris from further analysis. Multicellular aggregates were removed from the analysis population to focus only on single cells using an FSC-H vs. FSC-A gate. Leukocytes were first distinguished from the single cell population based on CD45 expression (FL2-A or PE vs. SSC-H). Anucleated red blood cells were distinguished by their absence of Draq5 nuclear stain (FL4-A or Draq5 vs. SSC-H). The cellularity of the final remaining single cells (CD45 negative, Draq5 positive) was confirmed by detecting cell membranes using CellMask Green stain (FL1-A or CellMask green vs. FSC-H). Finally, live and dead nucleated tissue cell percentages were discriminated based on 7-AAD signal (FL3-A or 7-AAD vs. SSC-H).

2.4 Conclusion

In this chapter, we have presented a new microfluidic device to isolate single cells from cm x mm-scale tissues using the combination of hydrodynamic shear forces and proteolytic digestion. Upon testing our microfluidic digestion device with kidney and liver tissue samples, we consistently observed improvements in recovery of DNA and single tissue cells relative to standard methods that require mincing with a scalpel. Device performance at short processing times was particularly exciting, as a 10 min treatment yielded results that were within 50% of scalpel mincing and digesting for 1 hour, but with improved viability. Recovery improvement were most striking for DNA, suggesting that the current device design may have left a significant number of cells within small aggregates or clusters. In future work, we will explore smaller channel dimensions to improve aggregate dissociation, or pair with another device such as our branching channel array with hydrodynamic micro-scalpels [51]. We did observe evidence that cells may have been damaged during initial tissue digestion, or more likely while repeatedly recirculating through the device, particularly for liver. Thus, next generation designs will seek to remove single cells as soon as they are liberated via filtration or another means of physical separation. Finally, we will pursue testing of additional tissues such as solid tumors from various cancer types for diagnostic purposes and other healthy tissues such as skin, heart, and fat for use in tissue engineering and regenerative medicine.

CHAPTER 3 MICROFLUIDIC TISSUE AND CELL AGGREGATES DISSOCIATION

3.1 Introduction

Recent evidence has pointed to a model in which tumors are viewed as an ecosystem consisting of a diverse array of cell types that work in concert to maintain homeostasis and drive further development [1]. This cellular heterogeneity has been identified as a key factor underlying tumor progression, metastasis, and the development of drug resistance [2]. Cell types can include neoplastic subpopulations with distinct genotypes and phenotypes (clonal evolution, hierarchical differentiation from stem-like precursors or cancer stem cells) [1], [3]. Host cells of diverse origins, including non-tumor epithelium, stroma, and immune subtypes, can also assist the tumor in different capacities [1], [4]. Tumor heterogeneity and the presence of key cell types such as cancer stem cells have become major focus areas in tumor biology and clinical diagnostics, and have changed the overarching problem in cancer from identifying general molecular drivers to achieving a more holistic understanding [5].

A major challenge to characterizing molecular and cellular information within solid tumors is the fact that specimens are three-dimensional tissues. Such a formation often hinders further downstream sample processing. Methods such as histology, immunohistochemistry, and fluorescence in-situ hybridization are clinical standards that provide morphological detail with sub-cellular resolution for intact tissues, but are low throughput and detection signals are difficult to quantitate and multiplex. Techniques that involve sample destruction such as genetic sequencing, microarrays, and mass spectrometry provide vast amounts of molecular information but fail to retain context with

respect to the different cellular components that constituted the original sample. Cell-based analysis platforms such as flow cytometry are attractive because they offer high-throughput and multiplexed information at the single cell level, allowing the entire population to be analyzed. Other applications include mass cytometry [15], microfabricated magnetic and optical detectors [16]–[18], cytology [19], single cell gene sequencing [20], as well as physical measurements such as density and deformability [21], [22]. The single cell format is also advantageous for isolating rare cell types such as cancer stem cells, metastatic precursors, or drug resistance clones for more detailed study [23]–[26]. The disadvantage of cell-based techniques is that the tissue must first be broken down into single cells, which requires considerable expenditure of time and effort. Moreover, the processes used to achieve dissociation can potentially damage or otherwise bias samples. Thus, tissue dissociation remains a major barrier to the application of single cell techniques to solid tumor specimens.

Tumor tissues are currently dissociated into single cells using proteolytic enzymes that digest cellular adhesion molecules and the underlying extracellular matrix. Larger tissue specimens are first minced with a scalpel into approximately 1-2 mm pieces, and then an enzyme or enzyme cocktail is applied. Trypsin is a broadly reactive protease that is very efficient, typically requiring only short incubation times on the order of 15 minutes [16], [19]. But trypsin can also cleave cell surface proteins that may be needed to provide important diagnostic information or regulate cell function. An important example is CD44, which is commonly used as a cancer stem cell marker and has been shown to be sensitive to trypsin cleavage [52]. Collagenase is a milder enzymatic alternative that digests collagen within the underlying extracellular matrix, leaving cells largely undisturbed. For this

reason, collagenase has been employed in most studies seeking to identify and isolate cancer stem cells via CD44 or other biomarkers [23]–[26]. However, collagenase requires long incubation times on the order of 1 to 2 hours, which could negatively affect cell viability or allow for changes in molecular expression, and dissociation is incomplete, as large aggregates must be filtered. Alternative enzymes such as hyaluronidase or thermolysin [23], or even non-enzymatic options such as the calcium chelator ethylenediaminetetraacetic acid (EDTA), can also be employed to augment dissociation. Following initial enzymatic or chemical treatment procedure, samples are subjected to fluid shear forces to mechanically liberate individual cells. This is typically achieved by vortexing and repeated pipetting of the sample. These methods generate poorly defined shear flow environments that do not allow control over sample exposure, potentially resulting in variations among samples or across different laboratories. The gentleMACS™ Dissociator is a commercial system that has been developed to standardize mechanical dissociation [27], but use with tumor specimens is not common and performance is not well documented. The final step is to remove remaining large aggregates and debris by filtering, which results in loss of sample. Taken together, current tumor tissue dissociation methods are labor intensive, time consuming, incomplete, and rely on harsh or prolonged proteolytic enzyme treatment. Thus, new technologies are critically needed to meet all of the following goals: improve dissociation efficiency to increase yield, maximize overall cell quality in terms of viability and molecular biomarker expression, decrease processing time from hours to minutes, and automate workflow to enable point-of-care operation and directly connect to downstream processing and analysis tasks. Automation is particularly critical for clinical applications, where the patient is separated from pathology facilities

where the necessary processing infrastructure can be found. Tumor specimens cannot be preserved prior to dissociation because the cells would be locked together or become too fragile. Consequently, achieving tumor tissue dissociation at the patient's bedside followed by immediate fixation or analysis of the resulting cell suspension would be powerful.

Microfabrication technologies have advanced the fields of biology and medicine by miniaturizing devices to the scale of cellular samples. In particular, microfluidic systems have enabled precise manipulation of cells and other reagents to achieve systems with high throughput, cost efficiency, minimal sample requirement, integration of multiple procedures on the same device, and point-of-care operation [44], [45]. Sample processing has been a major focus area, specifically for on-chip cell purification, sorting, and lysis [45]–[47]. However, little attention has been given to processing tissues. One example is the Biogrid, which employs a 100 μm mesh with sharp edges to cut large cell aggregates into smaller units that still contain numerous cells [49]. To date, a microfabricated fluidic device for dissociating tissue into single cells has not been described. Developing such a device is challenging because it would need to operate across a large range of length scales, from millimeter tissues down to tens of micron cells. Furthermore, the device would need to maintain a flow through format that is ideal for integrating the resulting single suspension directly with downstream operations such as purification, sorting, physical analysis [21], [22], and probe detection [16]–[18] to achieve point-of-care tumor cell analysis platforms.

In this chapter, we present a novel microfabricated fluidic device for processing tumor tissue samples into single cells. The device employs channel features ranging in size from millimeters down to hundreds of microns. The channels also contain constriction and expansion regions that generate hydrodynamic fluid jets with varying size scales and shear

force magnitudes to progressively break down tissue fragments and cell aggregates. We believe this design will enable gradual disaggregation, thereby maximizing cell yield without causing extensive cell damage. Moreover, the flow-through format will enable rapid processing and is ideal for connecting to downstream fluidic operations. Using cultured tumor tissue models of varying complexity, we show that the microfluidic dissociation device significantly augments enzymatic digestion by increasing the number of single cells liberated. This is because the device is significantly more effective at dissociating small clusters, while limiting cell destruction or holdup. We also demonstrate that efficient dissociation can be obtained under enzyme-free conditions, in which the device operates in combination with EDTA treatment or even alone for certain samples. Thus, our microfluidic device significantly improves tumor tissue dissociation efficiency, resulting in higher quality single cell suspensions even under enzyme-free conditions that better maintain molecular expression levels. Furthermore, these results were obtained in less than ten minutes total processing time. We envision our device operating as a standalone unit or as the first component of an integrated and automated platform, capable of processing tumor or other types of tissue samples that are 1 mm in size or less. This could include, but is not limited to, laboratory-scale tissue models, small volume specimens such as fine needle aspirate (FNA) biopsies, and larger surgical or core biopsy specimens that have been finely cut with a scalpel. The improved dissociation capabilities will help promote laboratory and clinical investigations that utilize powerful cell-based detection and isolation platforms, thereby advancing our understanding of cancer biology and enabling molecular diagnostics in clinical settings.

3.2 Microfluidic Device for Mechanical Dissociation of Cancer Cell Aggregates into Single Cells

3.2.1 Device Design

The concept for our dissociation device is to employ a series of branching channels that resemble a physiological microvascular capillary network or reported microfluidic droplet splitters [53]. We believe this design will make it possible to process tissue fragments and cell aggregates of different length scales in an effective but gentle manner. The device has a total of 7 stages that are each approximately 1 cm in length, and with branch points placed at the end of each stage (Figure 3.1A). The first stage is a single channel with a minimum channel width of 2 mm. We have chosen for channel dimensions to decrease by half after branching, thus the total width across each stage is maintained as a constant throughout the device. We have included an additional design feature to facilitate dissociation, continuous expansion and constriction of the channel width. This will modulate fluid velocity, actively mixing the sample and generating shear forces across cell aggregates. The expansion and constriction regions are connected by smooth curved lines to avoid turbulent mixing and the generation of microvortices that can trap cells in recirculating flows [54]. The maximum width in the expansion region is 3-fold greater than the minimum width in the constriction, and this ratio is maintained throughout the device. Finally, constriction regions are separated by a distance equal to the expansion region width, which results in an increase in the number of constrictions per channel with each stage. Since channel width dimensions decrease by half as channel number doubles, and channel height is constant at 300 μm, average velocity (v_{avg}) is constant in each channel

throughout the device. Channel specifications for each stage are listed in Table 3.1. For reference, the orifice diameter for standard P-1000 pipette tips that are commonly used to shear tumor tissue samples is approximately 1 mm.

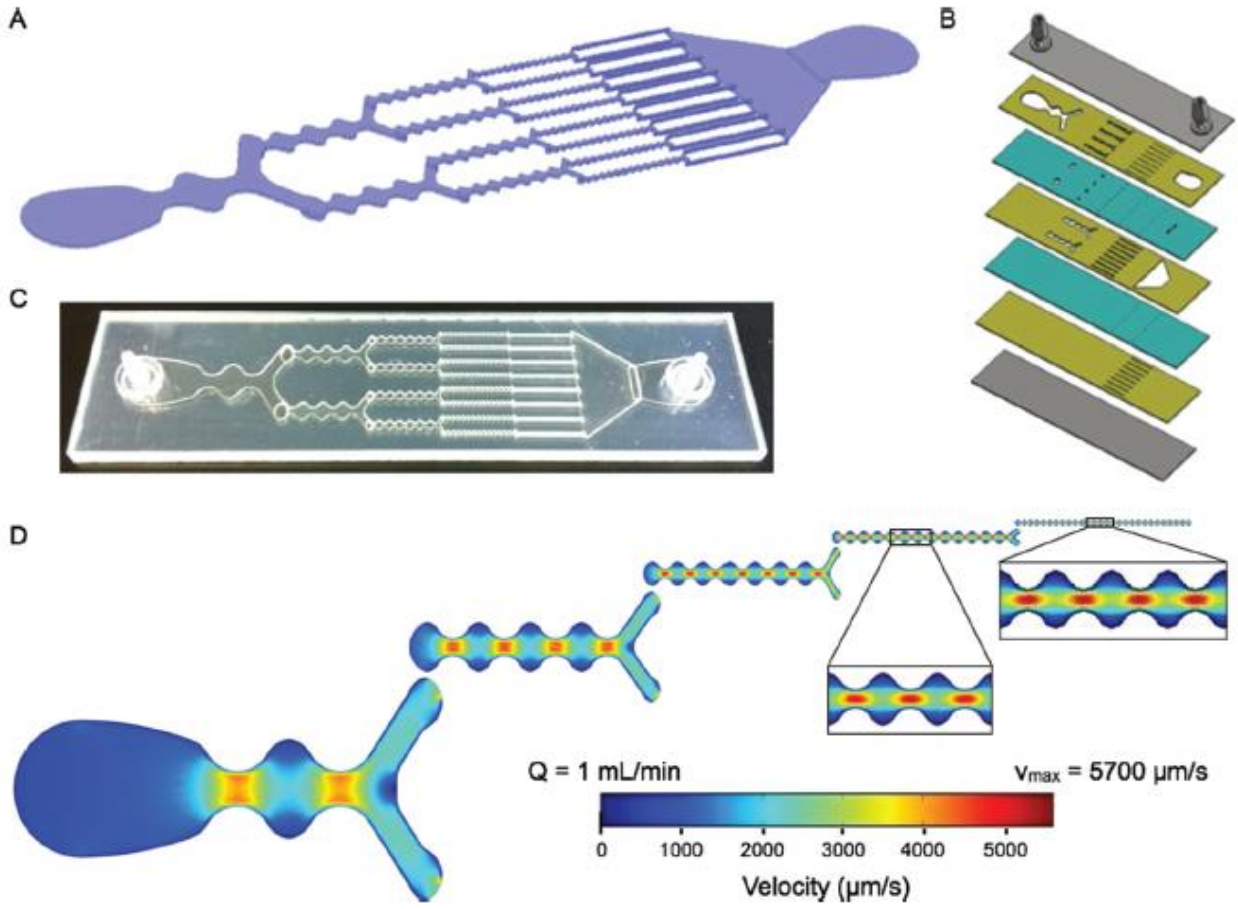

Figure 3.1. Microfluidic dissociation device. (A) Schematic showing the branching channel design containing alternating constriction and expansion regions. Channel dimensions are listed in Table 3.1. (B) Expanded view for the laminate format containing 7 plastic layers. Features are etched in plastic using a laser, with the channels placed on three layers (gold) that are connected by *via* layers (teal). Two layers are used to seal the device (gray), with hose barbs placed in the top layer to serve as the inlet and outlet. (C) Picture of a fabricated microfluidic device. (D) Finite-element fluid dynamics simulations showing velocity profiles in each stage of the device. Fluidic jets are generated in the constriction regions with high flow velocities and shear stresses. The fluidic jets decrease in size scale and increase in shear magnitude with each stage, leading to gradual dissociation of tissues and cell aggregates. Simulations were performed at 1 mL/min, and flow velocities and shear stresses are listed in Table 3.1.

Table 3.1. Channel dimensions and flow properties.

	Stage 1	Stage 2	Stage 3	Stage 4	Stage 5
Channels	1	2	4	8	16
Min. width (mm)	2	1	0.5	0.25	0.125
Constrictions	2	4	7	14	27
Re_{max} [a,b]	160	80	40	20	10
v_{max} [a,b] ($\mu m\ s^{-1}$)	4300	4600	5200	5300	5700
$\tau_{W,max}$ [a] (dyne cm^{-2})	0.4	0.9	2	4	9
τ_H [a] (dyne cm^{-2})	2.9	3.1	3.4	3.6	3.8
$\Delta P_{Channel}$ [a] (Pa)	50	40	45	60	160
ΔP_{Stage} (Pa) [a,c]	50	20	12	8	10

[a] All flow properties are given for $Q = 1$ mL min^{-1}. [b] $v_{avg} = 2800\ \mu m\ s^{-1}$. [c] $\Delta P_{Total} = 100$ Pa.

We chose to fabricate the device using a laminate approach, with channel features etched in hard plastic (polyethylene terephthalate, PET) using a laser. This format should provide a more robust product than alternative options that utilize photolithography and polydimethyl siloxane (PDMS), and thus better supports high flow rates and pressures that may be needed to effectively dissociate tissues. We employed multiple plastic layers, which were bonded with adhesive and pressure lamination. Consecutive device stages were placed on different layers and connected by *vias* that have a diameter equal to the minimum cross-section of the subsequent stage. This will maximize device strength and integrity, as well as change the direction of fluid flow to mix and agitate the sample between stages (Figure 3.1B). Seven layers were used in total, including three for channel features, two for *vias*, and two to seal the top and bottom. Channel height includes contributions from both the plastic layer (250 μm) and adhesive (~50 μm), and is approximately 300 μm.

While v_{avg} is constant in each channel, the continuous variations in width will result in complex, size-dependent velocity profiles. Therefore we have performed computational fluid dynamics simulations using COMSOL Multiphysics. This will be important for understanding the mechanisms of tissue dissociation achieved through hydrodynamic forces. We separately analyzed a single channel within each stage to simplify simulations and because the multi-layer laminate design is not continuous in the axial direction. However, we have confirmed that single channel outputs do closely match results obtained from consecutive, multistage simulations (Figure 3.2). Simulations were performed under laminar flow conditions, which are expected because changes in channel width are gradual and the Reynolds number remains less than 25 at all points in the device when operating at 1 mL/min flow rate. Maintaining laminar flow will be important to achieve well-defined flow properties and shear forces. Velocity profiles across the channel widths are shown in Figure 3.1D, viewed from the center of the height dimension. Flow velocity increases in the constriction regions to form discrete jets, with the maximum velocity (v_{max}) concentrated in the central region for all but the first stage. The magnitude of v_{max} is similar in each stage, but does increase slightly throughout the device. However, hydrodynamic shear force scales with the shear rate, which depends on the change in velocity (v_{max}) divided by the channel half-width. Thus, the fluidic jets increase in dissociation power as they become smaller in scale. We envision that these regions act as "hydrodynamic micro-scalpels" that become sharper and finer throughout the device, progressively breaking the tissue down into smaller aggregates and finally single cells. For this reason we left the minimum dimension of the final stage at 125 μm, significantly greater than the 10-20 μm diameter of typical epithelial cells. The shear stress generated across the device width (τ_W) was

calculated by multiplying the shear rate by the fluid viscosity, which was assumed to be the same as water. The shear stress across the height dimension (τ_H) can also be calculated using v_{max} and the half-height, which will remain constant in each stage. It should be noted that τ_H will exceed τ_W, even within the constriction regions, for the first 3 stages. Velocity and shear stress values are listed for each stage in Table 3.1. Note that physiological values for wall shear stresses in human blood vessels are in the range of 1-10 dynes/cm^2.

3.2.2 Dissociation of Small Cell Clusters

We first introduced cell suspensions into the device to determine whether cells are lost under different operating conditions due to holdup or damage induced by shearing. We employed HCT 116 colon cancer cells that were grown in culture flasks, digested with trypsin-EDTA, and mechanically sheared (pipetting and vortexing) per routine procedures. Cell suspensions were applied to the microfluidic device using a syringe pump under different flow rate and cell concentration conditions. Cell recovery was then assessed using a commercial cell counter, and compared to the initial value measured before passing through the device. We found that recovered cell counts increased progressively with flow rate, ranging from approximately 40% of the initial count at 0.2 mL/min to approximately 100% at 12.5 mL/min (Figure 3.2A). In fact, recovery was slightly greater than 100% and we observed a shift in the population to smaller sizes (Figure 3.2B). We believe that the larger species correspond to small clusters of 2 or more cells that remained after trypsin digestion and vortexing/pipetting treatments. This is a common occurrence in routine cell culture, but additional treatment is not encouraged because it could decrease cell viability and the small clusters do not negatively affect sub-culturing or most downstream assays.

The device was significantly more effective at dissociating these small cell clusters, resulting in a truer single cell suspension. Evidence supporting our conclusion can be found in the fact that the device yielded a cell population that was evenly distributed around an average diameter of 13-14 μm, which was consistent with microscopic analysis of HCT 116 cells (Figure 3.2B). Control samples had a similar peak size, but also showed significant species at larger sizes. We defined single cells by gating the histograms equally around the 13.5 μm mean, from 9.5 μm to 17.5 μm. Using this size range to define single cells, we found that only 75% of the events were single cells prior to device treatment. Single cell percentage increased with flow rate up to 94% at 12.5 mL/min (Figure 3.2C). We believe the clusters were dissociated rather than simply retained in the device, as the latter case would have lowered total recovery yield for the 12.5 mL/min sample. However, since recovery at this condition did not significantly exceed 100%, increases in cell number from cluster dissociation were likely offset by losses that could have been incurred from device holdup, including non-specific sticking or entrapment in low flow regions, or cell destruction. Recovery results did decrease slightly for lower input cell concentrations, but remained greater than 90% even when only 10,000 cells were tested (Figure 3.2D). Finally, we employed a different cell type, LS 174T colon cancer cells. Cell suspensions contained 79% single cells prior to device treatment, and this was enhanced to 92%, with a similar total cell count, after processing at 12.5 mL/min (Figure 3.2E). Representative cell histograms and micrographs are shown in Figure 3.2F. Note that it is possible that single cell percentage is over-represented in control samples because clusters larger than 30 μm, such as those pictured in the micrograph, were not assessed by the cell counter. From these studies, it is clear that the microfluidic dissociation device can significantly improve single

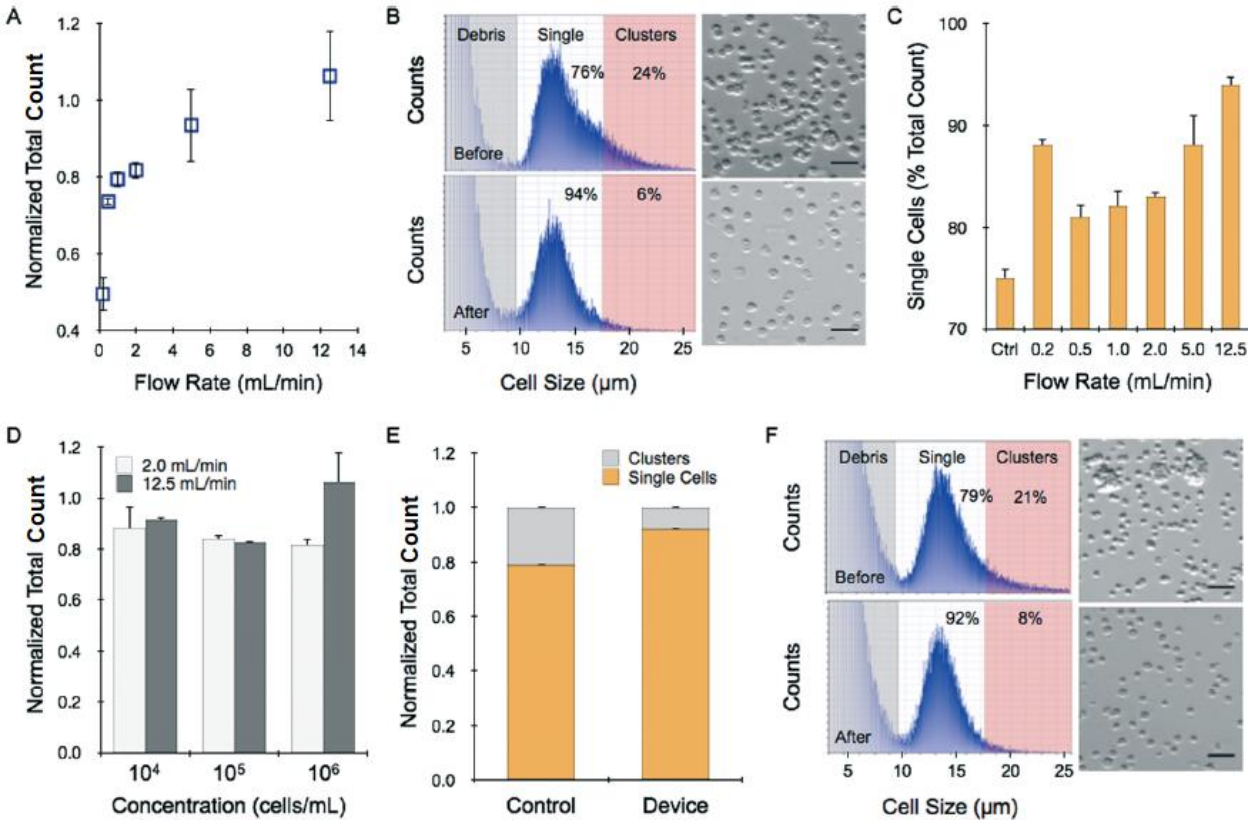

Figure 3.2. Dissociation of small clusters in cell suspensions. (A-D) Cultured HCT 116 colon cancer cells were treated with trypsin-EDTA and the cell suspensions were passed through the microfluidic device. (A) Increasing flow rate led to progressively higher cell counts in the recovered sample, reaching approximately the same value as before addition to the device. (B) While total count was similar, the size distribution before (top) and after treatment at 12.5 mL/min (bottom) changed significantly. The peak size was approximately 13.5 μm for both cases, however prior to device treatment there was also a population of larger sizes corresponding to cell clusters. The device-processed sample was evenly distributed around the mean, indicating that nearly all events were single cells. The accompanying micrographs confirm average cell size and single cell content. (C) The percentage of single cells was determined as the counts between 9.5 to 17.5 μm compared to the total count. In general, increasing flow rate resulted in more efficient dissociation of cell clusters. (D) Total recovery was similar at lower initial concentrations, down to only 10,000 cells. (E) Single cell and total counts obtained for LS 174T colon cancer cell suspensions prior to and after passing through the microfluidic device at 12.5 mL/min. Total recovery was again similar, with a greater percentage of single cells due to dissociation of cell clusters. (F) Population size distribution shifted to lower values after device treatment, indicating higher single cell content. All total count results obtained after device treatment were normalized to the value before treatment. Scale bars represent 50 μm. Error represent the standard error from at least three independent experiments.

cell content in trypsin-treated cell cultures. Moreover, results were consistent and robust for low sample concentrations and for different cell lines.

3.2.3 Dissociation of Intact Cell Monolayers

While dissociating small cell clusters is promising, our goal is to process tumor tissues. As a starting point, we created a simple tissue model consisting of cell monolayers that were released as intact sheets. This was accomplished by growing HCT 116 cells to confluency in collagen-coated wells and then treating with collagenase. These monolayer tumor sheets contained approximately 1 million cells that indeed remained connected to each other after being suspended. Dissociation experiments were conducted by passing a single tumor sheet through the device in buffer at 2 and 12.5 mL/min flow rates. To increase dissociation efficiency, some samples were repositioned for multiple device passes. After testing was complete, the sample was recovered and a cell count was obtained. Finally, we tested whether large aggregates passed through the device by treating the effluent with trypsin-EDTA, vortexing, pipetting, and performing a second cell count. Control sheets only received trypsin-EDTA, vortexing, and pipetting procedures, and less than 60% of the cell counter events were single cells. At 2 mL/min operating flow rate, total recovery including contributions from single cells, small clusters, and large aggregates was only 60% of the control count (Figure 3.3A). Utilizing more device passes progressively increased singe cell yield, but total recovery was similar suggesting that significant sample remained within the device or samples were damaged. Increasing flow rate to 12.5 mL/min improved results substantially (Figure 3.3B). Total recoveries after 1 and 3 passes were both nearly the same as the control, with single cell yield increasing upon further treatment. However, after 10 passes the total count exceeded the control by

30%. This was possible because the sample now contained 95% single cells with no appreciable large aggregates (Figures 3.3B and C). Note that these promising results were obtained with no additional treatment, only the hydrodynamic forces generated within the microfluidic device following release of the intact monolayers using collagenase.

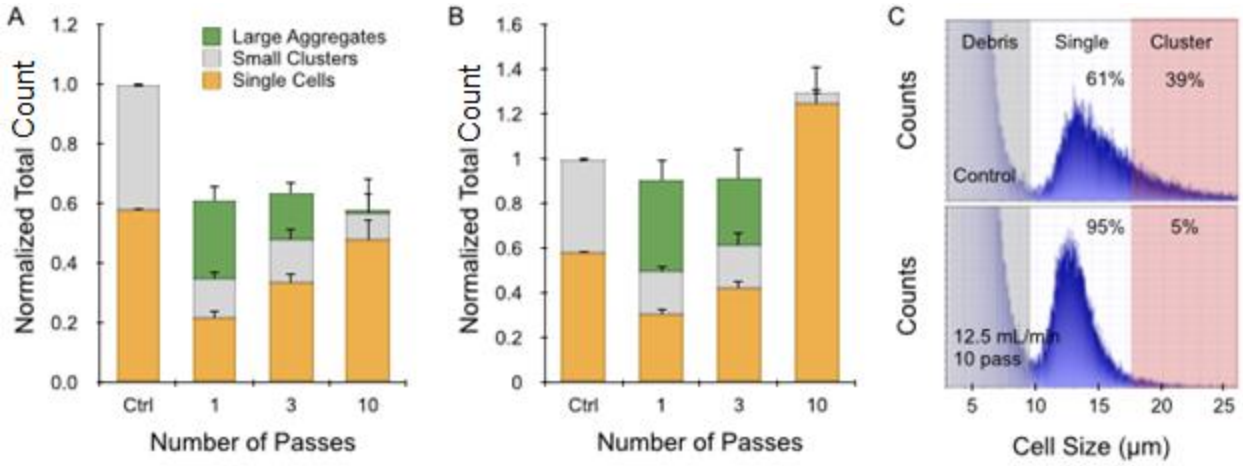

Figure 3.3. Dissociation of tumor monolayer sheets. HCT 116 cells were grown to confluency in collagen-coated 24-well plates and released as intact monolayer sheets using collagenase. Sheets were then passed directly through the microfluidic dissociation device at different flow rates for a total of 1, 3, or 10 passes. Control sheets were treated with trypsin-EDTA, vortexed, and pipetted. (A) At 2 mL/min flow rate, total count was only 60% of the trypsin control after as single device pass. Additional passes did not change total recovery, but did increase single cells at the expense of large aggregates. (B) Increasing flow rate to 12.5 mL/min enhanced total recovery to values similar to the trypsin-control for 1 and 3 passes. After 10 passes, total recovery exceeded the trypsin control by 30%, and single cell accounted for 95% of the recovered sample. (C) Representative cell counter histograms for the (top) trypsin control and (bottom) 12.5 mL/min, 10 pass cases. All total count results were normalized to controls that were digested with trypsin. Error represent the standard error from at least three independent experiments.

3.2.4 Dissociation of Tumor Spheroids

Next we employed tumor spheroids, a more advanced model with three-dimensional structure that more closely resembles solid tumors. Spheroids were prepared using the hanging drop method and collected after reaching 250-300 μm diameter. We employed HCT 116 and LS 174T cells as already discussed, as well as NCI-H1650 lung

cancer cells. In each case, the spheroids contained approximately 1000 cells. Dissociation experiments were conducted in a similar manner to the tumor sheet studies. Results obtained for 12 pooled HCT 116 spheroids that were processed at 12.5 mL/min flow rate for different number of device passes are presented in Figure 4A. Overall, recovery results were strikingly similar to the HCT 116 tumor sheets processed at 2 mL/min flow rate (Figure 3.3A). Total count was approximately 60% of the control after 1 pass, but actually decreased with additional treatment, possibly indicating cell damage. Single cell content did increase progressively, nearly approaching the value present within the control. We also performed 10 pass experiments with different numbers of HCT 116 spheroids, and found recovery results that scaled directly with sample size (Figure 3.4B). Remarkably, this includes using only a single spheroid that initially contained only 1000 cells. Finally, we performed dissociation tests with NCI-H1650 (Figure 3.4C) and LS 174T (Figure 3.4D) spheroids, and observed recovery results that were similar to the HCT 116 case but with even lower yields. This is likely due to the fact that these spheroids are more cohesive, as they do require longer digestion times with trypsin. These data suggest that the device was not able to generate high enough shear forces to dissociate tumor spheroids without inducing cell damage. Improving recovery results through additional device passes does not appear to offer much potential, and we were already operating at the highest flow rate of our syringe pump.

Although device dissociation of tumor spheroids was inefficient, this would be an unnecessarily stringent goal for practical purposes, as tumor tissues are typically treated with proteolytic enzymes prior to mechanical treatments. Therefore we tested device performance after brief exposure of spheroids to trypsin-EDTA. We also tested brief EDTA

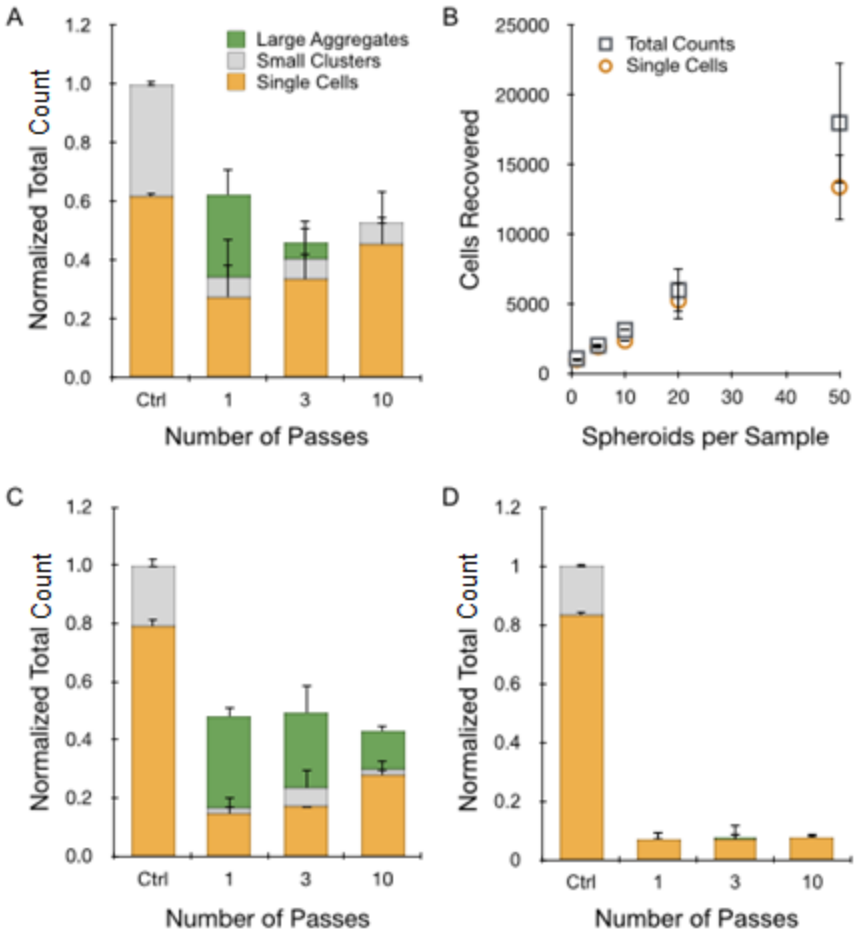

Figure 3.4. Dissociation of tumor spheroids. Tumor spheroids were grown with different cell lines using the hanging drop method and passed directly through the microfluidic dissociation device at 12.5 mL/min for a total of 1, 3, or 10 passes. Control spheroids were treated with trypsin-EDTA, vortexed, and pipetted. (A) For HCT 116 spheroids, total recovery was only 60% of the control after a single pass. Additional device passes decreased total recovery, but did shift the population to higher single cell percentages that were similar to the control. (B) Total and single cell recoveries scaled with initial spheroid concentration, even down to a single spheroid. Results for (C) NCI-H1650 lung cancer and (D) LS 174T spheroids were similar, but with lower total recoveries even after 10 passes. All total count results were normalized to the maximum count determined by fully digesting each spheroid type with trypsin. Error represent the standard error from at least three independent experiments.

treatment to explore an enzyme-free alternative. After 5 min trypsin digestion, total recovery for of HCT 116 spheroids improved 2.75-fold after a single pass, with negative effects observed for additional processing (Figure 3.5A). Single cell content only increased from 75 to 85% (Figure 3.5D), and thus the dramatic increase in total count is likely to have

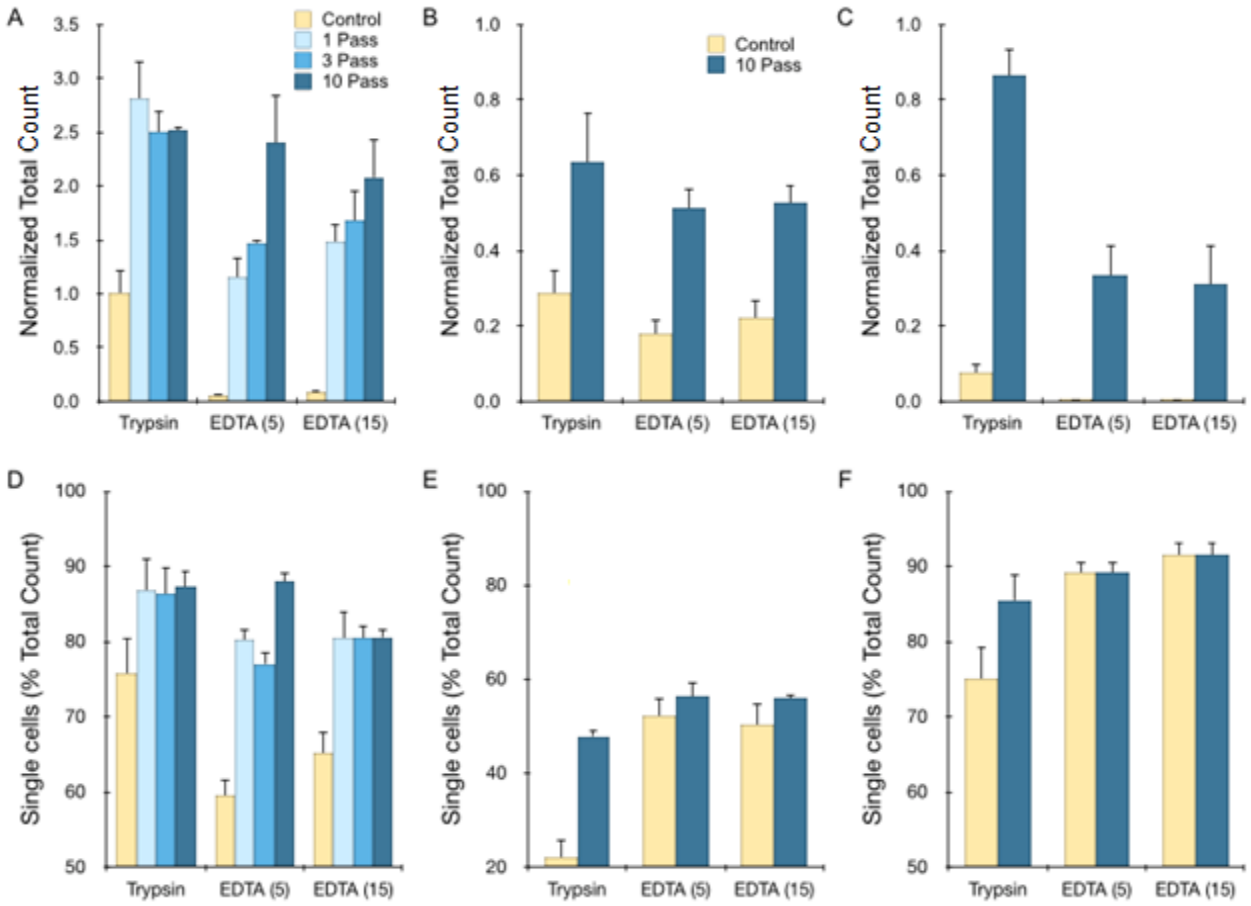

Figure 3.5. Microfluidic dissociation augments trypsin and EDTA treatments. Total recovery (A-C) and single cell percentage (D-F) for different spheroid types following treatment with trypsin for 5 min, EDTA for 5 min, or EDTA for 15 min, with or without microfluidic device processing at 12.5 mL/min. (A,D) For HCT 116 spheroids, the device increased total recovery for both treatments by 2- to 3-fold, with improved single cell content as well. Maximal results were obtained after 1 pass for the trypsin case, while additional passes enhanced EDTA results. (B,E) For NCI-H1650 spheroids, samples were only partially dissociated for brief trypsin and EDTA treatments, but 10 passes through the microfluidic device improved total recovery by more than 2-fold. (C,F) For LS 174T spheroids, brief trypsin and EDTA treatments were extremely inefficient, but were enhanced by more than 10-fold following microfluidic device processing (10 passes). All total count results were normalized to the maximum count determined by fully digesting each spheroid type with trypsin. Error represent the standard error from at least three independent experiments.

arisen from enhanced dissociation of larger aggregates that were not measured by the cell counter. EDTA treatment was extremely inefficient, but the microfluidic device increased recovery dramatically. Total yield was similar to the trypsin control following a single pass,

and increased almost 2.5-fold with further processing. Increasing EDTA exposure time enhanced recovery for all but the 10-pass case. NCI-H1650 and LS 174T spheroids required at least 20 min for complete trypsin dissociation, and after 5 min total recoveries were only 30% for NCI-H1650 and 8% for LS 174T cases. The microfluidic device improved recovery by 2- and 10-fold, respectively (Figures 3.5B and C). Combined EDTA-device treatments had lower total recoveries, but still exceeded the short trypsin treatment. In all cases, the microfluidic device improved single cell content (Figures 3.5D-F). Representative cell counter histograms for all conditions are shown in the Supplemental Information. Based on these findings, microfluidic dissociation significantly augments enzymatic digestion, resulting in enhanced single and total cell yields. Notably, comparable recoveries were obtained using the enzyme-free combination of EDTA and device treatments, which could be beneficial for preserving key surface proteins. As a final note, EDTA may also serve as an anticoagulant for clinical specimens, which can be contaminated with blood from procurement procedures [16].

3.2.5 Analysis of Cell Suspensions by Flow Cytometry

We further characterized the cell suspensions achieved from the different dissociation procedures using flow cytometry. First, we utilized light scattering information to confirm our conclusions regarding single cell content. This was done by plotting the forward-scatter width (FSC-W) versus the forward-scatter area (FSC-A). These values are directly related for single cells, uniformly aligning data points along a constant axis. Representative results for HCT 116 spheroids treated with trypsin, trypsin followed by device processing (12.5 mL/min, 10 passes), and EDTA followed by device processing are

shown in Figure 3.6A. Note the data points located within the gated rectangle region are the expected single cells. Non-symmetric components such as doublets and larger order clusters have a relatively larger FSC-A, shifting data points to the right of the plot. Single cell percentages were calculated based on the number of events inside the gated region relative to total events, and values are shown in Figure 3.6B. These closely match cell counter results shown in Figures 3.5D-F. The uniform population shift observed for the EDTA/device condition could be indicative of cell distress.

Finally, we measured the expression of specific surface protein biomarkers to assess the impact of the different dissociation procedures. Diagnostic and cell sorting applications require specific targets to provide information or select for unique cell subpopulations. Surface proteins are typically employed because they are easier to access for live cells, but this also increases the likelihood that these protein targets are damaged. We selected classic tumor biomarkers for this study, including epithelial cell adhesion molecule (EpCAM), transferrin receptor (TfR), and mucin 1 (MUC1). We have previously observed that TfR and MUC1 are cleaved by trypsin, leading to lower expression levels. EpCAM is not sensitive to trypsin, but is a homotypic cell-cell junction protein that could be affected by mechanical separation. We found that EpCAM expression on cells obtained from HCT 116 and NCI-H1650 spheroids was similar for all dissociation treatments, including when the device was used exclusively for dissociation (Figures 3.6C and D). Brief exposure to trypsin did lower expression of TfR and MUC1 expression relative to EDTA treatment, by approximately 25 to 50%. Differences were more pronounced after longer trypsin digestion times. Device treatment at 12.5 mL/min flow rate for 10 passes did not significantly alter trypsin or EDTA results. Slightly elevated expression of TfR and MUC1

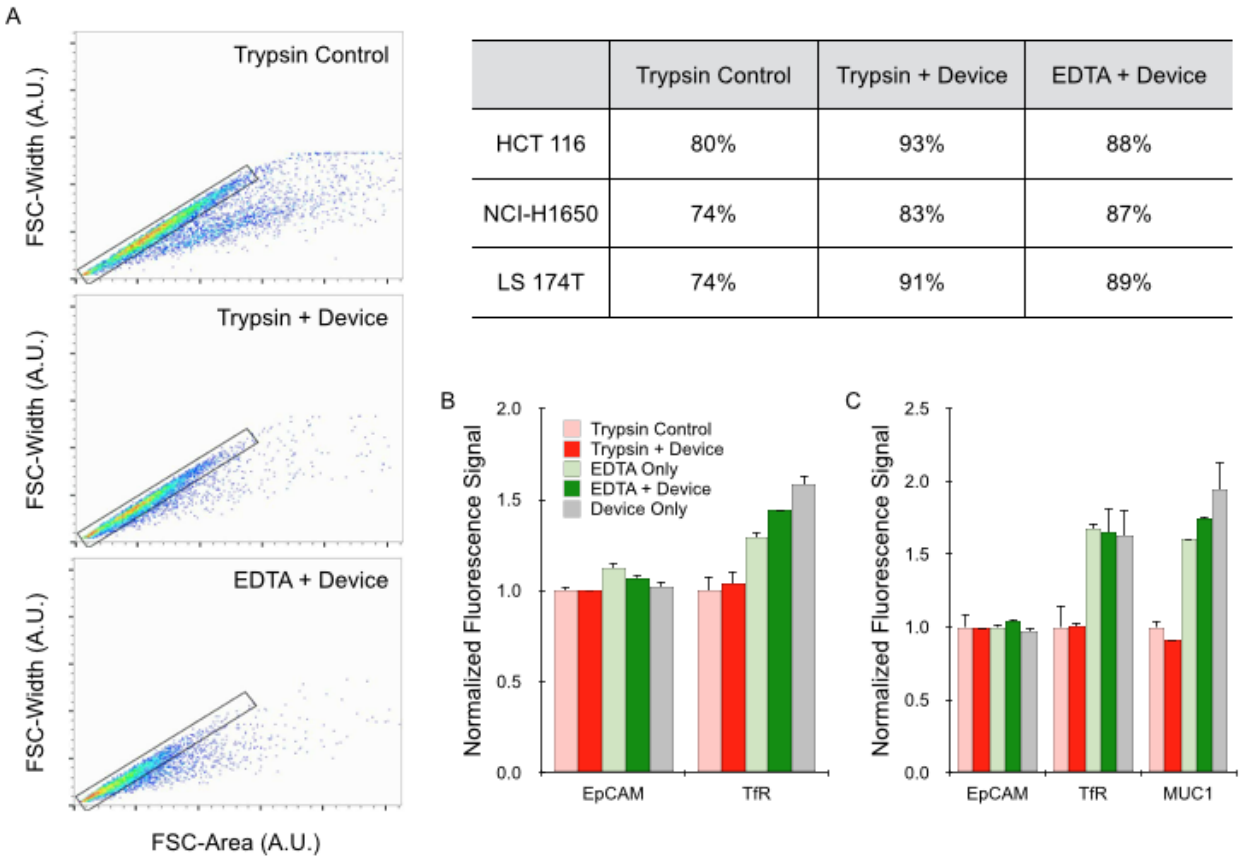

	Trypsin Control	Trypsin + Device	EDTA + Device
HCT 116	80%	93%	88%
NCI-H1650	74%	83%	87%
LS 174T	74%	91%	89%

Figure 3.6. Single cell content and molecular expression determined by flow cytometry. (A) Single cells and aggregates were identified by plotting the forward scatter (FSC)-width by FSC-area for HCT 116 spheroids under different dissociation conditions. Single cells fall within the gated region, while aggregates are shifted to the right. The percentage of events inside the gate relative to the total population are given in the table for HCT 116, NCI-H1650, and LS 174T cases. (B) HCT 116 spheroids were stained for the surface biomarkers EpCAM and TfR. EpCAM is a homotypic cell adhesion molecules, and expression was similar under all dissociation conditions. TfR is sensitive to trypsin cleavage, resulting in lower expression. Device treatment did not alter expression either case. (C) Similar results were observed for NCI-H1650 spheroids. MUC1 expression was also measured, and showed trypsin sensitivity. All fluorescent signals were normalized to controls that were digested with trypsin. Error represent the standard error from at least three independent experiments.

was observed when the device was used alone, but only in some cases. This may indicate that membrane integrity may have been compromised to some degree by hydrodynamic shear forces, leading to labeling of intracellular stores of the targets. Note that HCT 116 cells do not express appreciable levels of MUC1. These findings confirm the potential power

that non-enzymatic dissociation methods, such as our device working alone or in concert with EDTA, can have for preserving surface biomarker expression.

3.3 Materials and Methods

3.3.1 Device Fabrication

The dissociation device was produced using a commercial microfabrication process offered by ALine, Inc. (Rancho Dominguez, CA). This is a laminate technology that uses a laser to cut the desired pattern in hard PET plastic sheets. Multiple PET layers are then aligned and fused using adhesive and pressure lamination. The channel features were designed in AutoCAD and arranged over three plastic layers (Figure 3.1B). The device was sealed using two additional uncut sections, for a total of seven layers. Channels are connected between layers by *vias* to facilitate fluid flow. Holes were drilled and hose barbs were installed to serve as the fluid inlet and outlet. The bottom layer was a 125 μm thick solid slab of PET.

3.3.2 Fluid Dynamic Simulations

To characterize flow profiles and shear stresses within the device, particularly the channel constrictions where dissociation is primarily expected to occur, we performed finite-element fluid dynamics simulations using COMSOL Multiphysics software. Simulations were conducted by coupling the Navier-Stokes equations and continuity equation, assuming laminar flow and applying the no-slip condition at the channel walls. Fluid density and viscosity were assumed to be that of water. Simulations were performed for a single channel within each stage because full device calculations were complex and the laminate format causes the fluid to change directions as it passes between stages.

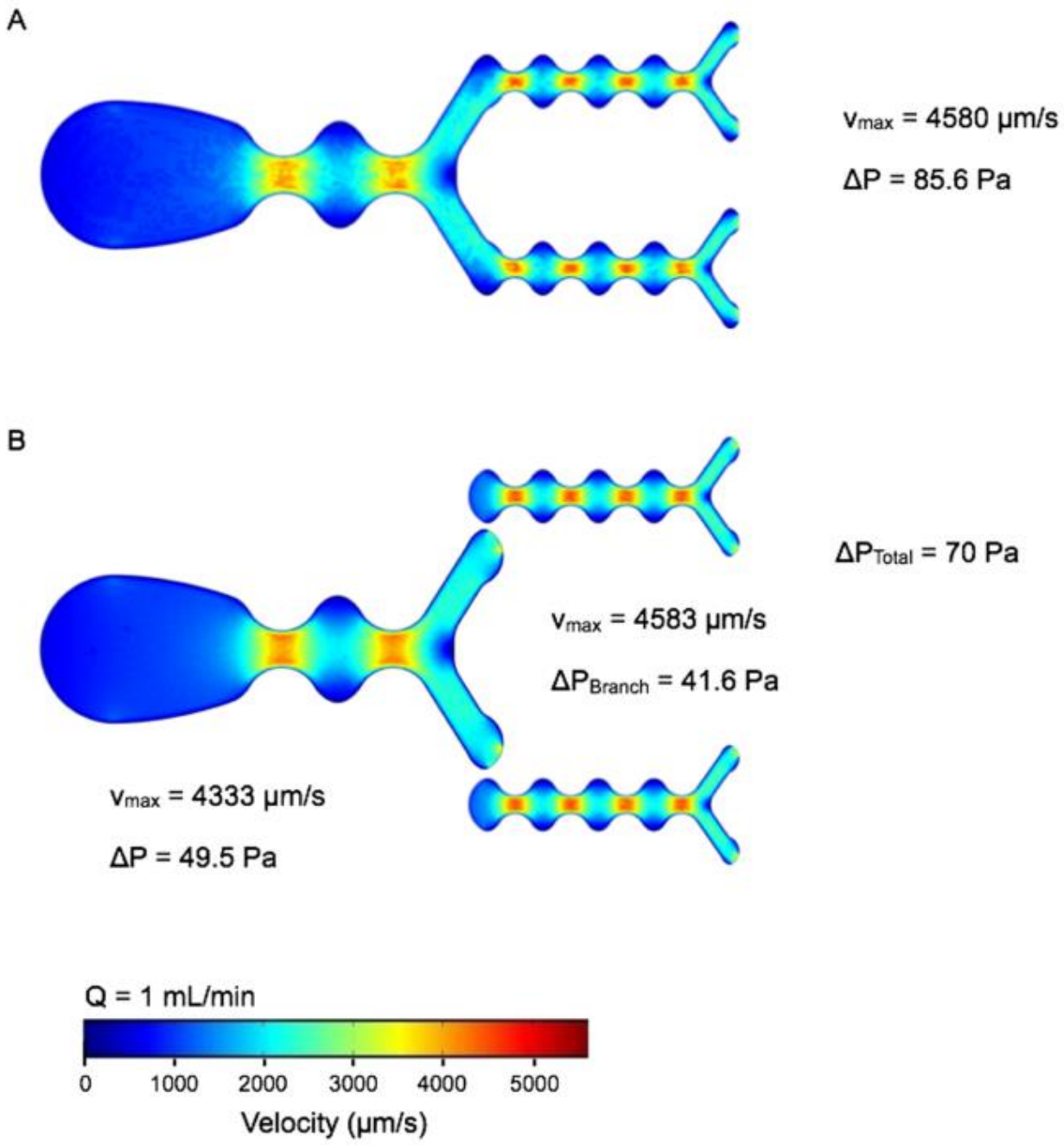

Figure 3.7. Finite-element fluid dynamics simulations of single and consecutive stages. Simulations were performed at 1 mL/min flow rate for the first and second device stages (A) with direct connection between the stages or (B) as separate units. Inlet conditions for stage 2 in part B are based on the average velocity. Velocity profiles appear similar, and the maximum velocity values are identical. Separating the stages does however lead to underestimating the total pressure drop by 15%.

Channel specifications were imported from the AutoCAD files used for device fabrication, and included the inlet, all expansions and constrictions, and the branch point (Figure 3.1B). Channel dimensions are given in Table 3.1. For the inlet condition, we used the average velocity (v_{avg}), which is the same for all channels throughout the device because both channel height and total width across all channels within each stage are constants. Outlet pressure was assumed to be zero to determine the pressure drop (ΔP). Flow profiles are shown in Figure 1C for a flow rate of 1 mL/min, with maximum velocity (v_{max}) and pressure drop values given in Table 1. Total pressure drop (ΔP_{Total}) for the device was calculated by summing the channel pressure drops in parallel to determine the total value for the stage, and summing the results for each stage in series. Results for different flow rate conditions will scale proportionally (data not shown). Simulation outputs that included the first and second stages in sequence were similar to that of the individual channels (Figure 3.7).

3.3.3 Cell Culture and Tissue Models

Human colon cancer cell lines HCT 116 and LS 174T, and lung cancer cell line NCI-H1650, were obtained from ATCC (Manassas, VA). Cells were cultured in standard tissue culture flasks using DMEM media containing 10% FBS and 1% penicillin-streptomycin, and passaged using trypsin-EDTA (Corning, Corning, NY). Cell suspensions used for device testing were obtained in similar manner to the passaging procedures. Monolayer tumor sheets were prepared by growing HCT 116 cells in collagen-coated 24-well plates (Life Technologies, Carlsbad, CA) to confluency, washing with Hanks Buffered Saline Solution

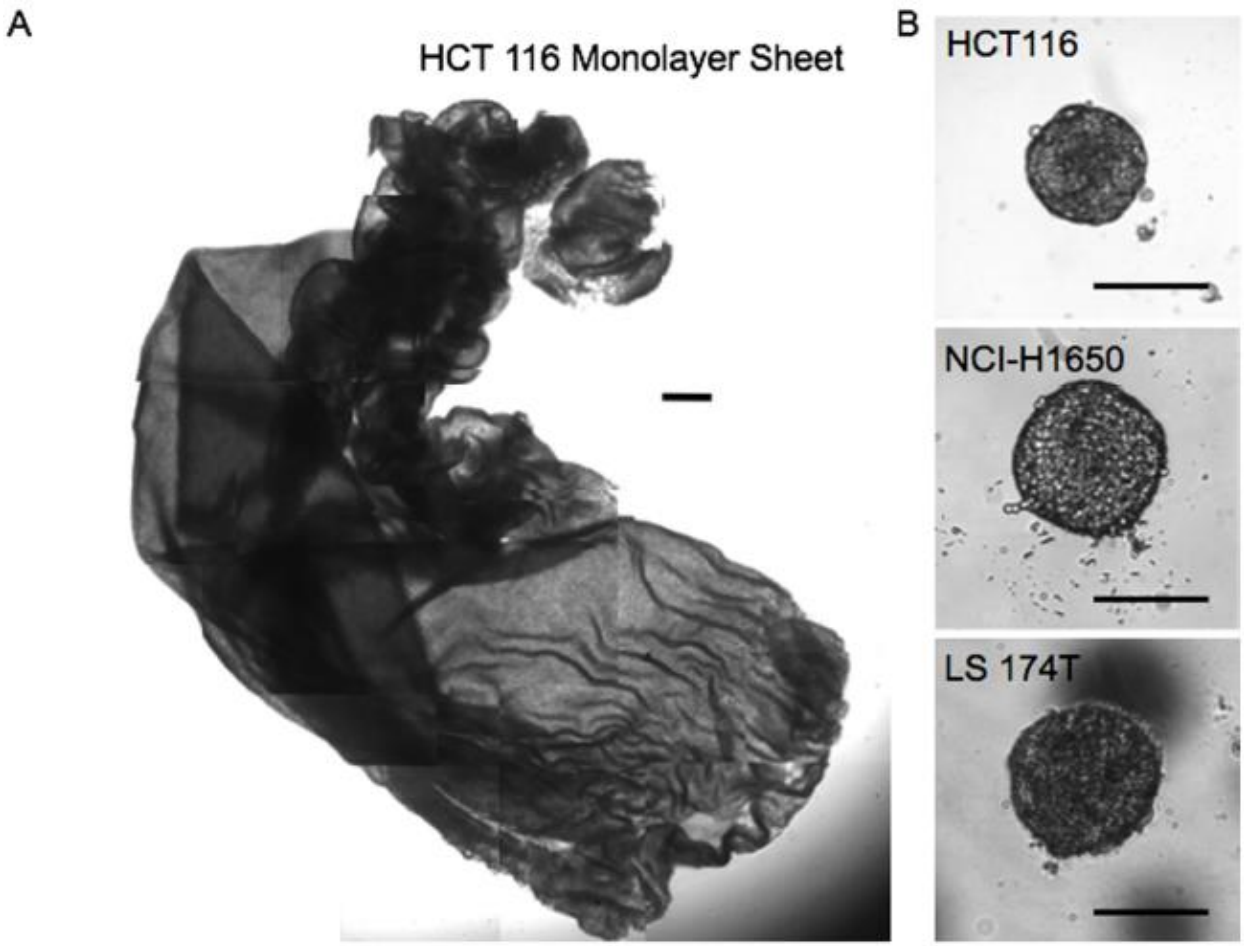

Figure 3.8. Tumor monolayer sheet and spheroid models. (A) Tumor monolayer sheet created by growing HCT 116 cells in collagen-coated 24-well plates and releasing with collagenase. Image was manually tiled together from many individual micrographs. (B) Tumor spheroids produced using the hanging drop method for HCT 116, NCI-H1650, and LS 174T cells. Scale bars represent 250 μm.

(Corning, Corning, NY), incubating with Type II collagenase (Life Technologies, Carlsbad, CA) for 5 min, and releasing the intact monolayer by agitation. Tumor spheroids were grown in MicroWell MiniTrays (Thermo Fisher Scientific, Waltham, MA) using the hanging drop method [55]. Briefly, 20 μL of media containing approximately 300 cells was added to each well, the plate was inverted, and the cells were cultured in the meniscus formed at the air-liquid interface until cohesive spheroids formed and reached approximately 300 μm diameter. Micrographs of tissue models are shown in Figure 3.8. Individual spheroids were

recovered using a P-200 pipette, and pooled for experiments. For spheroids that received pre-treatment with trypsin-EDTA or EDTA (Cellstripper, Corning, Corning, NY), the sample was centrifuged, resuspended in the treatment, and incubated for the indicated time period. All samples (cell suspensions, tumor monolayer sheets, and tumor spheroids with or without pre-treatment) were prepared for experiments by centrifugation and resuspension in 1 mL PBS containing 1% BSA (PBS+). Control samples were only treated with trypsin-EDTA or EDTA, followed by vortexing and repeated pipetting.

3.3.4 Dissociation Studies

The dissociation device was prepared by affixing 3" PVC 1/32ID tubing (Nalgene, Rochester, NY) to the hose barbs at both the inlet and the outlet. A 3-way valve was added to the inlet tubing, with connections to a syringe pump (Harvard Apparatus, Holliston, MA) and a buffer reservoir. Prior to use, devices were filled with Superblock blocking buffer (Thermo Fisher Scientific, Waltham, MA) and incubated for 15 minutes to prevent non-specific adhesion of cells to the channel walls, and then flushed with PBS+. Cell or tumor tissue samples were loaded into a syringe, and administered to the device using a syringe pump with flow rate set between 0.2 to 12.5 mL/min. The latter flow rate was the maximum we could generate with our syringe pump, and required only 5 s to run the 1 mL sample. For single pass studies, the sample was collected and the device was flushed at the same flow rate with 1 mL PBS+ that was obtained via the buffer reservoir at the inlet. Sample and wash effluents were combined prior to analysis. For multiple pass experiments, flow was reversed at 2 mL/min to withdraw the sample back into the syringe in preparation for the next run. This process was repeated for the indicated number of passes,

and afterward the sample was collected and device flushed as described above. Cell concentration was measured using a Moxi Z cell counter with type S cassettes (Orflo, Hailey, ID), which utilizes the Coulter principle. The cassettes contain a prefilter to remove large cell aggregates and the device only measures cell sizes up to 26 μm diameter, thus only single cells and small aggregates are counted. To determine if large aggregates were present in the samples, the entire volume was centrifuged, resuspended in trypsin-EDTA, incubated for 5 min, vortexed, pipetted repeatedly, and a second cell count was obtained. The difference in the two cell counts was attributed to large aggregates. Counts corresponding to single cells were defined by first identifying the peak size in the cell counter histograms, and then applying an equal distribution to both smaller and larger sizes. Mean cell diameters were approximately 13 μm for cell suspensions and monolayer sheets and 17 μm for spheroids. Sizes were corroborated by visual inspection of samples using a microscope. Total recoveries for all experimental conditions were normalized to the control sample that was treated only with trypsin-EDTA. Single cells were represented as the percentage of counts that fell within the single cell size range relative to the total count. Data are represented as the mean +/- standard error determined from at least three independent experiments.

3.3.5 Flow Cytometry

Dissociated spheroid samples were labeled with monoclonal antibodies specific to human EpCAM (mouse IgG_{2B}, clone 158206, R&D Systems, Minneapolis, MN), transferrin receptor (TfR, mouse IgG_1, clone 29806, R&D Systems, Minneapolis, MN), or mucin 1 (MUC1, mouse IgG_1, clone M01102909, Fitzgerald Industries International, Acton, MA). A

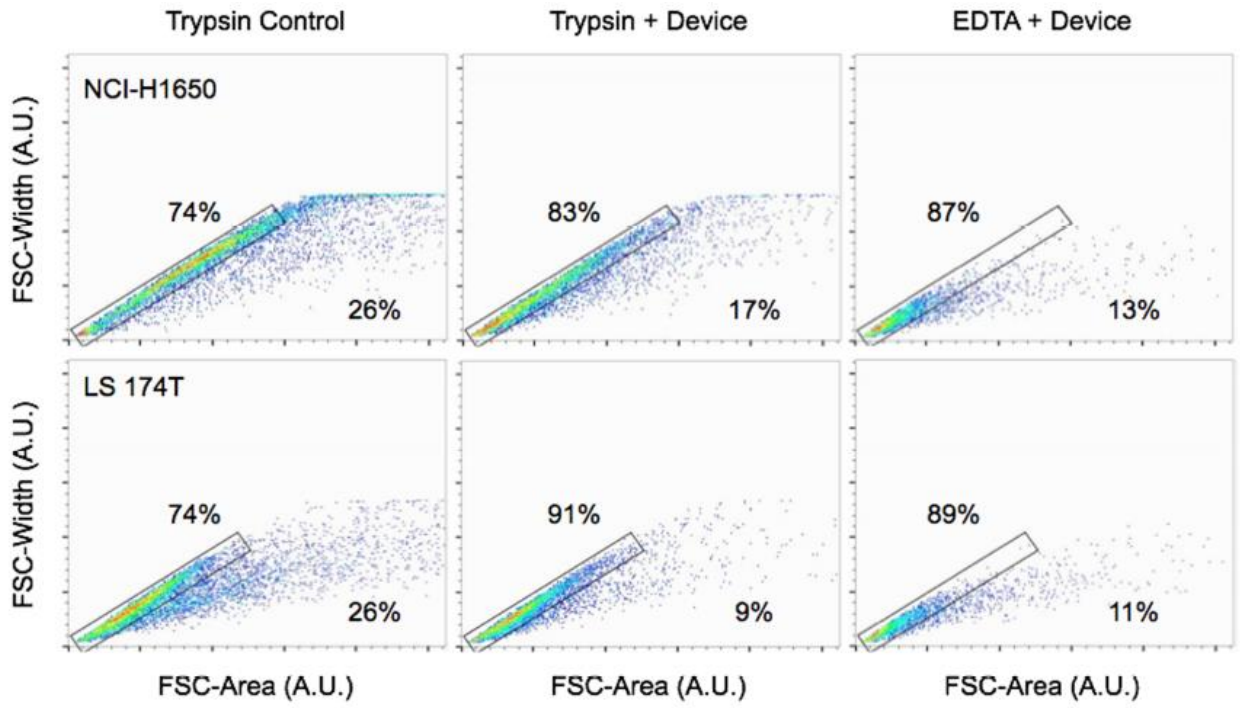

Figure 3.9. Flow cytometry analysis of single cells and aggregates obtained from tumor spheroids. Single cells are identified following dissociation of NCI-H1650 and LS 174T spheroids by plotting forward scatter (FSC)-width versus FSC-area. Single cells are shown in the boxed region, with the larger and non-symmetric aggregates outside.

non-binding monoclonal antibody (rat anti-mouse IgG1, clone A85-1, BD Biosciences, San Jose, CA) was used as a control. Cell suspensions were centrifuged, resuspended in PBS+ containing 5 µg/mL primary antibody, and incubated for 30 min at room temperature. Samples were then washed twice with ice-cold PBS+ by centrifugation, resuspended in ice-cold PBS+ containing 2 µg/mL fluorescein-conjugated secondary antibody (rat anti-mouse IgG1, clone A85-1, or anti-mouse IgG2a/2b, clone R2-40, BD Biosciences, San Jose, CA), incubated for 30 min on ice, washed twice with PBS+, and resuspended in 0.25 mL PBS+. Cell scattering and fluorescein signal intensities were acquired using an LSR II flow cytometer (Becton Dickenson, Franklin Lakes, NJ), and analyzed using FlowJo software (Tree Star, Ashland, OR). Single cells were discriminated from aggregates by plotting

forward-scattering width (FSC-W) versus forward-scattering area (FSC-A). Single cells fall on a line of constant slope, and were gated. Aggregates have higher FSC-A, shifting data points away from the single cell region. Single cells were represented as the percentage of data points that fell within the gated region relative to the total population (Figure 3.9). Fluorescein intensity values are based on the geometric mean measured for single cells, after subtracting background signals obtained with the control antibody. All signals were normalized to the control sample that was treated only with trypsin-EDTA. Data are represented as the mean +/- standard error determined from at least three independent experiments.

3.4 Conclusion

In this chapter, we present a novel microfluidic device for dissociating tumor tissue into single cells. This device utilizes a branching channel network and repeated constrictions to generate well-defined and multi-scaled fluid shear force challenges, acting as "hydrodynamic micro-scalpels", to dissociate tumor tissue and cell aggregates. We demonstrated using tumor cell culture models of varying complexity that our microfluidic dissociation device produces significantly higher total cell numbers, with a greater percentage of single cells, when compared to routine trypsin digestion, vortexing, and pipetting treatments. For small clusters in cell suspensions and intact monolayer sheets, superior results were obtained using the device alone. For more complex tumor spheroids, the device dramatically augmented trypsin and EDTA treatments. The combination of brief EDTA exposure followed by device processing is particularly interesting as a non-enzymatic method, resulting in higher cell recovery without affecting surface protein

expression. This could significantly improve results for applications that rely on protease sensitive surface markers, such as molecular diagnostics or studies seeking to detect and isolate cancer stem cells via CD44 or other potential targets [23]–[26].

We have identified four tissue dissociation criteria that would dramatically expand the application of single cell-based methods for solid tumor specimens: (1) recovery yield, (2) cell quality, (3) processing speed, and (4) automation. We have shown evidence here that the microfluidic dissociation device holds excellent potential for improving the recovery of single cells. We are currently pursuing ways to improve this initial prototype, investigating different channel dimensions and features to increase dissociation efficiency. This would improve overall capabilities and enable comparable results to be achieved at lower flow rates that may be more compatible with specific downstream applications. We are also evaluating new designs to minimize sample holdup and clogging. With regard to cell quality, the microfluidic device may allow non-enzymatic procedures or significantly decrease proteolytic digestion times, thereby better preserving expression of certain surface proteins. Follow up work is planned to investigate effects on cell viability. For processing speed, the high flow rates that were required to achieve efficient dissociation required only five seconds per pass for the 1 mL sample volumes. We should note that this is a reasonable processing rate to allow for manual flow actuation with a standard P-1000 laboratory pipetter. Factoring in time to reposition the sample between runs, multiple pass experiments required less than two minutes. Even studies incorporating brief trypsin or EDTA incubations prior to device treatment were performed in less than ten minutes total processing time. Finally, automating dissociation procedures would standardize results, eliminate infrastructure needs, and enable point-of-care operation. We envision that our

microfluidic dissociation device could serve as the first component of an integrated and automated platform. This would be accomplished by directly interfacing modules to enable filtering, microfluidic operations such as cell sorting/purification or physical characterization, and miniaturized detectors for molecular analysis.

Considering future application to human clinical tumor specimens, these tissues may be substantially more complex than the cell culture models that we have employed in this chapter. Our model tissues only contained a single cancer cell type, did not have physiological structures such as blood vessels, and most likely had lower stromal content. Furthermore, sample dimensions were either centimeter scale monolayers or spheroids that were hundreds of microns in diameter. Human tumor tissue specimens obtained by resection, surgical biopsy, or core needle biopsy will be composed of heterogeneous cell populations held together by significant stroma. These specimens can also be very large, but typically are minced with a scalpel into 1-2 mm pieces prior to enzymatic digestion. Future studies will seek to evaluate device performance using these types of samples, either obtained from xenograft tumor models or human specimens. While human specimens may be substantially more complex, a key observation from this work is that as samples became more complex, a smaller percentage of the sample obtained after trypsin digestion was single cells, and thus there was a corresponding increase in the potential impact of the microfluidic device. Thus, we predict that complex samples are more likely to need additional treatment from the device to effectively liberate single cells. Microfluidic dissociation can also reduce incubation times or enable use of gentler alternatives. As discussed, EDTA can serve a dual role to prevent blood coagulant and induce tissue dissociation with clinical specimens, and thus can be considered a baseline treatment.

Finally, we believe our device approach is particularly well-suited for small volume clinical specimens such as FNA biopsies that we have worked with previously [16]. The FNA technique uses smaller 22 gauge needles (~400 μm orifice) to withdraw small tissue fragments and individual cells. This makes FNAs less invasive, minimizing patient morbidity while also increasing potential for repeated sampling in both spatial and temporal (i.e. before and after drug treatment) contexts [56], [57]. However, FNA samples are difficult to work with for diagnostic applications because yields are very low, potentially on the order of only 10,000 cells [16], [58]–[60]. It is possible that the simple tissue models we have used in this chapter may realistically reflect the small tissue fragments and cell aggregates that are characteristic of FNA specimens. We have already shown that the microfluidic device can operate with small sample sizes (10,000 cells or single spheroids).

CHAPTER 4 MICROFLUIDIC CHANNEL OPTIMIZATIONS

4.1 Introduction

Recent insights into the importance of cellular heterogeneity have combined with advancements in sequencing technologies to help usher in the era of single cell diagnostics [33], [34]. But progress towards clinical applications will be limited by the fact that most cells in the body reside within tissue masses and organs. For example, the most common and deadly forms of cancer originate from epithelial tissues, resulting in abnormal tissue masses that are highly cohesive and difficult to break down [61]–[63]. Overcoming this obstacle would provide valuable insight about resident tumor and host subpopulations that could help predict disease progression, metastatic potential, and drug resistance [37], [61], [64]–[66]. Current tissue dissociation procedures involve cutting tissues into small pieces with a scalpel, lengthy digestion with proteolytic enzymes, and mechanical treatment by pipetting and vortexing. This is a laborious, time-consuming, and inefficient process that results in significant loss of sample. Specifically, long digestion times can lead to poor cell quality vis-a-vis changes in molecular expression profiles and death. Thus, improving tissue dissociation such that single cells can be liberated in a rapid, gentle, and thorough manner would dramatically advance the clinical potential of single cell diagnostics under modalities such as flow cytometry, mass spectroscopy, and single cell sequencing [33]–[35], [67]. The fields of tissue engineering and regenerative medicine would also directly benefit from improving the procurement of healthy and functional primary, progenitor, and stem cells from various organs and tissues to serve in tissue constructs and cell-based therapies [36], [38]–[40], [42], [68], [69].

To advance tissue dissociation, we developed a novel microfluidic device that gently and efficiently breaks down cellular aggregates into single cells [51]. Key features include an array of branching channels that decrease in size from millimeters to hundreds of microns, as well as repeating expansions and constrictions of the channel width to generate hydrodynamic fluid jets and shear forces. The net effect was that shear stresses of different size scales and magnitudes could be applied to cell aggregates and clusters to mechanically separate cells from each other. Extensive testing with cancer cell aggregates and spheroids demonstrated that our microfluidic device significantly improved cell recovery in terms of single cell numbers and purity. These results were obtained using minimal proteolytic digestion, and in some cases even without enzymes. Moreover, we did not observe changes in cell viability, and total processing time was less than 10 minutes. However, we have not yet tested this device on actual tissue specimens. Furthermore, we fabricated our devices from multiple layers of hard plastic using a commercial laminate process. While this provided a robust device that was amenable to large-scale manufacturing, further device development has been limited by high fabrication cost and the poor resolution of commercial lasers. Thus, a rapid prototyping method is needed to optimize microfluidic channel design and improve dissociation performance.

Rapid prototyping of microfluidic devices has been dominated by photolithography and molding of polydimethylsiloxane (PDMS) because it is fast, cheap, easy to use, and has relatively high resolution. However, device complexity and manufacturing potential are limited by difficulties controlling channel depth and combining multiple layers into a single device. Moreover, the elastic nature of PDMS can be a drawback for applications that require high fluid flows or pressures [70]. Laser micro-machined polymeric films in

conjunction with adhesive transfer tapes for bonding have recently emerged as a robust and cost-effective rapid prototyping method for multilayer microfluidic devices [71]. The versatility and efficacy of such devices has been demonstrated in an array of microfluidic applications, with channel resolutions on the order of 50 μm [72]–[80]. Most importantly, use of laser-etched polymeric films and adhesive transfer tapes will recapitulate the form and function of the commercial laminate systems used for our original microfluidic dissociation device.

In this chapter, we utilize laser etched polyimide films as a rapid prototyping tool to optimize the design of our microfluidic cell aggregate dissociation device. We first demonstrate that a single-layer polyimide film based device can dissociate cancer cell aggregates into single cells, but not as effectively as a multilayer counterpart. However, reducing channel dimensions improves performance such that dissociation efficiency is on par with, and even surpasses, our multilayer device. Next we employ computational fluid dynamics simulations to optimize the design of the channel expansions, resulting in a new geometry that we refer to as a shark fin. While the shark fin design modestly improves cancer cell aggregate dissociation, extending the extent of the shark fin channel expansions yields the best dissociation results that we have seen to date. Finally, we validate performance of our microfluidic dissociation devices using mouse kidney tissue. Following standard tissue mincing and collagenase digestion procedures, we find that microfluidic treatment dramatically increases single cell recovery, lowers the number of aggregates, and maintains cell viability. The best results are obtained using two microfluidic devices in series, with the original multilayer device first reducing large tissue fragments and aggregates into smaller units, followed by a final sample polishing step using the new

optimized single layer shark fin device to produce more single cells. Compared to a standard 1 hour digestion control, dual device treatment produces three-fold more single cells at the same digestion time, and comparable numbers after only a brief 15 min digestion. This work establishes, for the first time, that microfluidic dissociation improves the speed and efficiency of single cell production from digested tissue. Moreover, the combination of different devices and operating principles is needed when working with tissue so as to span a large enough range of channel sizes and shear forces. In future studies, we will continue to explore new dissociation device designs, as well as integration with other microfluidic operations to enable further cell processing and analysis. We will also examine performance using different tissue types including various normal organs and solid tumor specimens.

4.2 Microfluidic Channel Design Optimization to Improve Hydrodynamic Dissociation of Cell Aggregates and Tissue

4.2.1 Device Design

Our original microfluidic dissociation device design consisted of a network of branching channels that progressively decreased in channel width, and channels were arranged across three layers of hard PET plastic that were separated by via layers [51]. The channels also contained repeated expansions and constrictions that generated fluidic jets to supply the shear force needed to separate cells from each other. In this chapter, we employed laser micro-machined polyimide films and lamination as a rapid prototyping method to optimize both channel width and the shape of the channel expansions in an effort to obtain improved single cell recovery. Devices were fabricated using four layers of

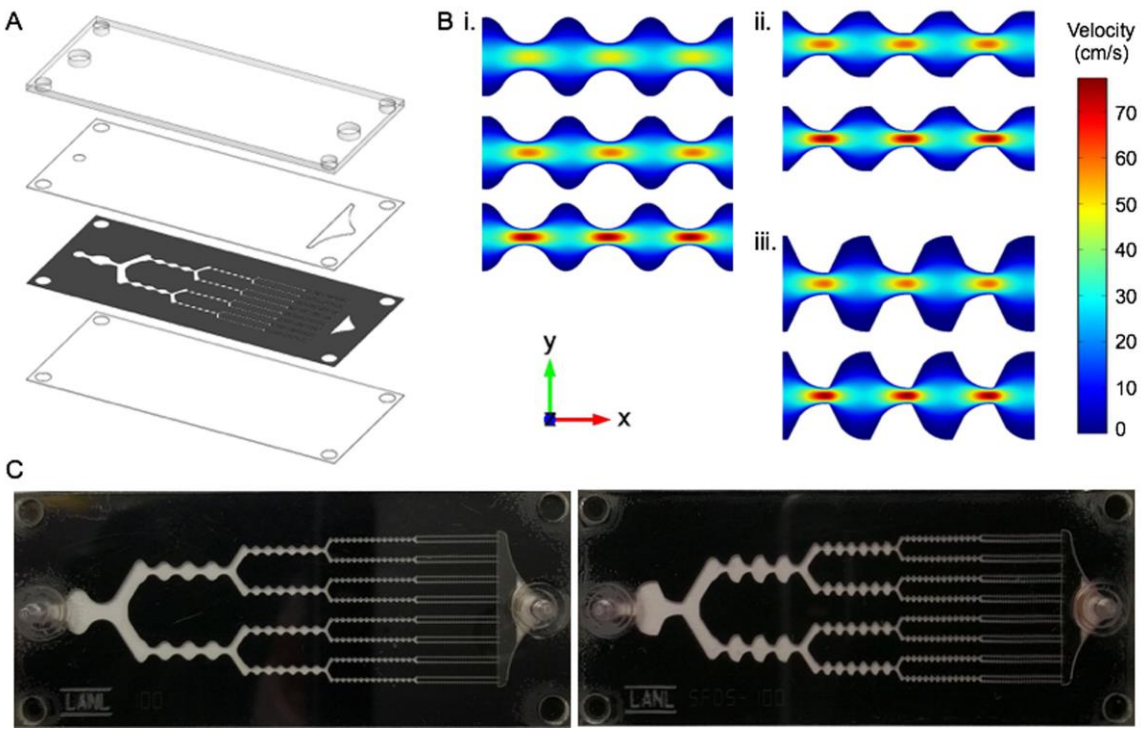

Figure 4.1. Single layer polyimide based microfluidic device and new channel designs. (A) Exploded view showing four device layers including acrylic top layer, PET outlet layer, channel layer produced by laser-etching polyimide film, and PET bottom layer. (B) Finite-element fluid dynamics simulations showing velocity profiles for the (i) original, (ii) shark fin, and (iii) extended shark fin designs at (top to bottom) 125, 100, and 75 μm minimum widths. Simulations were performed at 1 mL/min. Decreasing channel width led to higher maximum flow velocities in the channel constrictions, while the extended shark fin provided greater variation in flow rate between the expansions and constrictions. (C) Pictures of fabricated single layer devices with (left) original and (right) extended shark fin designs. Both devices had a minimum channel width of 100 μm in the fifth stage.

polymeric films bonded by adhesive transfer tape (Fig. 4.1A). The microfluidic channel features were laser-etched into polyimide films, which can allow etching of high resolution features. This simplification to our original design means that samples will not change inertial reference frame nor pass through the two-dimensional via constrictions. We also explored new channel designs, such as reducing the minimum channel width from the original value of 125 μm in the final stage down to 100 and 75 μm. Based on computational fluid dynamics (CFD) simulations, this would increase shear stress within the channel

constrictions by 20 and 50%, respectively (Figure 4.1Bi). Note that the original scaling ratios were retained, including minimum channel width between different branch stages (factor of 2) and the expansion to constriction width within each stage (factor of 3). We further used CFD simulations to explore new channel expansion geometries. These efforts resulted in a non-symmetric design with a more gradual initial expansion and more abrupt transition into the constriction, which we called a shark fin (Figure 4.1Bii). We did not expect the shark fin design to change the maximum flow velocity or shear rate, however, the shark fin produces larger variations in flow velocity experienced between the expansions and constrictions, which we expect will accentuate shear forces on cell aggregates as they move through the channel. Finally, we also created an extended shark fin design by doubling the slope at which the channel constricted, which would further accentuate the variation in flow rate between expansions and constrictions (Figure 4.1Biii). Pictures of the single layer polyimide dissociation devices with the original and extended shark fin channel designs are shown in Figure 4.1C.

4.2.2 Evaluation of Single Channel Layer Devices with Different Channel Widths

We first compared the performance of the original channel design in the new single layer, polyimide film based device to the original multilayer, PET version. We used MCF7 human breast cancer cell line monolayers for these studies, which is a strongly cohesive cell line that produces aggregates under routine cell culture conditions. As in previous work, cell suspensions were introduced into microfluidic devices using a syringe pump at 12.5 mL/min, and were passed through the device either 3 or 10 times. Device effluents were recovered and cell numbers were quantified using a cell counter. For the multilayer

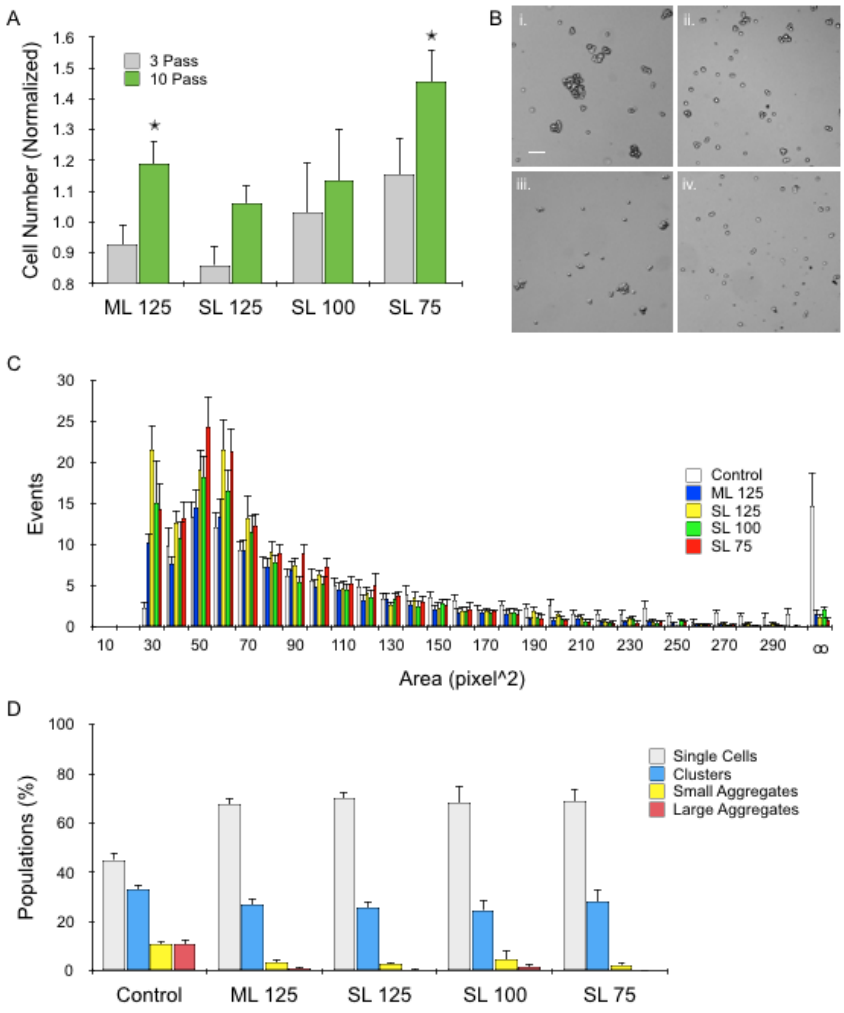

Figure 4.2. Evaluation of single layer polyimide based devices at different channel widths. (A) MCF7 breast cancer cells recovered in device effluents were quantified and normalized by the initial value prior to device processing. The original multilayer (ML) device significantly improved single cell yield after 10 passes, but this was not seen in the single layer transfer tape (SL) device with the same channel dimensions (125 μm). However, decreasing channel width improved performance, with the SL device with 75 μm width exceeding the ML case. (B) Micrographs showing cell suspensions (i) prior to device processing and (ii-iv) after passing 10 times through the (ii) ML, (iii) SL 125, and (iv) SL 75 devices. Scale bar is 100 μm. (C) Cell unit area histogram determined by analyzing micrographs, leading to classification of single cells (<80 pixels^2 and aspect ratio <1.2), clusters (80 to 200 pixels^2 and aspect ratio >1.2; 2-3 cells), small aggregates (200 to 300 pixels^2, 4-10 cells), and large aggregates (>300 pixels^2, >10 cells). Data was combined between 3 and 10 pass conditions. (D) Cell populations above plotted as percent total for the control, ML device, and various SL devices after 10 passes. Device processing eliminated almost all large aggregates and most small aggregates, leading to higher single cell purity. Clusters only decreased slightly. Error bars represent standard errors from at least three independent experiments. * indicates $p<0.05$ relative to non-device processed control (value=1).

device, no change in cell recovery was observed after 3 passes, but 10 passes generated 20% more cells (Figure 4.2A). The single layer device did not show a significant change in cell number for either case. Thus, simplifying the design to a single channel layer substantially diminished dissociation power. This was most likely due the fact that cells no longer changed inertial reference frame, leading to poorer sample mixing, nor passed through via layers that effectively act as two-dimensional constrictions. Next we investigated the effect of reducing channel dimensions throughout the device such that minimum widths in the final stages were 100 and 75 μm minimum width. The 100 μm device results were similar to the original multilayer device after both 3 and 10 passes, but with higher variability. Decreasing channel width further to 75 μm provided the most cells after both 3 and 10 device passes, more than doubling number of new single cells generated in comparison to the original multilayer device.

To obtain information about aggregate populations, cell suspensions were imaged under phase contrast before and after device treatment (Figure 4.2B). Micrographs were then processed to identify contiguous cellular units and determine their area. Results are plotted in Figure 4.2C. The control and device-treated MCF7 populations were similar up to approximately 200 pixels^2, or 750 μm^2, and from this point the control had significantly more events. After extensive cross-referencing, we defined four population categories as follows: single cells, clusters (2 to 3 cells), small aggregates (~4 to 10 cells), and large aggregates (>10 cells). These categories were defined primarily based on area values, however we did observe overlap between the single cell and cluster populations, and thus added aspect ratio as a second metric. The number of events in each category were summed for each treatment condition, and the results are presented for 10 pass device

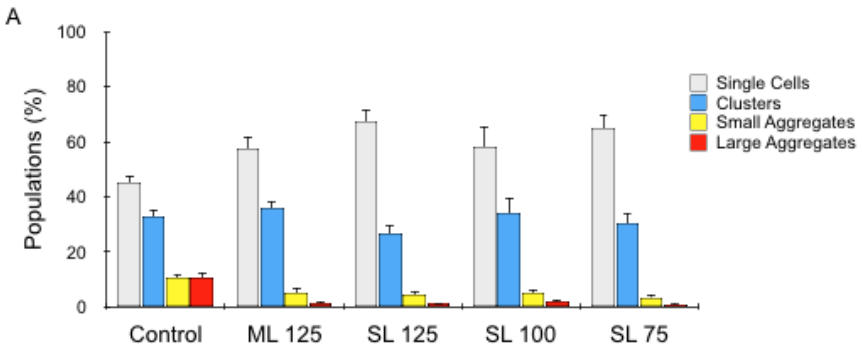

Figure 4.3. Cell populations for multilayer and single layer devices after 3 passes. Cell populations were determined from micrographs and plotted as percent total for the control, ML device, and various SL devices after 3 passes. Results were similar to those after 10 passes presented in Figure 2D, but with slightly larger cluster and aggregate populations. Error bars represent standard errors from at least three independent experiments.

conditions in Figure 4.2D. Single cells constituted less than half of the total events for controls, but increased to as high as approximately 70% with device treatment. Small and large aggregates both represented approximately 10% of the events in controls. Device treatment decreased small aggregates by approximately half and large aggregates to <1% for device cases. Clusters initially represented 35% of controls, and decreased to around 25% for all device cases. Similar results were observed after 3 passes (Figure 4.3), but with slightly higher percentages of clusters and aggregates.

4.2.3 Optimization of Channel Geometry

Next we examined the influence of channel shape, namely the new shark fin and extended shark fin expansion geometries. Experiments were again performed using the MCF7 cancer aggregate model. The original design was again tested to enable direct comparison, and generally yielded similar results for both channel widths (Figure 4.4A). The shark fin design was slightly better than the original at 100 μm minimum width, but there was no difference in performance at 75 μm minimum width. The extended shark fin

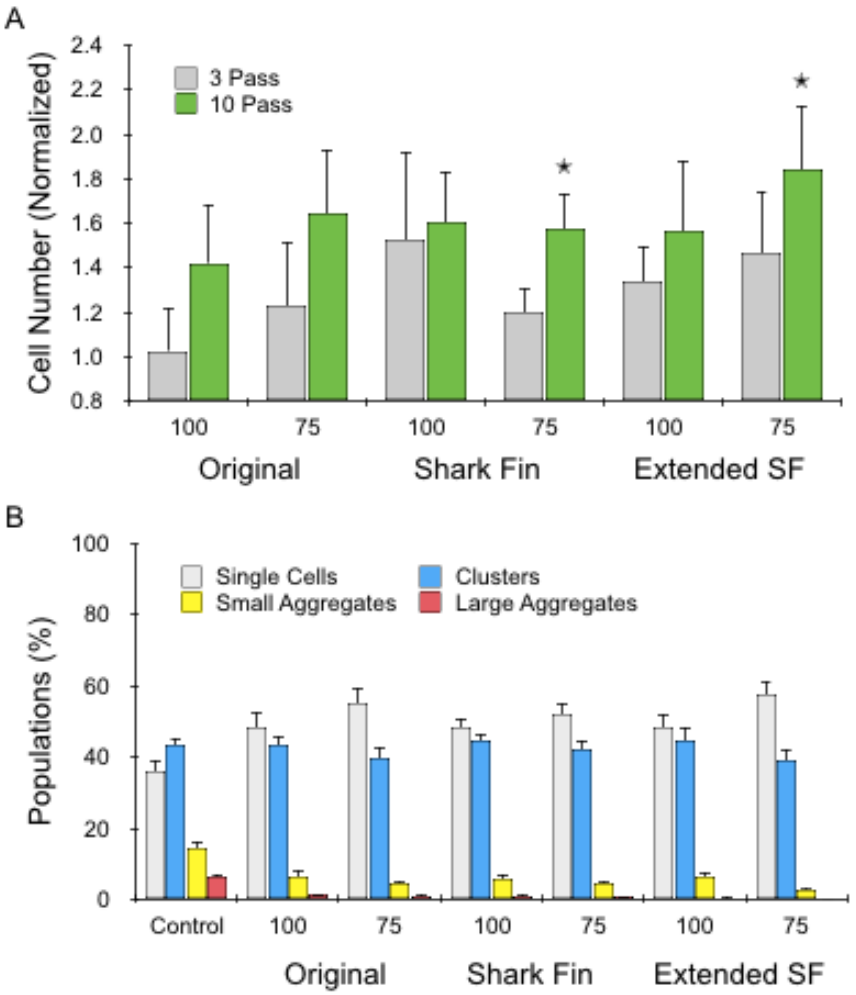

Figure 4.4. Optimization of channel geometry. (A) Normalized MCF7 cell counts obtained for SL transfer tape devices with the original, shark fin, and extended shark fin (extended SF) channel geometries with 100 and 75 μm channel minimum widths. All devices produced more single cells after 10 passes, but only the shark fin and extended SF were significant. (B) Cell populations plotted as percent total for the control and various SL devices after 10 passes. The extended SF design with 75 μm minimum width displayed the highest single cell and lowest cluster/aggregate percentages. Error bars represent standard errors from at least three independent experiments. * indicates $p<0.05$ relative to non-device processed control (value=1).

was most promising, with elevated cell counts relative to the original design across all dimensions and pass numbers, and the highest overall level of single cells produced. While the trends are clear, it should be noted that differences between the device conditions were not statistically significant due to errors. Thus, we quantified cell clusters and aggregates in

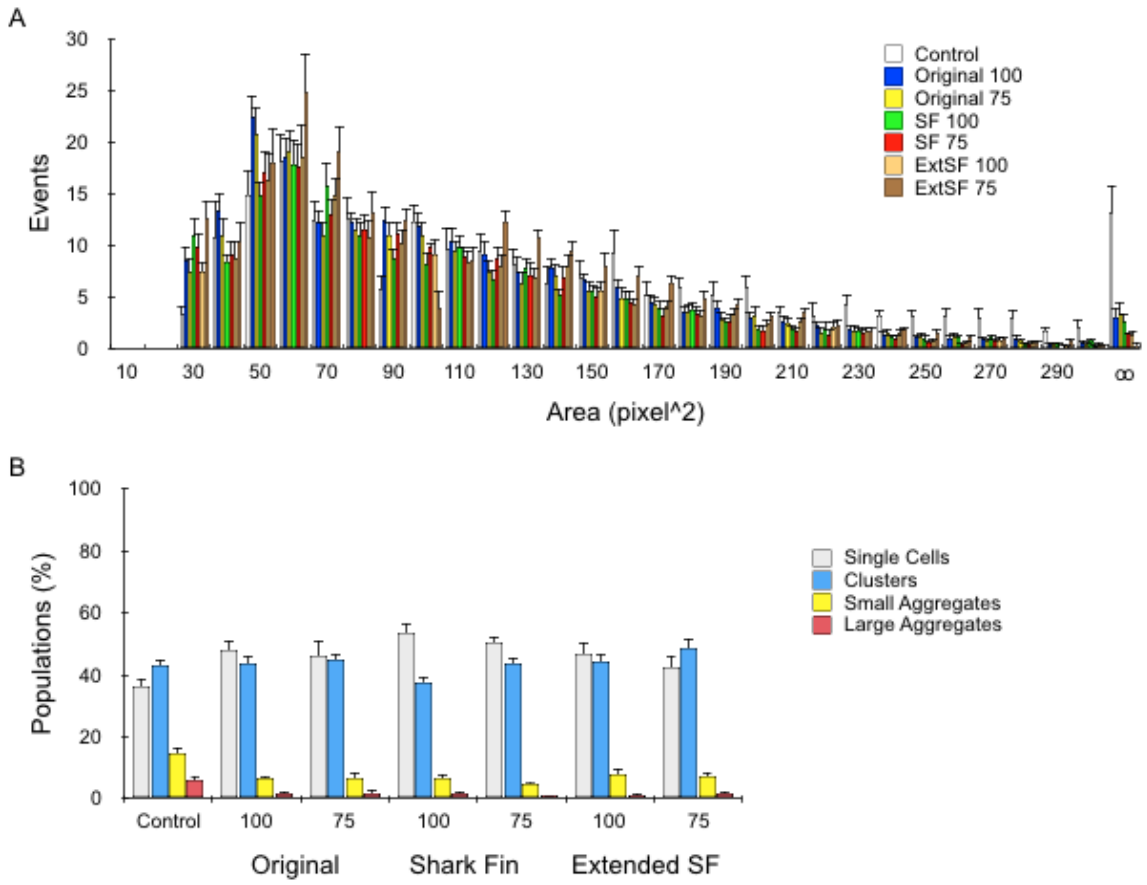

Figure 4.5. Cell populations after 3 passes for different channel geometries. (A) Cell unit area histogram used to determine cell populations in MCF7 suspensions based on image analysis of micrographs. Data was combined between 3 and 10 pass conditions. (B) Cell populations plotted as percent total for the control and various SL devices after 3 passes. Results were similar to those after 10 passes presented in Figure 3B, but with slightly larger cluster and aggregate populations. Error bars represent standard errors from at least three independent experiments.

micrographs as described, and the area histogram is shown in the Supporting Information, Figure 4.5. For all devices, nearly all large aggregates and most small aggregates were dissociated, while small clusters remained in the range of 40-45%. Single cell percentages were elevated from 35 to approximately 50% for most cases. The extended shark fin with 75 μm minimum width provided optimal results, with the highest percentage of single cells at 60% and lowest percentages of all aggregate species.

4.2.4 Validation Performance Using Kidney Tissue

As a final dissociation test, we evaluated performance of the original multilayer and new optimized extended shark fin device using tissue obtained from freshly resected murine kidneys. Kidney is considered to be a difficult tissue to dissociate due to its structure as a dense array of blood vessels and epithelial lined tubules, which function under high physiologic hydrodynamic pressures, have tight intercellular junctions, and have specialized basement membranes [40], [41]. Immediately after harvesting, kidneys were sliced into histologically similar sections with a scalpel, minced into approximately 1 mm^3 pieces, and weighed. Samples were then digested with collagenase for 15, 30, or 60 min in a conical tube under constant agitation, and vortexed every 5 min. Following digestion, samples were passed through the multilayer dissociation device either 3 or 10 times. We chose to employ the single layer, extended shark fin device with 75 μm minimum width only on sample that had already been processed with the multilayer device due to concerns about potential clogging, thus functioning as a final polishing step. To maximize operational efficiency, the two devices were coupled in series, and we only tested 3 passes. Control samples were mechanically treated by vortexing and pipetting, per routine procedure. All digested cellular suspensions were treated with DNase, filtered through a 40 μm cell strainer, and separated into two representative portions. One portion was treated with red blood cell lysis buffer and analyzed using the cell counter while the other was reserved for flow cytometry analysis. For controls, cell recovery increased progressively from approximately 1000 to 2000 cells/mg tissue between 15 and 30 min digestion times, but jumped to approximately 16,000 cells/mg at 60 min (Figure 4.6A). All three device conditions produced dramatically more cells than controls at each digestion time. After 15

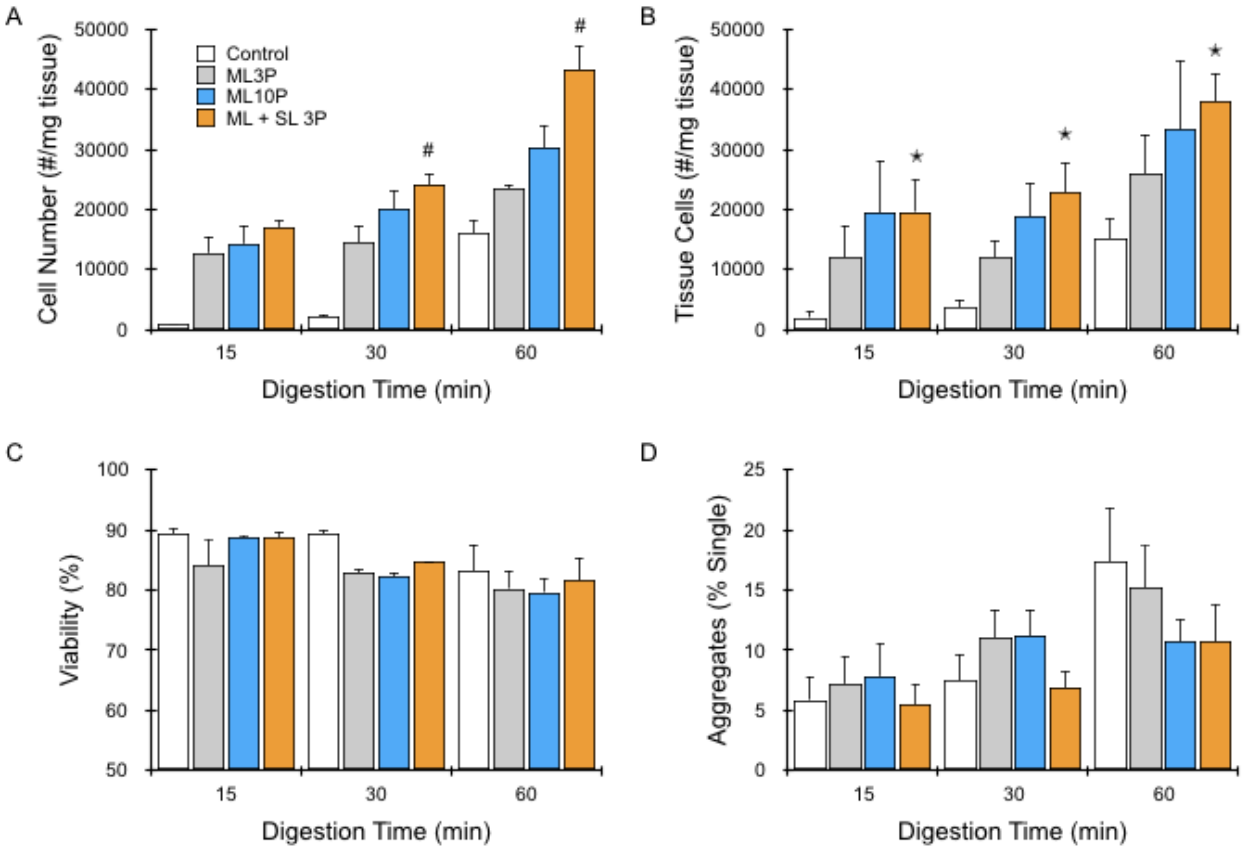

Figure 4.6. Analysis of dissociated mouse kidney cell suspensions. Mouse kidneys were minced, digested with collagenase, and processed under three device conditions: original ML device for 3 and 10 passes and the combination of ML plus SL (extended shark fin, 75 μm) devices for 3 passes. (A) Cell numbers were determined using a cell counter after lysing red blood cells, and showed that all device conditions produced significantly more single cells than digestion alone ($p<0.05$ for all cases). The ML and SL coupled devices provided the highest cell counts at all digestion times. Flow cytometry was also used to directly analyze cell suspensions so as to identify tissue cells and assess viability. (B) The number of single tissue cells recovered matched the cell counter results, but with higher levels of associated error. (C) Tissue cell viability was not affected by device processing at 15 and 60 min, though a small decrease was seen at 30 min. (D) Relative number of tissue aggregates with respect to single tissue cells increased with digestion time, and was lowest for the dual device condition. Error bars represent standard errors from at least three independent experiments. * indicates $p<0.05$ relative to control at the same digestion time. # indicates $p<0.05$ compared to ML 3P condition.

min, three passes through the multilayer device yielded 10-fold more cells than the control. Increasing the number of device passes to 10 had little effect, but co-processing with the single layer device yielded 30% more cells. Findings at the 30 and 60 min digestion times

followed similar trends, but with progressively smaller differences with respect to the controls because cells were better liberated enzymatically. However, there were also progressively larger differences between the device conditions. In terms of maximum cell yield achieved after 60 min digestion, the multilayer 3 pass, multilayer 10 pass, and dual device 3 pass conditions produced 50%, 100%, and 200% more cells than the control, respectively. Notably, the dual device produced more cells after a brief 15 min digestion than the control after 60 min digestion.

The remaining portion of each sample was analyzed using flow cytometry and a panel of four fluorescent probes: CellMask Green to stain phospholipid cell membranes, Draq5 to stain DNA within all cells, 7-AAD to stain DNA only within dead cells with disrupted plasma membrane, and CD45 to stain leukocytes (Table 2.1). This panel enabled distinction of tissue cells from non-cellular debris, anucleate red blood cells, and leukocytes, while simultaneously assessing viability. Stained cell suspensions were analyzed with a BD Accuri Flow Cytometer to obtain the number of each cell type using the gating protocol described in the methods section and shown in chapter 2, Figure 2.3. The number of tissue cells obtained per mg tissue are presented in Figure 4.6B, and generally corroborate cell counter results, but with higher variability. It is unclear whether this variability was due to the greater number of processing steps and time required to label cells with probes, lower reliability of flow cytometry for cell counting, or a change in cell appearance that affected the gating scheme. Tissue cell viability remained similar for all conditions at the 15 and 60 min digestion times, but were slightly lower than control at 30 min (Figure 4.6C). The recovery of red blood cells and leukocytes followed the same trends as tissue cells (Figure 2.3), suggesting that both longer digestion and increased

hydrodynamic dissociation provided greater access to, and likely breakdown of, blood vessels. Interestingly, the relative number of tissue aggregates with respect to single cells increased with digestion time in control cell suspensions (Figure 4.6D). These were likely clusters and small aggregates, as samples had been filtered with the 40 μm strainer. Aggregate percentage was lowest after using the single layer extended shark fin device, as they were converted into more single cells. These results conclusively demonstrate that hydrodynamic treatment using our microfluidic dissociation device concept dramatically increases cell recovery. This was observed at both short and long digestion times, with devices consistently liberating more single cells. Moreover, our new optimized shark fin design can produce more single cells by efficiently breaking down small aggregates and clusters.

4.3 Materials and Methods

4.3.1 Device Fabrication

Dissociation devices were fabricated using laser micro-machined polyimide films following methods similar to previous work described in literature [71]. Briefly, the device was composed of four laser etched layers that were laminated together as follows:

(1) The top layer was fabricated from 1.5 mm acrylic sheets (McMaster Carr, Elmhurst, IL) with through holes to access the microfluidic layers.

(2) The second layer was fabricated from PET films that had silicone based adhesive transfer tape (3M, St. Paul, MN) laminated to both sides. The second layer contained a reservoir for collecting and passing the dissociated samples to the outlet.

(3) The third layer featured the branched microfluidic channel structures, which was fabricated by laser micro-machining polyimide films typically used in the flexible circuit industry.

(4) The bottom layer was fabricated from PET films having silicone based adhesive transfer tape (3M, St. Paul, MN) on the top side. This layer sealed the microfluidic channel layer from the bottom.

Hose barbs were glued into the top layer of the finished device to provide tubing connectors. 2D channel features were designed in AutoCAD.

4.3.2 Fluid Dynamics Simulations

Flow profiles and shear stresses within fluidic channels were simulated using COMSOL Multiphysics software. Finite element fluid dynamics simulations were conducted by coupling the Navier-Stokes equations and continuity equation. Assumptions of laminar flow and the no-slip boundary condition was enforced at the channel walls. Flow rate was 1 mL/min.

4.3.3 Cell Culture and Tissue Models

Human breast cancer cell line MCF7 was obtained from ATCC (Manassas, VA) and cultured in standard tissue culture flasks at 37°C in 5% CO_2 using recommended media: DMEM media containing 10% FBS, 2 mM L-Glutamine, 1 mM sodium pyruvate, 1X non-essential amino acids, 100 U/mL penicillin, 100 μg/mL streptomycin, and 44U/L Novolin R insulin (Thermo Fisher, Waltham, MA). Prior to experiments, confluent MCF7 monolayers were digested with trypsin-EDTA for 5 min, which was sufficient to liberate cells but also

retain a significant number of cellular aggregates. Cell suspensions were washed by centrifugation into PBS containing 1% BSA (PBS+).

Mouse kidney work is detailed in chapter 2, section 2.3.8.

4.3.4 Microfluidic Dissociation

Devices were prepared by affixing 3'' PVC 1/32ID tubing (Nalgene, Rochester, NY) to the hose barbs at the inlet and outlet. A 3-way stopcock was used to connect the device to a syringe containing the cell sample and a buffer reservoir containing 1 PBS+. Immediately prior to experiments, devices were filled with SuperBlock blocking buffer (Thermo Fisher, Waltham, MA), incubated for 15 minutes, and flushed with PBS+. Cell suspensions were then loaded into the sample syringe and administered to the device using a syringe pumps (Harvard Apparatus, Holliston, MA) at a flow rate of 12.5 mL/min. Multiple device passes were achieved by reversing the flow of the syringe pump to replace the sample back into the inlet syringe. This process was repeated for the indicated number of passes. Finally, devices were flushed with 1 mL PBS+ to wash out remaining cells. Cell concentration was measured using a Moxi Z cell counter with type S cassettes (Orflo, Hailey, ID), which utilizes the Coulter principle for cell counting. Cell counts were performed directly on MCF7 suspensions. For kidney samples, one fifth of each suspension was transferred to a new conical tube and incubated with red blood cell lysis buffer containing ammonium chloride, potassium carbonate, and EDTA (BioLegend, San Diego, CA) for 5 min at room temperature prior to obtaining the cell count.

4.3.5 Imaging Cellular Suspensions

MCF7 suspensions were added to a 12-well plate and imaged using a Hoffman phase contrast microscope with a 4x objective. Raw images were converted to binary using

MATLAB, and all distinct cellular units were identified and outlined using ImageJ. Finally, the area of each cellular unit was calculated and classified into the following categories: single cells (20 to 80 pixels^2 or 75 to 300 μm^2), clusters (80 to 200 pixels^2 or 300 to 750 μm^2), small aggregates (200 to 300 pixels^2 or 750 to 1120 μm^2), and large aggregates (>300 pixels^2 or >1120 μm^2). Comparing these categories back to the micrographs, clusters correlated to ~2 to 3 cells, small aggregates contained ~4-10 cells, and large aggregates included >10 cells.

4.3.6 Flow Cytometric Analysis

Mouse kidney work and flow cytometric analysis are detailed in chapter 2, section 2.3.8.

4.3.7 Statistics

Data are represented as the mean ± standard error determined from at least three independent experiments. P-values were calculated based on mean, standard error, and sample population using student t-tests.

4.4 Conclusion

In this chapter, we show that single layer polyimide film can be used to fabricate robust microfluidic devices for dissociating cancer cell aggregates and tissues into single cells. We also used this method as a simple, low-cost, and rapid prototyping method to optimize channel features. While the single layer format is generally less effective than a comparable multilayer design, reducing channel width and changing to the new extended shark fin expansion geometry resulted in the most efficient dissociation and highest single cell recoveries that we have observed to date. We also demonstrated, for the first time,

using mouse kidney tissue that our microfluidic dissociation device concept can produce dramatically more single cells than digestion alone. We also show that using two devices can produce the best results for tissues, as it would otherwise be hard to span a large enough range of channel sizes to effectively break down the largest tissue fragments so that the device doesn't clog, while also being able to convert the smallest cell clusters into single cells. Specifically, the combination of the multilayer device with larger channel dimensions and the optimized single layer device with smaller shark fin channels produced significantly more single cells from kidney tissues. It is unclear how these results will translate to other tissue types, such as softer and more fragile liver tissues or tougher and denser solid tumors. Testing these tissues will be the focus of future work. We will also continue to explore new designs for our dissociation device, as well as combining with microfluidic devices and operations to process and analyze the single cell suspensions.

CHAPTER 5 MICROFLUIDIC TISSUE AND CELL AGGREGATES FILTRATION

5. 1 Introduction

Recent insights into the importance of cellular heterogeneity have combined with advancements in sequencing technologies to help drive interest in the era of single cell analytics [33], [34]. But continued progress towards clinical diagnostics is limited by the fact that most cells within the body reside within tissue masses and organs [34]. For example, the most common and deadly forms of cancer originate from epithelial tissues and subsequently form abnormal tissue masses that are difficult to break down due to high stromal content. Overcoming this obstacle would enable single cell analysis, which has already been used to provide valuable information about tumor progression, metastatic potential, and drug resistance [37], [61], [64]–[66]. Current tissue dissociation procedures include cutting of the tissue into small pieces with a scalpel, lengthy digestion with proteolytic enzymes, mechanical treatment by pipetting and vortexing, and filtering of the remaining tissue aggregates with a cell strainer. This is a laborious, time-consuming, and inefficient process that results in significant loss of sample and potentially poor cell quality vis-a-vis altered molecular expression signatures and death. Thus, improving tissue dissociation such that single cells can be liberated in a rapid, gentle, and thorough manner would dramatically advance the clinical potential of single cell diagnostics such as flow cytometry, mass spectroscopy, and single cell sequencing [33]–[35], [67]. The fields of tissue engineering and regenerative medicine would also be impacted by improving the yield and quality of primary, progenitor, and stem cells needed for tissue constructs and cell-based therapies [38], [40], [42], [68], [69].

In previous chapters, we developed novel microfluidic devices that improved tissue digestion and mechanical dissociation procedures [51]. These devices were composed of hard plastic, and lasers were used to etch channels features that generated hydrodynamic shear forces at precise scales and magnitudes. The digestion device was designed to hold cm-scale tissues in place while fluid containing proteolytic enzymes is used to "hydro-mince" the sample into smaller aggregates. The dissociation device then breaks down aggregates using an array of branching channels that contain alternating constriction and expansion regions. While effective at generating single cells, we have found that significant numbers of small aggregates and clusters still exit from the dissociation device. Since harsher mechanical treatment could damage the single cells that were already liberated, another mechanism is required to remove, or ideally dissociate, these small aggregates and clusters. Cell strainers with pore sizes in the range of 40-80 μm are routinely used to filter large aggregates from dissociated tissue samples. While smaller pore sizes are available, they are typically avoided due to concerns over potential sample loss. Placing the membranes inside of a microfluidic device should alleviate these concerns by minimizing hold-up volume and improving wash efficiency. Alternatives to fluidic channel-based dissociations have also been explored. Track etching, a technology utilizes heavy ion accelerators made etching of precise structures possible on PET and polycarbonate (PC) films possible. Using this technology, size, shape, and density of pores can be etched onto substrates in a controllable manner [81]. Moreover, the use of high flow rates could result in the pores acting as dissociating channels similar to the branching array device, but with smaller dimensions and extremely higher numbers. Overlapping of adjacent pores is commonly observed on track-etched membranes, leading to openings bigger than pore size

intended, thus allowing permeation of small cell clusters. Improvement to current track-etched technique with increased porosity and reduced various in pore sizes have been reported in literature [82]. However, applications adopting such technique haven't been reported. Silicon nanowires have also seen applications in sub-micron virus capturing enabled by microfluidics. Nevertheless, it shares the same drawback as track-etched membranes due to its lack of pore uniformity [83]. Thus, a high-throughput, label-free microfluidic single cell isolation device would be desired.

Vacuum-driven filtration systems containing track-etched membranes and microfluidic devices with integrated microfabricated membranes have been developed and used to isolate circulating tumor cells (CTCs) from blood [84]–[88]. Pore sizes were in the range of 5-10 μm to capture larger epithelial tumor cells from smaller blood cells, and flow rates were typically on the order of mL/h for whole blood and up to 10 mL/min after dilution. Cell deformability was shown to have a strong impact on retention, as cells were able to extrude through much smaller pores depending on their viscosity and the flow rate [84]. A novel microfabricated pillar array called the Cluster-Chip was also developed to capture CTC clusters [85], which have been correlated with high metastatic potential and poor prognosis relative to single cells. The Cluster-Chip successfully trapped >90% of cancer cell clusters at 2.5 mL/h from whole blood, although results were not as strong for triplets and doublets and generally eroded for all cluster sizes as flow rate increased. A track etched membrane with 5 μm pores was also used at similar flow rates, but cluster capture was much lower even though the blood had to be diluted to prevent clogging, presumably because the clusters could squeeze through the pores. For tissue dissociation applications, a filter device would ideally operate at mL/min flow rates to be compatible

with our digestion and dissociation devices. Based on the CTC cluster findings, we would expect poor capture efficiency under these condition for clusters of less than 10 cells, but it is possible that larger-scale aggregates would be retained. However, the fate of clusters that pass through a membrane pore has yet to be investigated. Track etched and microfabricated membranes should both provide the porosity, pore uniformity, and overall strength required for high flow rate applications. While track etched membranes are cheaper and easier to use, the lack of control over pore placement often results in overlapping to produce a larger pore than intended. An alternative that maximizes cost, east of use, and pore uniformity would be nylon membranes similar to those used in cell strainers. These are commercially available as a single layer mesh with pore sizes down to 5 μm. Furthermore, we believe that these nylon mesh membranes have the highest potential to provide a cluster dissociation effect, essentially operating like fluidic channels at the micron scale.

In this chapter we investigate on an alternative to traditional microfluidic dissociation where scale of hydrodynamics is ultimately limited by channel dimensions. We have integrated nylon membrane meshes with well-defined μm-sized pores with laminated acrylic sheets to achieve cluster dissociation at the micron scale that has never been achieved before. With well-defined pore sizes and mesh structures, these pores act like miniaturized microfluidic channels that provide shear at both the right magnitude and dimensions to dissociate clusters remain after tissue digestion and dissociation. In addition to advantages offered by the well-structured mesh membrane, filters with uniform pore sizes can also act as a sieve to separate singles cell from aggregates, thus prevent over-processing of sample. Separation of single cells from its aggregate counterparts can also

effectively avoid channel clogging, which has seen as a major issue in microfluidic-based dissociations [48], [49]. We have validated our filter devices using cancer cell line clusters as well as mouse kidneys. Cell clusters and tissues are introduced to the filter device in either the direct mode, where single cell filtration is achieved directly from pressure-driven flow, or the tangential mode, which allows continues separation of single cells from aggregates while prevent clogging of the filter mesh. In either operating mode, single cell dissociation and enrichment have been demonstrated with significant increase in both single cell yields and population percentage.

5.2 Microfluidic Device for Dual Action of Tissue Dissociation and Filtration

5.2.1 Device Design

Our device was designed to further purify and enrich single cell percentages from upstream tissue digestion and dissociation. Microfluidic single cell enrichment is largely limited by channel dimensions and resolutions. The typical size of a cancer cell aggregate doublet or triplet is approximately 50-100 μm, which is well below the feature resolution that can be etched using a CO_2 laser cutter reliably. As a result, flow-based dissociation would not be able to provide shear in such regime, therefore often fail to break aggregates at this scale further into single cells. To address this issue, we drew our inspiration from well-defined mesh structures found on commercially available nylon filter membranes. These filter membranes possess equally-spaced woven mesh networks, which when oriented in the cross-section of microfluidic channels, can be utilized as fine fluidic channels that are similar in dimensions to that of a single cancer cell. Shear generated from these micron scale “channel network” would produce the same dissociation effects as

millimeter scale channels do on bigger aggregates upstream, effectively breaking them up into smaller units. From a single cell enrichment point of view, these nylon mesh network can also be used as filter membranes. By tuning down flow rates of cells passing through the woven mesh, these micron scale "channel network" would act as filter pores to passively filter out aggregates based on size instead of actively generate shear to achieve the previously described dissociation effect. In this chapter, we have chosen filter membranes having pore sizes of 5, 10, 15, 25, and 50 μm, to demonstrate their dual purpose of single cell dissociation and filtration.

Devices were fabricated in hard acrylic sheets. Fluidic channels and filter membrane housing are laser etched on the channel layers, and are connected by via layers (Figure 5.1). The top and bottom layers are used to seal the device, with hose barbs placed on the top layer to serve as inlet and outlets of the device. All plastic layers were pressure laminated together to form a single unit. Filter membranes were sandwiched in between two acrylic layers, forming two fluidic pathways in the device. Incoming flow from the inlet can either flow through the filter membrane and exit from the single cell outlet, or bypassing the filter membrane and exit from the aggregate outlet (Figure 5.1C). The two outlets are named based on cell composition exiting them, and controlled by setting different flow rates. For example, an 80% aggregate and 20% single cell set up would see a 4x more fluid exiting from the aggregate outlet. The filter device can be operated under two flow conditions based on its design. Under the direct flow mode, the aggregate outlet is closed. Therefore, samples are only allowed to exit from the single cell outlet after coming in contact with the filter membrane. Alternatively, both single cell and aggregate outlets can be kept open during device operation. Under such operation, incoming mixture of

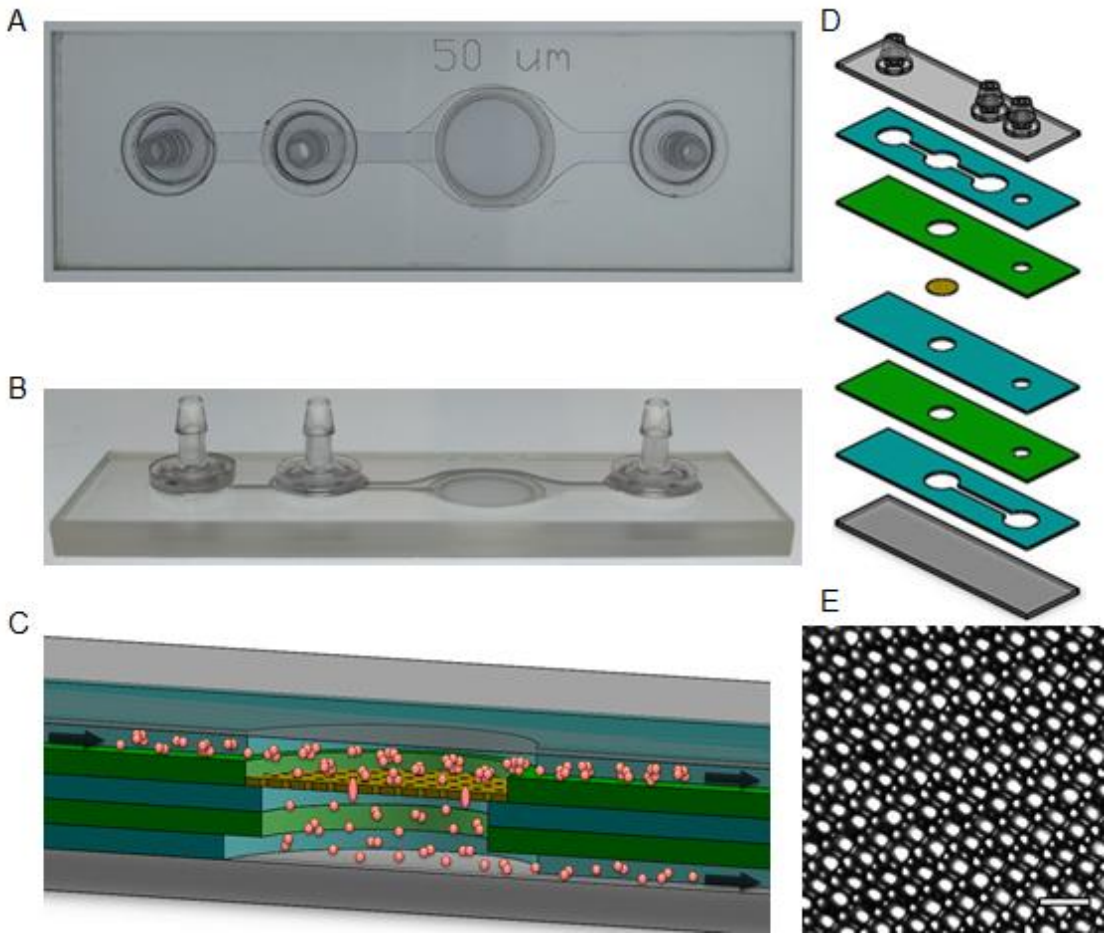

Figure 5.1. Microfluidic filtration device design and operation. Devices were fabricated using hard acrylic sheets. Hose barbs were inserted on the top acrylic layer to facilitate fluid flow. Fluidic channels were devided into 2 flow pathways which are separated by a nylon filter mesh. Top (A) and side (B) views of filter device are demonstrated. (C) Cartoon showing intended flow pathways and interactions between cell aggregates and nylon mesh filter. Clusters are believed to be further broken down into single cells as they travel through the filter mesh. (D) Exploded views showing layer and filter mesh placements. All layers were laminated together to withstand high flow rates. (E) Micrograph showing a 10 μm filter mesh. Scale bar is 100 μm.

single cells and aggregates are diverted upon coming into contact with the filter membrane, which allows only single cells to pass through the mesh network and recycles aggregates back to the inlet for further processing. In this mode, aggregates only come into contact with the filter tangentially, thus are subject to a reduced dissociation effect compared to the direct mode of operation. However, depending on the nature of tissues, operating under

tangential mode could alleviate clogging of tissues being introduced directly onto the filter, while providing a continuous operating format to cycle through tissues that are more challenging to dissociate.

5.2.2 Direct Flow

Performance of the microfluidic device was first evaluated using MCF7 human breast cancer cell line under the direct flow mode. Suspensions of MCF7 single cells and clusters were obtained from routine cell cultures and introduced to the microfluidic device using a syringe pump. Number of events were measured using a Moxi cell counter before and after cells going through the filter membrane. Normalized cell yields are plotted in Figure 5.2A, where a clear trend of increase in single cell yields is established as the filter pore sizes decreases. This result has validated the aforementioned analogy of filter pores acting as micron scale channels in aggregate dissociation. Given the diameter range of a typical single cell, it makes sense to see more single cells liberated from mesh membranes with smaller pores. To access viability of cells liberated from filter dissociation, propidium iodide staining was performed on dissociated cell populations (Figure 5.2B). Logically, cells that had more contact with the filter membrane would suffer from more server mechanical effect, which has clearly been reflected in the plot. It should also be noted that the diameter of a typical MCF7 single cell is approximately 15 to 20 μm. Thus, shape of the cell would change as it is pushed through a pore size much smaller than its diameter to conserve its volume. This has also been reflected by the data as percent live cells passing through pore sizes bigger than 25 μm is roughly comparable to that in the control.

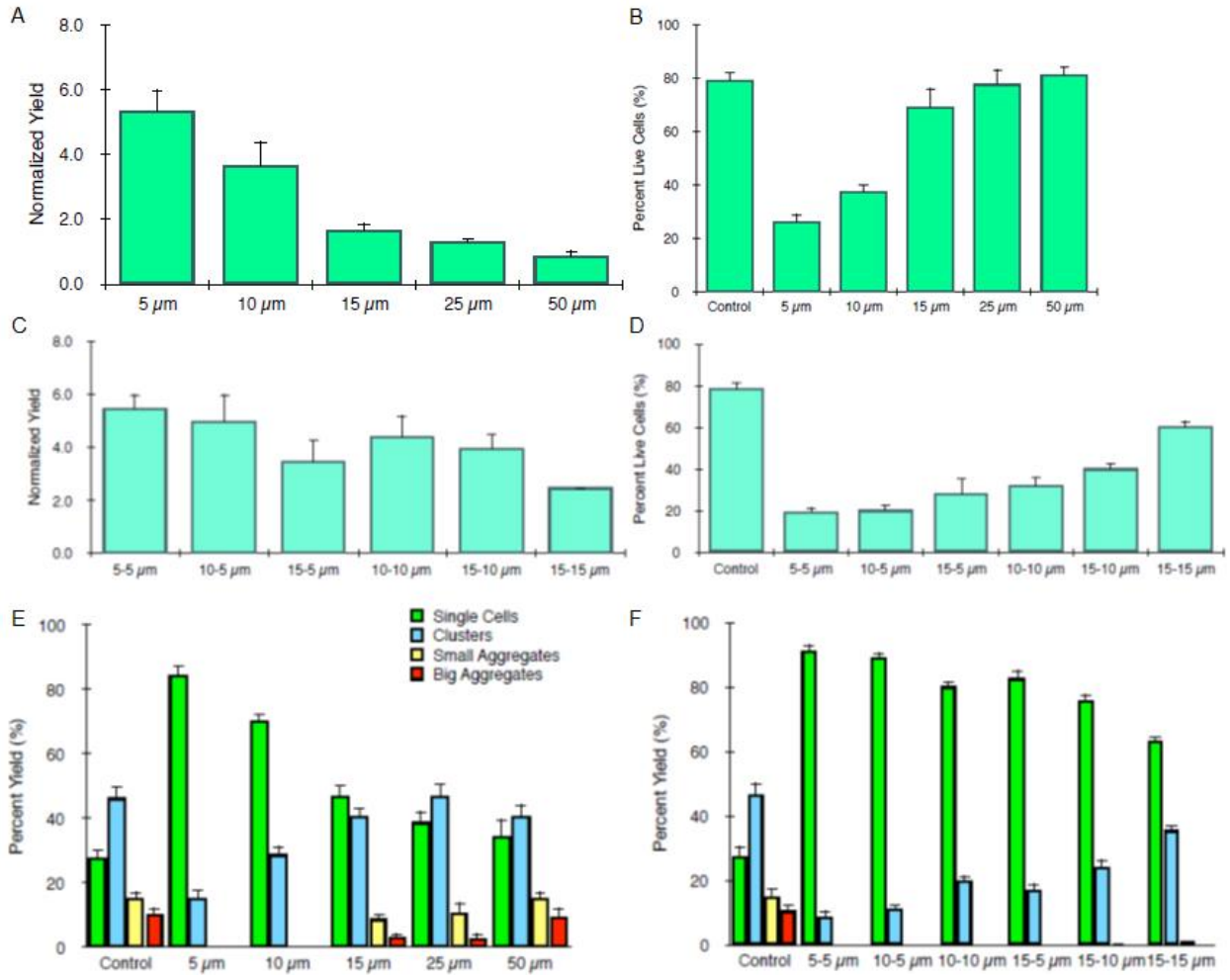

Figure 5.2. Direct flow cell recovery, viability, and population composition. (A) Normalized MCF7 cell counts obtained from sample passing through 5, 10, 15, 25, and 50 μm filter meshes. (B) Sample viability data corresponds to conditions demonstrated in (A). Viability was generally not compromised for cells passing through filter pore size bigger than 25 μm. (C) Filter coupling showed improved viability compared to single filter processing. It was hypothesized that bigger clusters would get broken down into smaller cones before coming into contact with a smaller pore, preventing further damage from colliding with a much smaller pore size filter. (E-F) Effluent population composition of device processed samples. Same imaging procedure was used as that described in chapter 4. Error bars represent standard errors from at least three independent experiments.

Having observed significant increases in single cell yields, the next task would be to reduce compromise in sample viability while maintaining high levels of single cell yield. To help minimize viability, it was hypothesized that if big clusters were broken down into smaller ones before coming into contact with 5 or 10 μm pores, cells would have a better

chance at avoiding colliding with the mesh network at full speed. To test this hypothesis, we coupled a smaller pore size filter with a bigger one upstream to allow aggregates to break up into smaller pieces before entering the downstream device. As demonstrated in Figure 5.2C and D, high single cell yields were maintained while viability was greatly improved by passing sample through a 10 or 15 μm pore size mesh membrane first. Compared to cells passing directly through a single 5 μm filter, sample viability was improved by approximately 10%. To investigate on single cell and aggregate population percentages, cell suspensions were imaged under a phase contrast microscope before and after device treatment following aforementioned imaging procedure in chapter 4. Single cell percentages after device processing have shown as much as 57% increase from the 5 μm filter alone; whereas a double 5 μm filter setup has shown an even greater single cell percentage increase of 63%. It also worth pointing out that the coupled filter setup is quite efficient at eliminating small and big aggregates, as these two sample populations are essentially zero in all coupled filter setups (Figure 5.2 E and F).

Alternatively, viability improvement was also tested by reducing flow rates. MCF7 samples of single cells and aggregates were introduced to 5, 10, and 15 μm filter devices operating under direct flow mode with different flow rates, cell yield and viability were then evaluated (Figure 5.3A and B). Compared to the normal operating flow rate of 12.5 mL/min, sequential reduction of approximately 4 fold to 4, 1, and 0.25 mL/min didn't significantly improve cell viability. Even at the lowest flow rate of 0.25 mL/min, 5 μm device processing viability was only improved by 10% compared to the same operation carried out at 12.5 mL/min. Compromise in cell viability could potentially be contributed more from cell contact with the mesh network, not flow rate. A cell would have to be

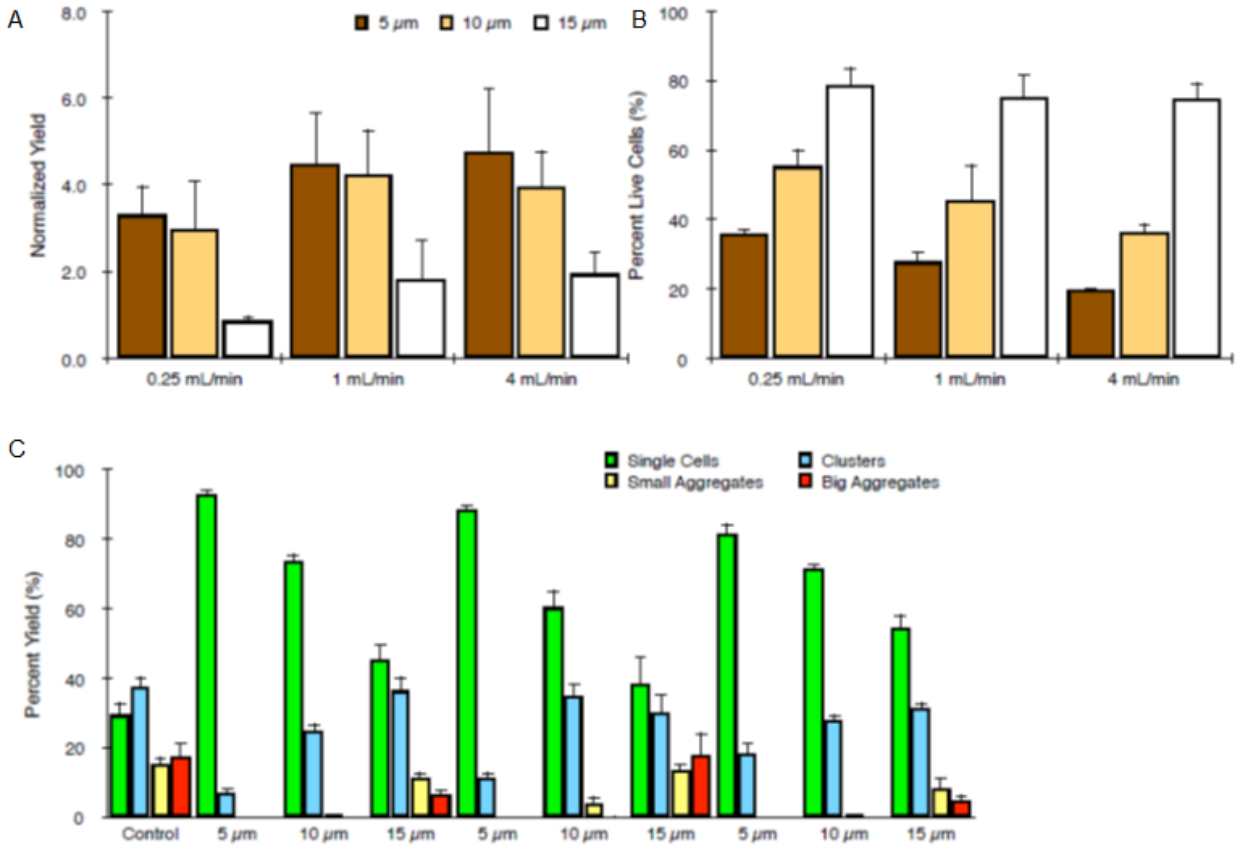

Figure 5.3. Filtration at reduced flow rate. (A) Normalized MCF7 cell counts obtained from sample passing through 5, 10, and 15 μm filter meshes at reduced flow rates. (B) Sample viability data corresponds to conditions demonstrated in (A). Sequential reduction of flow rate decreased cell recovery but essentially had no effect on viability. This leads to the conclusion that compromise in cell viability comes from interactions between cells and filter mesh, not flow rate. (C) Effluent population composition of device processed samples. Same imaging procedure was used as that described in chapter 4. Single cell percentage decreased as flow rate was lowered from 4 to 0.25 mL/min. Error bars represent standard errors from at least three independent experiments.

squeezed through pores smaller than its diameter regardless of the driving force behind it, thus susceptible to roughly the same magnitude of mechanical force during the dissociation process. Furthermore, cell yields produced by decreased flow rates are only slightly lower compared to that from 12.5 mL/min (Figure 5.3A), indicating flow rate is directly correlated to cell yields. Since microfluidic cell dissociation is driven by shear force, which is directly proportional to flow rate, it is expected to have low cell yields from reduced flow

rates. Population composition analysis was evaluated using the same procedure as described above (Figure 5.3C). Single cell percentage decreased as flow rate was lowered from 4 to 0.25 mL/min, reflecting the same trend seen in Figure 5.3A.

5.2.3 Tangential Flow

While device testing under the direct flow mode has provided a good understanding of the microfluidic device, a more advanced operating procedure is to be developed before the full potential of the device can be utilized. As mentioned before, one of the biggest challenges in microfluidic tissue dissociation is device clogging. This issue can be resolved by introducing flows parallel instead of perpendicular to the filter mesh, thus allowing samples to have tangential interactions with the mesh. This tangential interaction would be key in separating single cells from the mixture while sending aggregates back to the inlet for further device dissociation. Another advantage of a tangential flow format would be its capability of introducing continuous flow to the device setup. To test this setup, single cell and aggregate outlets were connected to syringes running under withdraw mode, pulling out cells from each outlet based on flow rates set on the syringe pumps. Three combinations of flow rates were tested under the tangential setup, with tangential (abbreviated T) to direct (abbreviated D) flow rate ratios of 80:20, 60:40, and 40:60. Sum of the two flow rates were kept at 12.5 mL/min. After collecting cells in each respective syringe, cells in the tangential syringe were sent to the direct syringe before samples were finally evaluated as shown in Figure 5.4A. Comparing different filter pore sizes, we see that more single cells were recovered from smaller pore size filters. Different flow rate ratios have not contributed significantly to cell yields or population composition (Figure 5.4B).

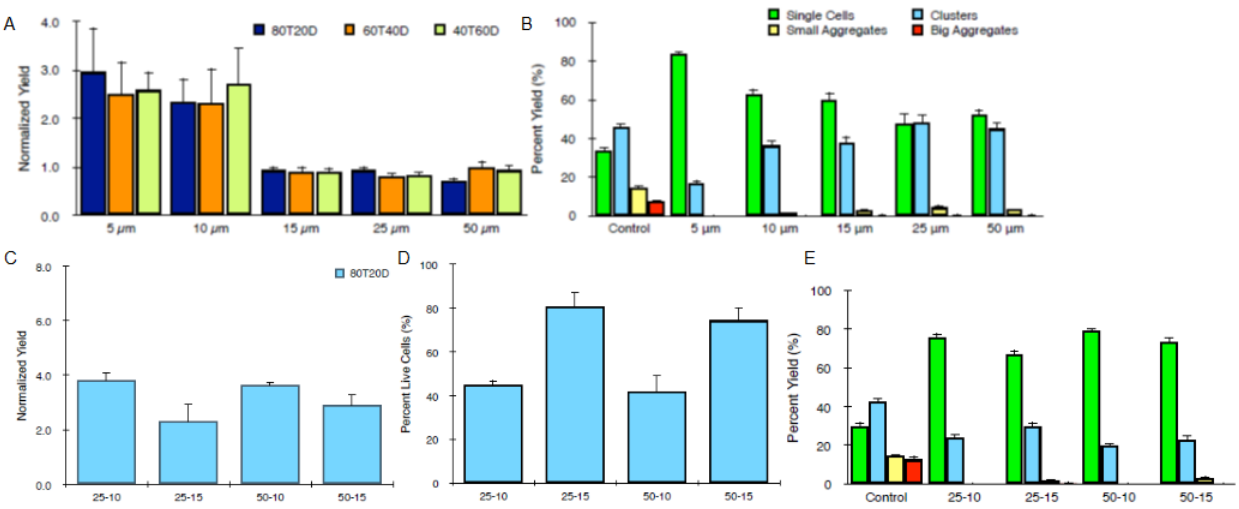

Figure 5.4. Tangential flow cell recovery, viability, and population composition. (A) Normalized MCF7 cell counts obtained from three flow rate ratios of 80:20, 60:40, and 40:60, tested on 5, 10, 15, 25, and 50 μm filter meshes. (B) Effluent population composition of device processed samples. Same imaging procedure was used as that described in chapter 4. Different flow ratios did not contribute significantly to population composition. Data shown were from 80:20. (C-D) Coupled direct and tangential device cell recovery and viability. A smaller tangential pore size of 10 μm produced about 2-fold more cells than their 15 μm counterparts. However a greater recovery was achieved through a compromise in cell viability. (E) Effluent population composition from coupled direct and tangential running at the ratio of 80:20. Population composition followed a similar trend, showing coupled devices under tangential mode were more efficient at eliminating aggregate populations. Error bars represent standard errors from at least three independent experiments.

To further explore possibilities of tangential filtration, we coupled two filter devices in series with a bigger pore size followed by a smaller one. In this setup, aggregate outlet on the upstream filter device was blocked, so that sample would pass through the first filter under direct flow mode before entering the downstream tangential filter. As mentioned before, the purpose of the upstream filter is to break up aggregates into smaller clusters prior to their introduction downstream. A set of 2 filters were selected to serve as the upstream and downstream sizes. Specifically, we have tested 50 and 25 μm filters followed by 10 and 15 μm filters, respectively (Figure 5.4C). Propidium iodide stationing and

imaging analyses were used again to evaluate sample viability and composition (Figure 5.4D). Similar to results seen from direct flow coupled devices, coupled devices under tangential mode are also more efficient at eliminating small and big aggregate populations (Figure 5.4E).

5.2.4 Validation of Mouse Kidney Tissue

Finally, devices were tested using freshly resected murine kidney samples. These tissues would best represent samples that would be used in future device integrations. After kidneys were obtained from mice, kidneys were sliced in half first to ensure histologically similar distribution of samples, then minced into ~1 mm^3 pieces with a scalpel and weighed. Filter device experiments were then conducted as previously described for MCF7 cell line models. Separate 15, 30, and 60 min controls were included in which the tissues were minced using the same procedure. Following device processing, control and experimental samples were vortexing and pipetted, filtered through a 40 μm cell strainer, and treated with DNase to remove extracellular DNA.

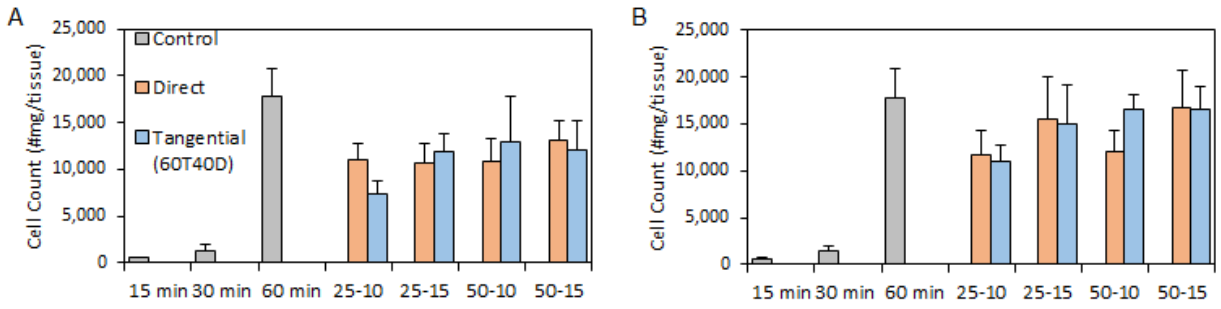

Figure 5.5. Coupled filtration device recovery. Coupled direct and tangential devices were tested with mouse kidney tissues after a 15 (A) and 30 min (B) collagenase digestion. Device processed samples at both digestion points yielded significantly more cells/mg than the collagenase-treated samples. After a 30 min collagenase digestion and device treatment, cell yields were as high as that seen from a 60 min collagenase control. Error bars represent standard errors from at least three independent experiments.

Kidney tissues were processed with coupled microfluidic filter devices under both direct and tangential modes. Under this operating condition, device processing has returned significantly more cells per mg compared to controls only treated with collagenase for the same amount of time (Figure 5.5). In general, samples with 30 min collagenase pre-treatment have shown higher cell yields compared to their 15 min counterparts. Cells liberated from a combination of 30 min collagenase digestion and device processing yielded as much cells as that seen from a 60 min control. It worth mentioning that cell yields from mouse kidney tissues did not follow a similar trend seen from cell line work, where smaller pore size filter mesh produced more cells. This is likely due to the fact that real tissue cells are in general smaller than cells from tissue cultured cell lines. In other words, if cells being filtered are significantly smaller than filter pore size, dissociation effect being subjected to the cell will be reduced by a significant amount.

In an effort to maximize cell yields from mouse kidney tissues, we decided to couple two filter devices running in direct mode. As mentioned earlier, since these tissue cells are significantly smaller than cell line models such as MCF7, shear being subjected on the cells should be greatly reduced. Our final evaluation focused on determining single and aggregate tissue cells, leukocytes, and red blood cells and their viabilities. Fresh mouse kidney were prepared and digested as described in chapter 2. Device-treated cellular suspensions were filtered through a 40 μm cell strainer and labeled with a panel of four fluorescent probes as described in Table 2.1. As mentioned before, this panel enabled distinction of tissue cells from non-cellular debris, anucleated red blood cells, and leukocytes, while simultaneously assessing viability. Stained cell suspensions were analyzed with a BD Accuri Flow Cytometer to obtain the number of each cell type using the

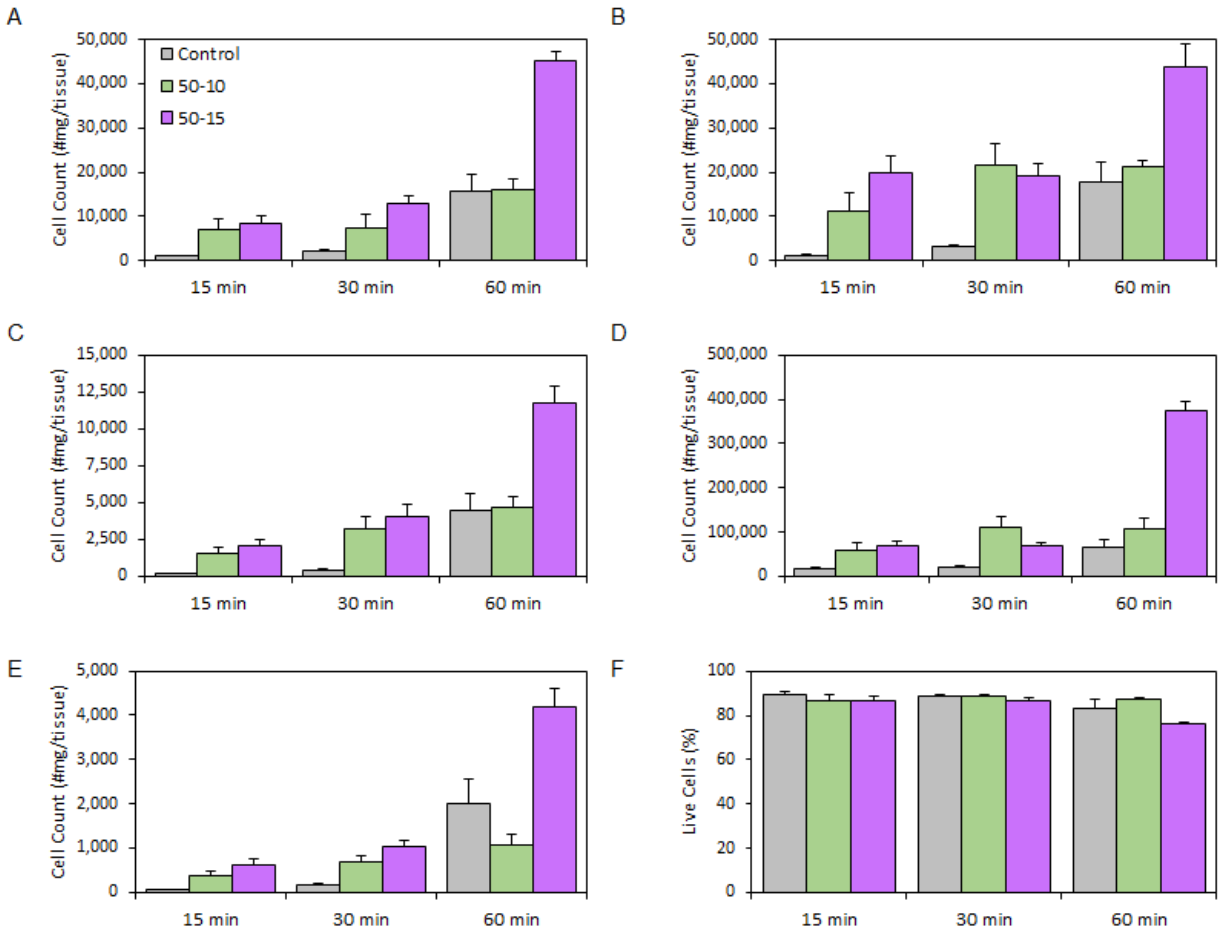

Figure 5.6. Coupled direct filtration device recovery and analysis. Filtration devices running under direct flow mode were coupled and tested with mouse kidney tissues. Samples were divided into three digestion times of 15, 30, and 60 min. Moxi cell counts (A), single tissue cells (B), leukocytes (C), red blood cells (D), aggregate tissue cells (E), and viability (F) were analyzed and plotted. The 50-15 µm double filter combination demonstrated superior dissociation and filtration capability compared to the 50-10 µm combination. It yielded more cells in every single metric tested, with only slightly compromised viability. Error bars represent standard errors from at least three independent experiments.

gating protocol described in the methods section and shown in Figure 5.6. Six metrics were tested, including cell counts from Moxi cell counter, single tissue cell yield, leukocyte, red blood cells, aggregate tissue cell yield, and sample viability. The 50-15 µm double direct filter combination has demonstrated superior results in almost every single metric tested, with only a slightly lowered viability. Single tissue cell yields from cell counter results

matched well with that determined from flow cytometry, suggesting a high reliability in cell yields.

5.3 Materials and Methods

5.3.1 Device Fabrication

Microfluidic devices were fabricated using a commercial microfabrication process offered by ALine, Inc. (Rancho Dominguez, CA). Briefly, fluidic channels and filter and hose barb openings were etched onto 7 acrylic and PET layers using a CO_2 laser. Devices layers as well as nylon mesh membranes were then laminated together to form a single device.

5.3.2 Cell Culture and Tissue Models

Human breast cancer cell line MCF7 work is detailed in chapter 4, section 4.3.3.

Mouse kidney work is detailed in chapter 2, section 2.3.8.

5.3.3 Dissociation and Filtration Studies

Microfluidic filter devices were prepared by affixing 3" PVC 1/32ID tubing (Nalgene, Rochester, NY) to the hose bars at device inlet and outlets. A 3-way stopcock was used to connect a washing buffer reservoir to syringe and device. Prior to experiments, devices were primed with SuperBlock blocking buffer (Thermo Fisher Scientific, Waltham, MA), incubated for 15 min to prevent non-specific binding of cells to channel walls and filter membrane. Devices were primed again with PBS+ (1x PBS with 5% BSA) right before experiment, replacing SuperBlock buffer in device. Depending on sample type, cell line samples were directly loaded into a sample syringe and administered to the device using a syringe pump (Harvard Apparatus, Holliston, MA) whereas mouse kidney samples were

digested using collagenase at indicated time intervals at 37°C. After initial device run, channels were flushed with 1 mL PBS+ to wash out any remaining cells. Cell counts were measured using a Moxi Z cell counter with type S cassettes (Orflo, Hailey, ID), which utilizes the Coulter principle for cell detection and counting.

5.3.4 Imaging Cellular Suspensions

Imaging work is detailed in chapter 4, section 4.3.5.

5.3.5 Flow Cytometric Analysis

Mouse kidney work and flow cytometric analysis are detailed in chapter 2, section 2.3.8.

5.4 Conclusion

In this chapter, we have developed a microfluidic filtration device downstream of the digestion and dissociation devices introduced in earlier chapters. This device is designed to eliminate cellular aggregates using an embedded nylon mesh membrane. In work using *in vitro* cancer cell line aggregates such as MCF7 cells, we have found that mesh membranes with pore sizes smaller than 25 μm filter small and large aggregates effectively. However, we also discovered that the 5, 10, and 15 μm pore sizes could also act to dissociated aggregates and clusters into single cells, thus improving single cell recovery. To better carry out the dual-purpose of this device, we designed and implemented direct and tangential modes. In the direct flow mode, samples are driven through filter membranes to maximize yell yields. Our results have shown while this is a feasible approach, a relatively large penalty of reduced cell viability have to be paid. Tangential mode, on the other hand, maximizes interactions between tissue and cell aggregates to be dissociated and the filter

membrane, thus reducing harsh physical interactions compared to the direct flow mode. Tangential operation not only increased cell viability, it also served as a better platform for continuous device integration. At the conclusion of this work, we are positioned to pursue large basic research and clinical studies analyzing solid tumor specimens from various cancer types using single cell sequencing. Further technology development could also be pursued, such as adding downstream microfluidic operations such as cell sorting or capturing modules for purification purposes. Furthermore, we could integrate microfabricated detection platforms such as micro-NMR or single cell-analysis devices [16], [22] to extend our technology to study other diseases and tissues at the single cell level.

CHAPTER 6 SUMMARY AND FUTHER DIERECTIONS

6.1 Summary

Advances in biomedical engineering technologies, such as microfabricated devices, hold exciting potential for analyzing clinical samples. Taking advantage of microfabrication technologies, miniaturized devices now have the potential to be integrated with biology and medicine to serve in a broader range of applications. In this dissertation, we sought develop a suite of microfluidic devices that are capable of tissue digestion, dissociation, and filtration. These microfluidic devices were designed to generate tailored fluid flow at specific size scales, mechanically disrupt tissue fragments, and achieve single cell level dissociation at the end of the process. These novel devices offered heretofore unprecedented capabilities for processing clinical specimens and paved the way for rapid expansion in the role of cell-based molecular analysis within clinical settings. We have chosen microfluidic technologies for its precise sample manipulation, high throughput, and cost efficiency. A microfluidic platform is also ideal for integration of chambers, valves, and pumps all on a plastic chip.

In chapter 2, we developed a microfluidic digestion device to directly interface tissue biopsies with microfluidic enabled processes. We showed that with a brief device digestion, tissues can be broken down to the size scales that are suitable for downstream dissociation. In chapter 3, we created our microfluidic dissociation device using a commercial laminate microfabrication process offered by ALine, Inc. We believed this fabrication process can handle much larger liquid volumes and higher pumping rates in comparison to standard photolithographic options. This fabrication format ensured that we

can meet the throughput required for processing tumor tissue samples in milliliters of fluid. Based on results from cell line models such as monolayer sheets and tumor spheroids, we showed that our dissociation device is able to generate single cell suspensions without comprising viability even in enzyme-free conditions. This would greatly increase usability of dissociated cells as biomarkers would be preserved for further diagnostics downstream. In chapter 4, channel optimization options were explored by means of dimension and geometry characterizations. Device channel dimensions and geometries were tailored to optimize device performance based on tissue models. In chapter 5, the concept of microfluidic filtration was introduced to further purify single cell populations. Filtration devices integrated with micron scale nylon mesh membranes demonstrate augmented single cell yield following microfluidic digestion and dissociation. To achieve the overall goal of developing a series of microfluidic devices that are capable of tissue dissociation as well as making it a compatible platform for downstream applications, all devices were initially tested with cell line-based models for proof of concepts followed by testing with more advanced tissue models such as mouse organs and human tumor biopsies for real world applications.

6.2 Future Directions

With the core microfluidic tissue processing technologies developed and validated, microfluidic technologies including tissue digestion, dissociation, and filtration are established and ready for implementation as a front end sample processing unit for research and clinical studies using single cell technologies such as flow cytometry and single cell sequencing. Since our devices are cost-effective and simple to fabricate, they

would be easy to commercialize for use in basic science and clinical labs that have a need for single cell work. It is also worth mentioning that our dissociation and filtration devices are already fabricated using a commercial process. Having said that, we envision all three of our devices introduced in this dissertation would be integrated into one platform to enable lab-on-a-chip tumor dissociation applications.

Aside from microfluidic mechanical aspect, we have always been interested in applying our microfluidic devices to translational work. After validating our devices using a small panel of tumor biopsies from patients, we envision participating in full scale clinical studies focused on tumor metastasis, progression, prognosis, and novel therapy development. In addition to diagnosing physical property changes in patient's tumor cells, we are also keenly interested in better understanding the mechanisms that give rise to these phenotypes. In other words, what specific changes are occurring within cells that lead to changes in mechano-behavior. Defining these connections is critical for understanding how cell survival may be enhanced to confer treatment resistance. A successful tumor treatment relies upon induction of apoptosis to induce cell death. Therefore, we are actively seeking connections between the cellular changes that bring about altered physical properties and factors that can sway the balance between anti and pro-apoptotic signals.

We also plan to combine the physical assays proposed with previous work sensing molecular biomarkers using nanoparticles. This would entail adding new components to the device that will make it possible to label the cells with nanoparticle sensors, perform purifications, and detect the signals. Detection could involve the magnetic nanoparticle or

micro-NMR format that we have used previously for profiling clinical samples. Alternatively, we could use fluorescent nanoparticles such as quantum dots and optical detection, which would be more amenable to a flow through microfluidic format and could be performed on single cells to maintain information about subpopulations and tumor heterogeneity. Adding molecular biomarker information would be extremely valuable for improving diagnostic, prognostic, or therapeutic capabilities. In addition, it could provide insight into the underlying molecular mechanisms behind biophysical property changes, such as signal transduction pathway activity or protein expression level, or help confirm the identity of important subpopulations.

References

[1] D. Hanahan and R. A. Weinberg, "Hallmarks of cancer: The next generation," *Cell*, vol. 144, no. 5, pp. 646–674, 2011.

[2] R. A. Burrell, *et al*., "The causes and consequences of genetic heterogeneity in cancer evolution," *Nature*, vol. 501, no. 7467, pp. 338–345, 2013.

[3] C. E. Meacham and S. J. Morrison, "Tumour heterogeneity and cancer cell plasticity," *Nature*, vol. 501, no. 7467, pp. 328–337, 2013.

[4] M. R. Junttila and F. J. de Sauvage, "Influence of tumour micro-environment heterogeneity on therapeutic response," *Nature*, vol. 501, no. 7467, pp. 346–354, 2013.

[5] P. L. Bedard, *et al*., "Tumour heterogeneity in the clinic," *Nature*, vol. 501, no. 7467, pp. 355–364, 2013.

[6] D. J. Slamon, *et al*., "Use of chemotherapy plus a monoclonal antibody against HER2 for metastatic breast cancer that overexpresses HER2," *N. Eng J. Med*, vol. 344, no. 11, pp. 783–792, 2001.

[7] T. S. Mok *et al.*, "Gefitinib or carboplatin-paclitaxel in pulmonary adenocarcinoma," *N. Eng J. Med*, vol. 361, no. 10, pp. 947–957, 2009.

[8] C. S. Karapetis *et al.*, "K-ras mutations and benefit from cetuximab in advanced colorectal cancer," *N. Eng J. Med*, vol. 359, no. 17, pp. 1757–1765, 2008.

[9] P. B. Chapman *et al.*, "Improved survival with vemurafenib in melanoma with BRAF

V600E mutation," *N. Engl J. Med*, vol. 364, no. 26, pp. 2507–2516, 2011.

[10] E. Paldino, *et al*., "Tumor initiating cells and chemoresistance: which is the best strategy to target colon cancer stem cells?," *Biomed Res Int*, vol. 2014, pp. 1-7, 2014.

[11] W. Liao *et al*., "Metastatic cancer stem cells: from the concept to therapeutics," *Am J. Stem Cells*, vol. 3, no. 2, pp. 46–62, 2014.

[12] D. Ponti, *et al*., "Breast cancer stem cells: An overview," *Eur J. Cancer*, vol. 42, no. 9, pp. 1219–1224, 2006.

[13] R. K. Jain, "Normalization of tumor vasculature: an emerging concept in antiangiogenic therapy," *Science*, vol. 307, no. 5706, pp. 58–62, 2005.

[14] M. Hristov and C. Weber, "Endothelial progenitor cells: characterization, pathophysiology, and possible clinical relevance," *J. Cell Mol Med*, vol. 8, no. 4, pp. 498–508, 2004.

[15] S. C. Bendall *et al.*, "Single-cell mass cytometry of differential," *Science*, vol. 332, no. 6030, pp. 687-696, 2011.

[16] J. B. Haun *et al.*, "Micro-NMR for rapid molecular analysis of human tumor samples," *Sci Transl Med*, vol. 3, no. 71, pp. 71ra16-71ra16, 2011.

[17] D. Issadore *et al.*, "Ultrasensitive clinical enumeration of rare cells ex vivo using a micro-hall detector," *Sci Transl Med*, vol. 4, no. 141, pp. 141ra92-141ra92, 2012.

[18] D. A. Ateya, *et al*., "The good, the bad, and the tiny: A review of microflow cytometry," *Anal Bioanal Chem*, vol. 391, no. 5, pp. 1485–1498, 2008.

[19] J. Sun *et al.*, "A microfluidic platform for systems pathology: Multiparameter single-cell signaling measurements of clinical brain tumor specimens," *Cancer Res*, vol. 70, no. 15, pp. 6128–6138, 2010.

[20] A. K. White *et al.*, "High-throughput microfluidic single-cell RT-qPCR," *Proc Natl Acad Sci U. S. A.*, vol. 108, no. 34, pp. 13999–14004, 2011.

[21] W. H. Grover, *et al.*, "Measuring single-cell density," *Proc Natl Acad Sci U. S. A.*, vol. 108, no. 27, pp. 10992–10996, 2011.

[22] D. R. Gossett *et al.*, "Hydrodynamic stretching of single cells for large population mechanical phenotyping," *Proc Natl Acad Sci*, vol. 109, no. 20, pp. 7630–7635, 2012.

[23] A. D. Boiko *et al.*, "Human melanoma-initiating cells express neural crest nerve growth factor receptor CD271," *Nature*, vol. 466, no. 7302, pp. 133–137, 2010.

[24] P. Dalerba *et al.*, "Phenotypic characterization of human colorectal cancer stem cells," *Proc Natl Acad Sci U. S. A.*, vol. 104, no. 24, pp. 10158–10163, 2007.

[25] K. S. Chan *et al.*, "Identification, molecular characterization, clinical prognosis, and therapeutic targeting of human bladder tumor-initiating cells," *Proc Natl Acad Sci U. S. A.*, vol. 106, no. 33, pp. 14016–14021, 2009.

[26] M. E. Prince *et al.*, "Identification of a subpopulation of cells with cancer stem cell properties in head and neck squamous cell carcinoma," *Proc Natl Acad Sci U. S. A.*, vol. 104, no. 3, pp. 973–978, 2007.

[27] R. Strauss *et al.*, "Analysis of epithelial and mesenchymal markers in ovarian cancer reveals phenotypic heterogeneity and plasticity," *PLoS One*, vol. 6, no. 1, pp. 1–20,

2011.

[28] J. Voldman *et al*., "Microfabrication in biology and medicine," *Annu Rev Biomed Eng*, vol. 1, no. 3, pp. 401–425, 1999.

[29] D. J. Beebe, *et al*., "Physics and applications of microfluidics in biology," *Annu Rev Biomed Eng*, vol. 4, no. 1, pp. 261–286, 2002.

[30] T. M. Squires and S. R. Quake, "Microfluidics: fluid physics at the nanoliter scale," *Rev Mod Phys*, vol. 77, no. 3, pp. 977–1026, 2005.

[31] N. Lion, *et al*., "Why the move to microfluidics for protein analysis?," *Curr Opin Biotechnol*, vol. 15, no. 1, pp. 31–37, 2004.

[32] S. C. Jacobson, *et al*., "Microchip structures for submillisecond electrophoresis," *Anal Chem*, vol. 70, no. 16, pp. 3476–3480, 1998.

[33] S. C. Bendall and G. P. Nolan, "From single cells to deep phenotypes in cancer," *Nat Biotechnol*, vol. 30, no. 7, pp. 639–647, 2012.

[34] C. Gawad, *et al*., "Single-cell genome sequencing: current state of the science," *Nat Rev Genet*, vol. 17, no. 3, pp. 175–188, 2016.

[35] J. M. Irish *et al*., "Mapping normal and cancer cell signalling networks: towards single-cell proteomics," *Nat Rev Cancer*, vol. 6, no. 2, pp. 146–155, 2006.

[36] S. R. Singh, "Somatic stem cells," *Methods Mol Biol* vol. 879, 2012.

[37] D. A. Lawson *et al.*, "Single-cell analysis reveals a stem-cell program in human metastatic breast concer cells," *Nature*, vol. 526, no. 7571, pp. 131–135, 2015.

[38] A. A. Palakkan *et al*., “Liver tissue engineering and cell sources: issues and challenges,” *Liver Int*, vol. 33, no. 5, pp. 666–676, 2013.

[39] M. Ramirez-Dominguez, "Pancreatic islet isolation: from the mouse to the clinic," *Adv Exp Med Biol*, vol. 938. 2016.

[40] S. C. Presnell *et al.*, “Isolation, characterization, and expansion methods for defined primary renal cell populations from rodent, canine, and human normal and diseased kidneys,” *Tissue Eng Part C Methods*, vol. 17, no. 3, pp. 261–273, 2011.

[41] C. Van der Hauwaert *et al.*, “Isolation and characterization of a primary proximal tubular epithelial cell model from human kidney by CD10/CD13 double labeling,” *PLoS One*, vol. 8, no. 6, pp. 2–11, 2013.

[42] R. S. Mahla, “Stem cells applications in regenerative medicine and disease therapeutics,” *Int. J. Cell Biol*, vol. 2016, pp 1-24, 2016.

[43] L. J. Hickson *et al*., “Challenges and opportunities for stem cell therapy in patients with chronic kidney disease,” *Kidney Int*, vol. 89, no. 4, pp. 767–778, 2016.

[44] J. El-Ali, *et al*., “Cells on chips,” *Nature*, vol. 442, no. 7101, pp. 403–411, 2006.

[45] L. Y. Yeo, *et al*., “Microfluidic devices for bioapplications,” *Small*, vol. 7, no. 1, pp. 12–48, 2011.

[46] A. Lenshof and T. Laurell, “Continuous separation of cells and particles in microfluidic systems,” *Chem Soc Rev*, vol. 39, no. 3, p. 1203-1217, 2010.

[47] D. R. Gossett *et al.*, “Label-free cell separation and sorting in microfluidic systems,”

Anal Bioanal Chem, vol. 397, no. 8, pp. 3249–3267, 2010.

[48] C. H. Lin, *et al*., "Single-cell enzyme-free dissociation of neurospheres using a microfluidic chip," *Anal Chem*, vol. 85, no. 24, pp. 11920–11928, 2013.

[49] L. Wallman *et al.*, "Biogrid—a microfluidic device for large-scale enzyme-free dissociation of stem cell aggregates," *Lab Chip*, vol. 11, no. 19, pp. 3241-3248, 2011.

[50] S. M. Hattersley, *et al*., "Development of a microfluidic device for the maintenance and interrogation of viable tissue biopsies," *Lab Chip*, vol. 8, no. 11, pp. 1842-1846, 2008.

[51] X. Qiu, *et al*., "Microfluidic device for mechanical dissociation of cancer cell aggregates into single cells," *Lab Chip*, vol. 15, no. 1, pp. 339–350, 2015.

[52] A. Biddle *et al.*, "CD44 staining of cancer stem-like cells is influenced by down-regulation of CD44 variant isoforms and up-regulation of the standard CD44 isoform in the population of cells that have undergone epithelial-to-mesenchymal transition," *PLoS one*, vol. 8, no. 2, pp. e57314-e57314, 2013.

[53] A. C. Hatch *et al.*, "1-million droplet array with wide-field fluorescence imaging for digital PCR," *Lab Chip*, vol. 11 no. 22, pp. 3838–3845, 2011.

[54] A. J. Mach *et al.*, "Automated cellular sample preparation using a centrifuge-on-a-chip," *Lab Chip*, vol. 11, no. 17, pp. 2827-2834, 2011.

[55] J. M. Kelm *et al.*, "Multicellular tumor spheroids applicable to a wide variety of cell types," *Biotechnol Bioeng*, vol. 83, no. 2, pp. 173-180, 2003.

[56] S. Krishnamurthy, "Applications of molecular techniques to fine-needle aspiration

biopsy," *Cancer*, vol. 111, no. 2, pp. 106–122, 2007.

[57] D. P. Clark, "Seize the opportunity: underutilization of fine-needle aspiration biopsy to inform targeted cancer therapy decisions," *Cancer*, vol. 117, no. 5, pp. 289–297, 2009.

[58] T. Crnogorac-jurcevic *et al.*, "Gene expression profiles of pancreatic cancer and stromal desmoplasia," *Oncogene*, vol. 20, no. 50, pp. 7437-7436, 2001.

[59] W. F. Symmans *et al.*, "Total RNA yield and microarray gene expression profiles from fine-needle aspiration biopsy and core-needle biopsy samples of breast carcinoma," *Cancer*, vol. 97, no. 12, pp. 2960-2971, 2003.

[60] B. A. Centeno *et al.*, "Classification of human tumors ssing gene expression profiles obtained after microarray analysis of fine-needle aspiration biopsy samples," *Cancer*, vol. 105, no. 2, pp. 101-109, 2005.

[61] I. Tirosh *et al.*, "Dissecting the multicellular ecosystem of metastatic melanoma by single-cell RNA-seq," *Science*, vol. 352, no. 6282, pp. 189–196, 2016.

[62] E. Z. Macosko *et al.*, "Highly parallel genome-wide expression profiling of individual cells using nanoliter droplets," *Cell*, vol. 161, no. 5, pp. 1202–1214, 2016.

[63] R. Satija *et al.*, "Spatial reconstruction of single-cell gene expression," *Nat Biotechnol*, vol. 33, no. 5, pp. 495–502, 2015.

[64] A. P. Patel *et al.*, "Single-cell RNA-seq highlights intratumoral heterogeneity in primary glioblastoma," *Science*, vol. 344, no. 6190, pp. 1396–1401, 2014.

[65] H. Li *et al.*, "Reference component analysis of single-cell transcriptomes elucidates cellular heterogeneity in human colorectal tumors," *Nat Genet*, vol. 49, no. 5, pp. 708–718, 2017.

[66] A. S. Venteicher *et al.*, "Decoupling genetics, lineages, and microenvironment in IDH-mutant gliomas by single-cell RNA-seq," *Science*, vol. 355, no. 6332, pp. 1-11, 2017.

[67] N. E. Navin, "The first five years of single-cell cancer genomics and beyond," *Genome Res*, vol. 25, no. 10pp. 1499–1507, 2015.

[68] S. V Murphy and A. Atala, "3D bioprinting of tissues and organs," *Nat Biotechnol*, vol. 32, no. 8, pp. 773–785, 2014.

[69] A. Keating, "Mesenchymal stromal cells : new directions," *Cell Stem Cell*, vol. 10, no. 6, pp. 709–716, 2012.

[70] B. S. Hardy *et al.*, "The deformation of flexible PDMS microchannels under a pressure driven flow," *Lab Chip*, vol. 9, no. 7, pp. 935–938, 2009.

[71] P. Nath *et al.*, "Rapid prototyping of robust and versatile microfluidic components using adhesive transfer tapes," *Lab Chip*, vol. 10, no. 7 pp. 2286–2291, 2010.

[72] N. Crews *et al.*, "Continuous-flow thermal gradient PCR Thermal Gradient PCR in a Continuous-Flow Microchip," *Biomed Microdevices*, vol. 10, no. 2, pp. 187-195, 2008.

[73] J. Kim and B. K. Gale, "Rapid prototyping of microfluidic systems using a PDMS/polymer tape composite," *Lab Chip*, vol. 9, no. 9, pp. 1290–1293, 2009.

[74] H. J. Sant and B. K. Gale, "Flexible fabrication , packaging , and detection approach for

microscale chromatography systems," *Sensors Actuators B. Chem*, vol. 141, no. 1, pp. 316–321, 2009.

[75] P. K. Yuen and V. N. Goral, "Low-cost rapid prototyping of flexible microfluidic devices using a desktop digital craft cutter," *Lab Chip*, vol. 10, no. 3, pp. 384–387, 2010.

[76] J. Greer *et al.*, "Comparison of glass etching to xurography prototyping of microfluidic channels for DNA melting analysis," *Micromech Microeng*, vol. 17, no. 12, pp. 2407-2413.

[77] X. Yuan *et al.*, "Electrokinetic biomolecule preconcentration using xurography-based micro-nano-micro fluidic devices," *Anal Chem*, vol. 87, no. 17, pp. 8695-701, 2015.

[78] P. Nath *et al.*, "Polymerase chain reaction compatibility of adhesive transfer tape based microfluidic platforms," *Microsys Technol*, vol. 20, no. 6, pp. 1187-1193, 2013.

[79] D. Patko *et al.*, "Microfluidic channels laser-cut in thin double-sided tapes: cost-effective biocompatible fluidics in minutes from design to final integration with optical biochips," *Sensors Actuators B. Chem*, vol. 196, pp. 352–356, 2014.

[80] K. Shen *et al.*, "A microchip-based PCR device using flexible printed circuit technology," *Sensors Actuators B. Chem*, vol. 105, no. 2, pp. 251–258, 2005.

[81] P. Apel, "Track etching technique in membrane technology," *Radiat Meas*, vol. 34, no. 1-6, pp. 559–566, 2001.

[82] M. Y. Kim, *et al.*, "Microfabrication of high-resolution porous membranes for cell culture," *J. Memb Sci*, vol. 452, pp. 460–469, 2015.

[83] Y. Xia *et al.*, "Label-free virus capture and release by a microfluidic device integrated with porous silicon nanowire forest," *Small*, vol. 13, no. 6, pp. 1–11, 2017.

[84] F. A. W. Coumans, *et al.*, "Filtration parameters influencing circulating tumor cell enrichment from whole blood," *PLoS One*, vol. 8, no. 4, pp. e61774-e61774, 2013.

[85] A. F. Sarioglu *et al.*, "A microfluidic device for label-free, physical capture of circulating tumor cell clusters," *Nat Method*s, vol. 12, no. 7, pp 685-691, 2015.

[86] M. G. Krebs *et al.*, "Analysis of circulating tumor cells in patients with non-small lung cancer using epithelial marker-dependent and –independent approaches," *J. Thorac Oncol*, vol. 7, no. 2, pp. 306 - 315, 2012.

[87] Y. Tang *et al.*, "Microfluidic device with integrated microfilter of conical-shaped holes for high efficiency and high purity capture of circulating tumor cells," *Sci Rep*, vol. 4, no. 6052, pp. 1–7, 2014.

[88] G. Vona *et al*., "Isolation by size of epithelial tumor cells: a new method for the immunomorphological and molecular characterization of circulating tumor cells," *Am J. Pathol*, vol. 156, no. 1, pp. 57–63, 2000.